Master thesis and internship[BR]- Master's Thesis : Comet Interceptor: Optimisation of Quasi-Ballistic Departure Opportunities by Means of a Lunar Swing-by[BR]- Internship (linked to master's thesis)

Auteur : Ranuschio, Daniel
Promoteur(s) : Kerschen, Gaetan
Faculté : Faculté des Sciences appliquées
Diplôme : Master en ingénieur civil en aérospatiale, à finalité spécialisée en "aerospace engineering"
Année académique : 2019-2020
URI/URL : http://hdl.handle.net/2268.2/10151

UNIVERSITY OF LIÉGE

Faculty of Applied Sciences

Graduation Studies conducted for obtaining the
Master's degree in Aerospace Engineering

Comet Interceptor: Optimisation of Quasi-Ballistic Departure Opportunities by Means of a Lunar Swing-by

Supervisor at University of Liège:
GAËTAN KERSCHEN

Supervisor at Politecnico di Milano:
CAMILLA COLOMBO

Supervisor at University of Cranfield:
JOAN PAU SÁNCHEZ
CUARTIELLES

Master thesis of:
DANIEL RANUSCHIO
Student Id n. s181154

Academic Year 2019-2020

ACKNOWLEDGEMENTS

ABSTRACT

As part of the Cosmic Vision Programme, the *Comet Interceptor* mission was selected in 2019 as a Fast-track mission programmed to be launched in 2028 together with the ARIEL M4 mission. The objective of the mission is the interception of a pristine comet on its way through the solar system. To accomplish this task the spacecraft will be placed in a quasi-Halo orbit around the L_2 Lagrangian Point where it will stay until a suitable target is identified. At this point the spacecraft begins its journey to the comet by departing from the parking orbit and escaping the Earth's gravitational field.

The aim of this thesis is the analysis of the first section of this journey, i. e., from the detection of the comet to the moment of escape. The analysis is performed assuming the validity of the Planar Circular Restricted Three-Body Problem (PCR3BP) and focuses on the evaluation of the expected value of the escape velocity with respect to the Earth. Initially the trajectory is computed by simply propagating a set of initial conditions, however, in order to optimise the escape conditions, a lunar flyby is introduced to alter the trajectory achieving higher v_∞.

Via a Monte Carlo Simulation it is demonstrated that optimal flybys can be systematically targeted and exploited under different initial conditions, leading generally to a substantial increase in escape velocity potentially reducing the Δv budget that needs to be provided by the spacecraft. Furthermore, it was proven that for some of the transfers also a reduction of the time of flight can be achieved reducing the required notice time, and thus increasing the success rate of the mission.

The obtained analysis serves as a starting point for the analysis of the interplanetary leg of Comet Interceptor. Moreover, the developed methodology can be used for the analysis of trajectories involving multiple lunar flybys.

Keywords: Comet Interceptor; Moon flyby trajectory; Earth escape trajectory; L_2 departure

CONTENTS

LIST OF FIGURES

ACRONYMS

Symbol	Description
2BP	Two-Body Problem
3BP	Three-Body Problem
CCW	Counter-Clockwise
CI	Comet Interceptor
CR3BP	Circular Restricted Three-Body Problem
CReMA	Consolidated Report on Mission Analysis
CW	Clockwise
DNC	Dinamically New Comet
DSM	Deep Space Manoeuvre
EMB	Earth-Moon Barycentre
ESA	European Space Agency
GEO	Geostationary Orbit
GNC	Guidance, Navigation and Control
HPC	High Performance Computer
IC	Inbound Crossing
LPO	Lyapunov Planar Orbit
MAG	Mission Analysis Guidelines
MCS	Monte Carlo Simulation
OC	Outbound Crossing
R3BP	Restricted Three-Body Problem
PBCM	Planar Bi-Circular Model
PCR3BP	Planar Circular Restricted Three-Body Problem

PDF	Probability Density Function
PO	Parking/Periodic Orbit
SOI	Sphere of Influence
SOI_{EM}	Sphere of Influence of the Earth-Moon system
SOI_{SE}	Sphere of Influence of the Sun-EMB system
UML	Unified Modeling Language

LIST OF SYMBOLS

Symbol	Description
C	Jacobi Constant/Integral
C_3	Characteristic Energy
δ	Bending Angle
Δv	Propulsive cost or budget in terms of velocity change
$\mathbf{R}$	Rotation Matrix
$\mathbf{\Phi}$	State Transition Matrix
θ_M	Phase angle of the Moon with respect to the Sun-Earth direction
t_{coast}	Coasting time between $t_{po,0}$ and t_{dep}
t_{dep}	Departure location on the periodic orbit defined from $\mathbf{x}_{po,0}$
$t_{po,0}$	Location at t_0 on the periodic orbit defined from $\mathbf{x}_{po,0}$
tof	Time Of Flight of a specific trajectory
$\mathbf{v}_\infty$	Escape velocity vector
$\oplus$	Symbol for Earth parameters
$\leftmoon$	Symbol for Moon parameters
$\odot$	Symbol for Sun parameters

CONSTANTS

Symbol	Description	Value	Unit
$\widetilde{a}_M$	Mean radius of the lunar Orbit	$384\,401$	km
$m_{\oplus}$	Mass of the Earth	$5.9736990613 \times 10^{24}$	kg
$m_{\mathbb{C}}$	Mass of the Moon	$7.3476418263 \times 10^{22}$	kg
$m_{\odot}$	Mass of the Sun	$1.9889194453 \times 10^{30}$	kg
$R_{\mathbb{C}}$	Radius of the Moon	1738	km
$\mu_{\mathbb{C}}$	Moon gravitational parameter	$4.9027801374 \times 10^{3}$	$\mathrm{km}^3/\mathrm{s}^2$
$\mu_{\odot}$	Sun gravitational parameter	$1.3272448769 \times 10^{11}$	$\mathrm{km}^3/\mathrm{s}^2$
μ_{EM}	Earth-Moon mass parameter	$1.2150535157 \times 10^{-2}$	[-]
μ_{SE}	Sun-Earth mass parameter	$3.0401473507 \times 10^{-6}$	[-]
$T_{\mathbb{C}}$	Moon orbital period	0.4704021	[-]

1

INTRODUCTION

COMET Interceptor (CI) is a Fast-track mission selected in June 2019 as part of ESA's Cosmic Vision Programme. As it is a "fast" mission, it is expected to be launched together with the ARIEL M4 mission in 2028. The objective of the mission is to target and intercept a comet that is visiting the inner Solar System for the first time, and therefore, its composition has not yet been influenced by the heating/cooling of previous visits of the inner system or by the Solar wind. Possible examples are comets coming from the *Oort cloud* [1], a spherical region that is theorised to be located between Pluto's orbit at 6×10^9 km from the Sun and the limit of the Sun's gravitational field at $\sim 2 \times 10^{13}$ km, and to be the source of long-period comets such as *ISON* and *Siding Spring* [2, 3]. Other potential flyby targets are Dinamically New Comet (DNC) or interstellar bodies such as *Oumamuamua* [4]. These bodies are thought to come from outside the solar system, and thus to have formed and evolved in other star systems [5].

In the past, comets were already object of interest for missions like Giotto and the more recent Rosetta [6, 7]. For these missions it was 'only' possible to intercept short-period comets, as a long notice period was necessary in order to design, build and launch the spacecraft for its mission. Therefore, the traditional mission procedure (target selection – spacecraft design and assembly – launch) is unsuitable for targeting new comets which are observed for the first time only a few months or years before perihelion. In order to avoid this problem, CI will be designed, built and launched before even discovering the target. In fact, after launch, the spacecraft,

which comprises three separated modules, will be parked in a Halo orbit around the Sun-Earth L_2 Lagrange point located at 1.5 million kilometres 'behind' the Earth with respect to the Sun. Here it will wait for the discovery of a suitable target which is then intercepted. As the spacecraft is already in space, ready to be sent to the interception point, the entire time between discovery and perihelion can be exploited to select the cheapest trajectory possible.

Prior to the arrival, the different modules will separate in order to make complementary observations of the comet from different points of view. In particular, there will be a main module which will stay at a safe distance from the comet nucleus in order to avoid the dust environment, this module will also serve as the communication hub between the other two modules and the ground segment. The other two modules will dive closer to the nucleus in order to maximise the scientific outcome of the mission. The so obtained multipoint measurements will give an unprecedented 3D description of the target and its coma [8].

1.1 COMET INTERCEPTOR TRAJECTORY REQUIREMENTS

Comet Interceptor, as previously mentioned, is a F-class mission, and as such, it will be launched as a co-passenger together with ARIEL M4. This implies that it will be a spacecraft of modest size, maximum weight of 1000 kg, which limits the amount of propellant on-board and, as a consequence, also the available Δv.

It is clear that the restricted Δv budget has a direct influence on the trajectory design, and in particular, on the reachable region in the ecliptic plane. As discussed by Sánchez Pérez, Bucci, and Skuppin [8] and Sánchez [9], for increasing propulsive budget the accessible heliocentric distance regions increase. For example, with a budget of 1 km/s the reachable range would be $[0.88 - 1.15]$ AU, while for 2 km/s it would increase to $[0.78 - 1.32]$ AU. Given the nature of the mission, targeting

of a yet unobserved comet, increasing the regions which can be 'explored' increases the possibility of detecting a suitable object. In fact, it is observed that, looking both at historical data, see Figure 1.1, and at numerical simulations [10], a greater heliocentric distance range would lead to a larger population of theoretically possible targets.
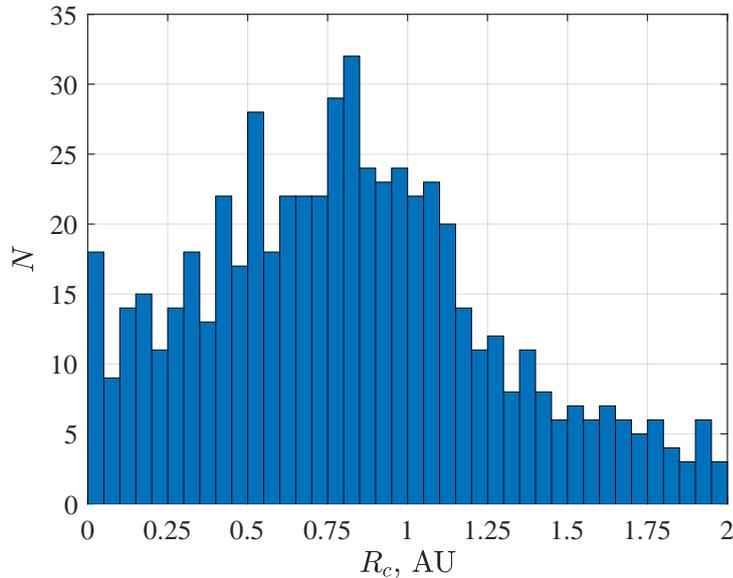
Figure 1.1: Perihelion of long-period comet population observed between 145 BC and 1995 AD [11].

After the detection of a possible target, it is necessary to design the transfer trajectory to understand if the available Δv budget is sufficient for the planned target. To do so a patched conic approach is used dividing the trajectory into three sections:

1. Departure from the periodic orbit around L_2, analysed in this thesis;

2. Interplanetary trajectory between the Sphere of Influence of the Earth-Moon system (SOI_{EM}) and the interception point, preliminary analysis by Sánchez [9];

3. Close approach and comet flyby, referring to the final phase of the transfer and the flyby of the comet.

The optimisation of the interplanetary trajectory is performed by considering two Lambert Arcs divided by a Deep Space Manoeuvre (DSM), it follows that the mission budget can be written as the sum of the departure and the DSM costs, respectively Δv_{dep} and Δv_{DSM}. The second term is mainly influenced by variables such as: t_{dep} (the departure time), t_{DSM} (time between departure and the DSM and the overall transfer strategy, which are impossible to evaluate without knowing the target. On the other hand, Δv_{dep} is the cost required to escape the Earth's gravitational attraction setting the spacecraft on the correct interplanetary trajectory. Its value is thus mainly driven by magnitude of the desired escape velocity, v_{∞},. While under normal circumstances Δv_{dep} is directly provided by the launcher during launch or shortly after, here the fact that CI is placed around L_2 plays in favour of the reduction of the departure manoeuvre as the natural dynamics of the system facilitate the departure trajectory.

Furthermore, by exploiting correctly the Earth's and Moon's gravitational fields, it is possible to further increase the achievable 'free' escape velocity greatly reducing the amount of propellant required for the departure. It follows that, maintaining fixed the total propulsive budget, this would lead to multiple benefits for the overall trajectory design, for example:

- perform a larger DSM, potentially increasing the reachable region for the spacecraft or reducing the total Time Of Flight of a specific trajectory (tof) giving the possibility to intercept comets with shorter notice time;

- after the completion of the primary mission, the mission could be extended by targeting other objects consuming the propellant saved during the departure phase.

This concept will be further discussed in Chapter 3 and Chapter 4.

1.2   HISTORICAL BACKGROUND

Since the dawn of space missions, the main objective for scientists and engineers is to collect as much information as possible from each specific mission. To do so, it is fundamental to reach the highest mass fraction possible for the launched payload. This cannot be obtained easily, in fact, as the missions are becoming more demanding both for the payload size and for the trajectory design, also the amount of required propellant increases.

In order to reach the set objectives, since 1972, gravity assists have been used to perform 'free' manoeuvres in space, reducing the amount of propellant, i. e., Δv, required for the mission. The first example is Pioneer 10 [12], an American space probe targeted at Jupiter, where it performed a gravity assist to become the first spacecraft to achieve escape velocity to leave the Solar System. After Luna 3, many other missions, in particular interplanetary ones, have exploited the capabilities of gravity assists. Some notable examples are Mariner 10 [13], which was the first probe to reach another planet through a gravity assist at Venus, Voyager 1 [14], first mission to cross the heliopause and enter the interstellar medium after flybys of the Jupiter and Saturn systems, and more recent examples like Rosetta and the Parker Solar Probe [7, 15], which performed gravity manoeuvres to match the speed of 67P/Churyumov–Gerasimenko and to decrease its heliocentric velocity respectively.

Gravity assists consist in the exploitation of the relative motion and the gravity field of another body, planet or moon, in order to alter the trajectory and speed of the spacecraft around the main body (e. g., Sun or principle planet). This variation can be desirable for different reasons, in fact, it is possible to increase/decrease the spacecraft as well as rotate the velocity vector outside the initial plane of motion (in general the ecliptic plane). The possibility to design the trajectory including various

gravity assists has allowed the development of mission which with existing propulsion systems would have been impossible.
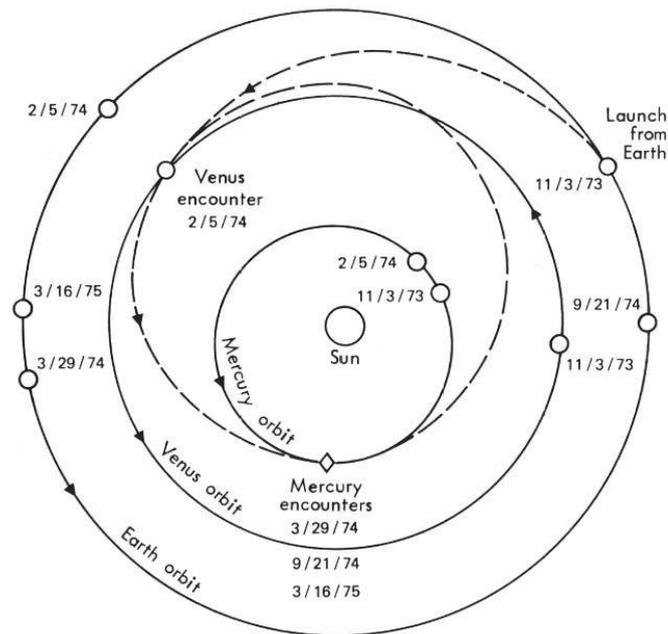
Figure 1.2: Mariner 10's heliocentric trajectory through the inner solar system [13].

For all the above mentioned missions, it was possible to describe the trajectory, at least for the preliminary design, following the a patched conic approach. This approach gave accurate results as the trajectory can be divided into a series of segments. Each segment follows the dynamics of the Two-Body Problem (2BP) (i. e., conic sections) around the instantaneous principal body. The main advantage of this approach is the description of the gravity assists, as they are described as hyperbolic segments inside the sphere of influence of the exploited body. Looking at Figure 1.2, it is possible to observe that the spacecraft follows elliptical arcs between each 'planetary segment', in fact, for the patched conic approach, the sphere of influence of the different planets are considered of infinitesimal radius with respect to the heliocentric distances. As a result of this approximation, the gravity assists are considered as pure rotations of the velocity vector relative to the planet used for the gravity assist. Note

that the magnitude and the direction of the rotation depend on the characteristics of the hyperbolic arc inside the sphere of influence [16].

The problem at hand is fundamentally different, the first peculiarity is that the spacecraft departs from a periodic orbit located around L_2. These orbits are not possible in a 2BP analysis of the trajectory, in fact, they 'appear' only as solutions of the Restricted Three-Body Problem (R3BP). This implies that the first part of the trajectory, i. e., the trajectory inside the SOI_{EM}, cannot be studied as a 2BP around the Earth.

The second particularity of this problem is that the lunar gravity assists do not occur between one interplanetary leg and another, as in the cases above, but are supposed to be exploited before departing for the interplanetary leg. This means that the spacecraft is expected to spend a considerable amount of time in the vicinity of the Earth-Moon system. Using the patched conics approach, in this case, does not give accurate results as the Sun's influence on the trajectory is neglected, while the spacecraft is inside the SOI_{EM}, over a long period of time. This leads to increased errors, negligible in the before mentioned cases, as they are integrated over time. This is particularly true when the trajectory reaches high perigees, as here the Sun's gravity has a much larger influence on the trajectory and can even be exploited during the design as described by Yagasaki [17] and Kawaguchi et al. [18].

1.3 THESIS AIM

The main objective of this thesis is the analysis of the first section of trajectory, leading the spacecraft from the orbit around L_2 to the interplanetary space. As discussed in Section 1.1, the understanding of the departure conditions is fundamental to define the reachable regions for the spacecraft. In fact, this directly translates in a theoretical success probability of the mission as increasing the reachable region

would increase the probability of intercepting a desired target in the available duration of the mission. To finally asses a range of achievable v_∞ the departure is analysed in different steps with increasing complexity until finally the an expected value is obtained.

Initially, in order to set a reference, the departure following directly the unstable manifolds associated with the Planar Lyapunov orbit, i. e., *direct escape/strategy*, will be studied. This result will be used to quantify the advantages of more complex strategies, such as, *single flyby trajectories*. After the reference is set, different methods to study lunar flybys are studied and implemented in order to get a better understanding of the problem at hand and to obtain a framework for the analysis of not only single flybys, but eventually also multiple flybys, which are not the scope of this thesis. As described in Chapter 3, lunar flybys can be efficiently used to increase the hyperbolic escape velocity with respect to the Earth and to slightly change the direction of $\boldsymbol{v}_\infty$. Given the limited amount of Δv, even a slight increase of 'free' escape velocity is desirable. Finally, as the initial and final conditions are not known a priory, a statistical analysis will be performed in order to identify the expected values for $\boldsymbol{v}_\infty$.

This work will cast some light on the real range of initial conditions that can be expected, laying the foundations for a more detailed analysis of the interplanetary trajectory, since its preliminary design has been performed by assuming that escape velocities under 800 m/s are available for any direction, which is not necessarily true [9].

<div style="text-align: right">*2*</div>

MODELS

I N this chapter the different dynamical models are introduced in order to give the reader sufficient insight in the hypotheses and approximations that are considered during the development of the thesis. In addition, the needed reference systems are defined in order to have a clear view of the variables that are introduced later on during the analysis of the methodology and of the obtained results.

Given the particular nature of the problem (i. e., waiting phase around L_2, navigation in the vicinity of the Earth-Moon system and escape towards the interplanetary space) it is necessary to consider the gravitational influence of three massive bodies. As described by Koon et al. [19] the Sun-Earth-Moon system can be described as a Planar Bi-Circular Model (PBCM). As such, the Earth and the Moon are considered to revolve around their center of mass (EMB) and together they rotate with the Sun around the Sun-(Earth-Moon) barycentre. This description arises from a simplification of the more general restricted four-body problem and it is possible given the low eccentricity values of the lunar orbit around the Earth ($e_\mathbb{C} = 0.0549$) and of the Earth's orbit around the Sun ($e_\oplus = 0.0167$). Furthermore, the motion is assumed to happen entirely inside the ecliptic plane, this description is again only possible given the peculiar characteristics of the system.

While the PBCM description gives the more accurate results, between the considered models, it is not suited for an initial analysis; thus, further simplifications are considered to facilitate the study of the problem. In particular, as suggested by various authors (see [20, 21]) the four body problem can be simplified by approximating

it as two PCR3BP problems patched together. This concept is further explained in Section 2.2.

2.1 PLANAR CIRCULAR RESTRICTED 3-BODY PROBLEM

The main model adopted in this thesis is the PCR3BP, which is a simplified version of the General Three-Body Problem. While the more general problem describes the motion of three bodies with comparable mass subjected to their respective gravitational forces, the restricted problem relies on three main assumptions:

- the mass of the third body is negligible with respect of the one of the two main bodies, which subsequently are called primaries (i. e., $m_1, m_2 \gg m_3$);

- the two primaries follow circular paths around their common centre of mass;

- the motion of the third body is restricted to the orbital plane of the primaries.

As a consequence of the first assumption, it is possible to neglect the gravitational effect of the third body, the spacecraft, onto the two primaries, which persist in their circular motion.

In light of the third assumption, it is possible to simplify the mathematical description as the z coordinate can be neglected. While this assumption is acceptable for current design, the obtained results need to be validated in the more general non-planar case as CI will be placed in a quasi-Halo orbit around L_2 which, by definition, lives in the 3D space. As this analysis is outside the scope of this thesis, a brief description of the issues which arise from the 3D analysis is presented in the concluding Chapter 7.

Whilst for the description of a keplerian orbit, e. g., heliocentric motion, the use of the inertial reference frame, i. e., x-y axes fixed in time (planar case), is well suited, when describing a trajectory in the PCR3BP it is convenient to change description

by moving to a *rotating* or *synodic reference frame*. This arises from the particular selection of 'relative' coordinates used in the literature, Koon et al. [19], Marchal [22], and Valtonen and Karttunen [23]. The origin of the reference system is located at the barycentre of the two primaries, e. g., Sun and Earth, the x-axis is defined by the vector connecting the two primaries, in general pointing from the larger to the smaller one. In order to complete the reference system the z-axis is selected to be perpendicular to the orbital plane and the y-axis is selected in order to obtain a right-handed coordinate-system. As opposed to the traditional inertial reference system, here the x and y axes rotate together with the two primaries, allowing for a better description of the motion relative to the main bodies. In addition, this description is the more natural to detect features like the Lagrangian points.
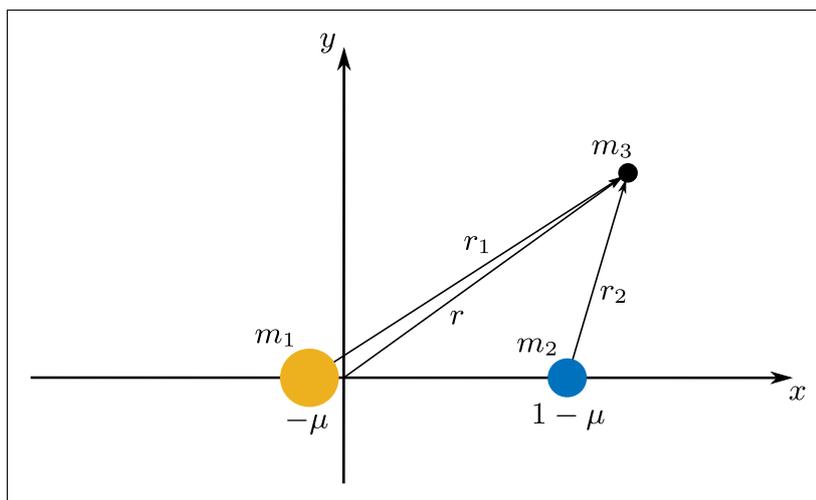
Figure 2.1: Rotating or synodic reference frame for the PCR3BP.

Once the reference system is selected, the problem is *normalized* by selecting particular units for mass, length and time, see Section 2.2. This selection depends on the considered bodies, but in general, the unit mass is considered to be $m_1 + m_2$, the length unit is the distance between the two primaries and, finally, the time unit is selected such that the orbital period of m_1 and m_2 around their barycentre is 2π. Since the reference system is synodic, the two primaries are fixed in position at

$y_{1,2} = 0$, as the problem is planar, a single parameter, the *mass parameter* (μ), is required to fully describe the position of the primaries,

$$\mu = \frac{m_2}{m_1 + m_2} \tag{2.1}$$

in fact, as can be observed in Figure 2.1, they are located at $x_1 = -\mu$ and $x_2 = 1 - \mu$ respectively.

Hereafter, the derivation of the nondimensional equations of motion is summarized based on the work of Koon et al. [19] and Marsden and Ratiu [24]. The equations of motion are derived as the Euler-Lagrange equations, see Eq. 2.6, where the Lagrangian of the system written in the rotating reference frame. The Lagrangian in the planar problem takes the form

$$L\left(x, y, \dot{x}, \dot{y}\right) = K\left(x, y, \dot{x}, \dot{y}\right) - U\left(x, y\right). \tag{2.2}$$

K represents the kinetic energy of the third body and is expressed as

$$K\left(x, y, \dot{x}, \dot{y}\right) = \frac{1}{2}\left(\left(\dot{x} - y\right)^2 \left(\dot{y} + x\right)^2\right). \tag{2.3}$$

After expressing the distances between m_3 and the two primaries as

$$\begin{aligned} r_1 &= \sqrt{\left(x + \mu_2\right)^2 + y^2} \\ r_2 &= \sqrt{\left(x - \mu_1\right)^2 + y^2} \end{aligned} \tag{2.4}$$

the gravitational potential in the rotational reference system can be simply expressed as

$$U\left(x, y\right) = -\frac{\mu_1}{r_1} - \frac{\mu_2}{r_2} - \frac{1}{2}\mu_1\mu_2 \tag{2.5}$$

where $\mu_1 = 1 - \mu$ and $\mu_2 = \mu$. Note, that the last term is a constant which is added to simplify some of the results. This formulation of the Lagrangian arises from the

choice of the reference system and has the characteristic of being *time-independent* since the position relative to the two primaries independent on their rotation.

Finally, the two equations of motion are derived as

$$\frac{\mathrm{d}}{\mathrm{d}t}\frac{\partial L}{\partial \dot{q}^i} - \frac{\partial L}{\partial q^i} = 0 \tag{2.6}$$

where q^i are the generalized coordinates x and y. This leads to the following final form of the equations of motion

$$\begin{aligned} \ddot{x} - 2\dot{y} &= -\bar{U}_x \\ \ddot{y} + 2\dot{x} &= -\bar{U}_y \end{aligned} \tag{2.7}$$

where $\bar{U}$ is the so called *effective potential* and is defined, starting from Eq. 2.5, as

$$\bar{U}(x,y) = -\frac{1}{2}(x^2 + y^2) + U(x,y).$$

2.1.1 *Lagrangian or Libration Points*

The above described equations of motion, see Eq. 2.7, yield particular solutions when all acceleration and velocity terms are equal to zero. The solution of the obtained system of equations, described by Koon et al. [19, Ch. 2.5], leads to the 'discovery' of 5 equilibrium points called *Lagrangian* or *Libration Points*, identified hereafter as L_i with $i = 1, ..., 5$. Looking at Eq. 2.7, it is clear that the points of interest are identified by $\frac{d\bar{U}}{dq^i} = 0$, and are thus stationary points for the effective potential.

From Figure 2.2, it can be seen that the first three libration points are positioned on the same line as the two primaries ($y = 0$), and are thus referred as *collinear* points. The other two points are located at the third corners of the equilateral triangles which have as base the segment connecting the two primaries. As previously introduced,
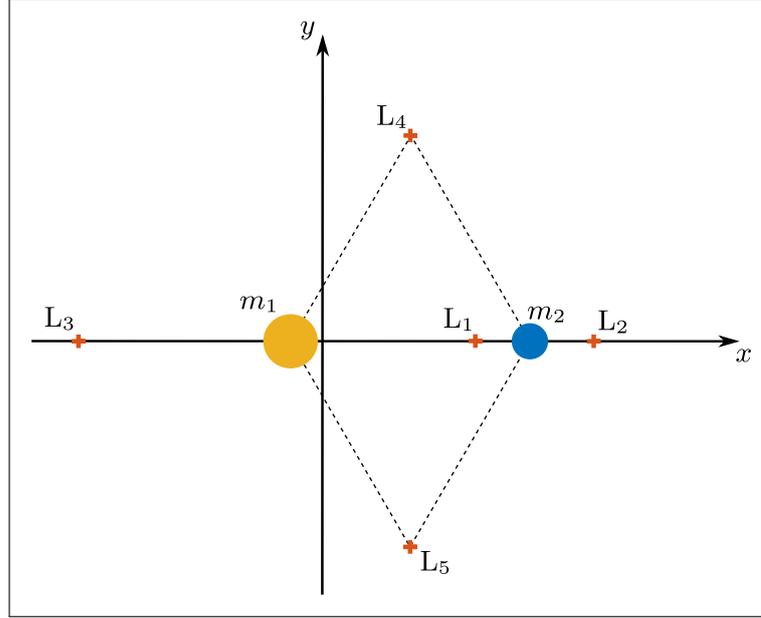
Figure 2.2: Location of the Libration or Lagrangian Points in the synodic reference frame.

the obtained coordinates are stationary points for the effective potential. As such, a spacecraft placed exactly at these coordinates will remain stationary with respect to the rotating reference frame.

As Comet Interceptor will be placed around L_2, the following discussion will only focus on this specific point. Although one of its coordinates is known, its exact position on the x-axis is still unknown. Simplifying the stationarity condition of $\bar{U}$ to $\frac{d\bar{U}}{dx}(x,0) = 0$ for this particular case, leads to Eq. 2.8 giving an implicit equation that depends only on the mass parameter of the specific system and on the position of L_2 with respect to the smaller primary, γ. The solution can be promptly identified by numerical methods, e. g., Newton Method, starting from the *Hill's Radius*, $r_h = (\mu/3)^{1/3}$, as the initial guess [25].

$$\gamma^5 + (3 - \mu)\gamma^4 + (3 - 2\mu)\gamma^3 - \mu\gamma^2 - 2\mu\gamma - \mu = 0 \tag{2.8}$$

Obviously, in reality this is impossible to achieve, and thus the stability of each point needs to be analysed in order to understand the motion in its vicinity. The

motion close to the equilibrium points is analysed considering the linearised form of the first derivatives of $\bar{U}$, Eq. 2.9. The obtained qualitative results are valid also for the full nonlinear analysis [26].

$$
\begin{aligned}
\ddot{x} - 2\dot{y} &= -\left(x\frac{\partial^2 \bar{U}}{\partial x^2} + y\frac{\partial^2 \bar{U}}{\partial x \partial y} \right) \\
\ddot{y} + 2\dot{x} &= -\left(x\frac{\partial^2 \bar{U}}{\partial x \partial y} + y\frac{\partial^2 \bar{U}}{\partial y^2} \right)
\end{aligned}
\tag{2.9}
$$

For the sake of brevity, the detailed analysis is not reported here but can be found in the work of Szebehely [25] and Hagihara [27]. For the continuation of this work it is sufficient to remember that, while L_4 and L_5 could be stable in particular cases, e. g., Sun-Jupiter system, the collinear points, and in particular L_2, are always unstable.

2.1.2 *Jacobi integral*

As mentioned, the obtained equations of motion are time-independent as they describe the motion in the rotating reference frame. This characteristic of the PCR3BP allows for the derivation of an energy integral of motion known as *Jacobi constant* or *Jacobi integral*. In fact, starting with the summation of the two equations of motion, multiplied respectively by $\dot{x}$ and $\dot{y}$, leads to:

$$
\ddot{x}\dot{x} - 2\dot{y}\dot{x} = -\bar{U}_x\dot{x}
$$

$$
\Rightarrow \qquad \ddot{x}\dot{x} + \ddot{y}\dot{y} = -\bar{U}_x\dot{x} - \bar{U}_y\dot{y}
\tag{2.10}
$$

$$
\ddot{y}\dot{y} + 2\dot{x}\dot{y} = -\bar{U}_y\dot{y}
$$

As the effective potential is time independent, the right hand side of Eq. 2.10 represents the full derivative of $\bar{U}$. Furthermore, the left hand side can be rewritten in

terms of the velocity components of the spacecraft in the synodic reference frame, leading to the following equation [23, Ch. 5.3].

$$\frac{d}{dt}\left(\dot{x}^2 + \dot{y}^2\right) = 2\frac{d\bar{U}}{dt}$$

Integrating this over time gives the definition of the *Jacobi constant*, see Eq. 2.11.

$$\begin{aligned}
C\left(x,y,\dot{x},\dot{y}\right) &= -\left(\dot{x}^2 + \dot{y}^2\right) - 2\bar{U}\left(x,y\right) \\
&= -\left(\dot{x}^2 + \dot{y}^2\right) + x^2 + y^2 + 2\frac{\mu_1}{r_1} + 2\frac{\mu_2}{r_2} + \mu_1\mu_2
\end{aligned} \tag{2.11}$$

Given the fact that the velocity of the spacecraft (i.e., $\sqrt{\dot{x}^2 + \dot{y}^2}$) cannot be negative, the motion is bounded in a specific region which depends on C, in particular, the spacecraft is allowed to move only where $\bar{U}(x,y) \geq C/2$ is verified. This condition divides the x-y plane (in the planar case) in two regions, one accessible and one inaccessible, their boundary is defined by the *zero-velocity curve*, i.e., where $\bar{U}(x,y) = C/2$. These regions can have different topologies depending on the initial value of C, the different possibilities are represented in Figure 2.3 for different values of C. Note that, as the Jacobi Constant is an integral of motion, and is thus constant over time, the topology of the region cannot change without considering propulsive manoeuvres or gravity assists. Note that, from this analysis, it is not possible to determine the actual trajectory of the satellite, but only the possible regions of motion. In order to determine the trajectory it is necessary to integrate numerically Eq. 2.7.

Throughout this work, the terms *Jacobi Constant, Jacobi Integral, energy* will refer to the same concept, i.e., the fundamental integral of motion in the PCR3BP. When required the, the difference will be clarified by the context, as the increase in energy is associated to a decrease of the Jacobi Constant and vice versa.
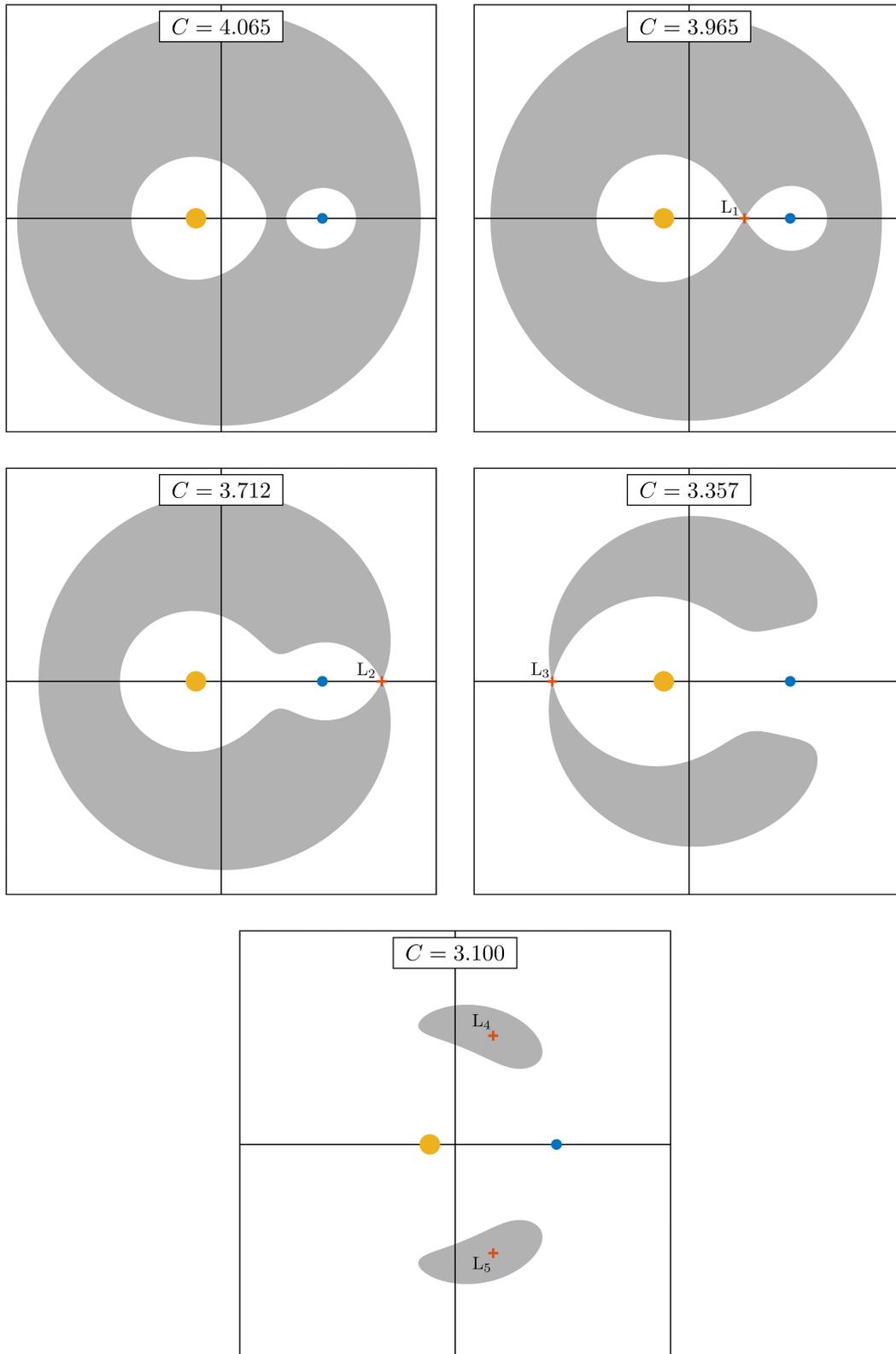
Figure 2.3: Zero-velocity curves for five values of the Jacobi constant for $\mu = 0.2$. The zones in white are accessible to the spacecraft with a specific energy value. The motion is bounded by the shaded zones known as *forbidden realm*.

2.2   PATCHED CR3BP DEFINITION

Following the description of various authors, such as Qi and Xu [21] and Castelli [28], in order to obtain a good approximation of the PBCM, see Figure 2.4 it is possible to divide the x-y plane in two separate regions, and thus in two distinct problems:

- one region around the Earth-Moon system, here the trajectory is well approximated by the PCR3BP having the Earth and the Moon as the two primaries. While the Sun still influences the trajectory, its impact is negligible with respect to the one of the two primaries;

- a second region surrounding the first one, here the gravity of the Moon alone is negligible with respect to the one of the Sun and the Earth; thus, a second PCR3BP is defined considering as the first primary the Sun and as the second one the Earth-Moon barycentre.

Clearly, during the overall mission, the spacecraft is not bound inside of one of these regions, in fact, given the relative positions of the Earth-Moon sphere and the L_2 libration point (located outside of it) and the nature of the mission, the trajectory necessarily will cross both regions.
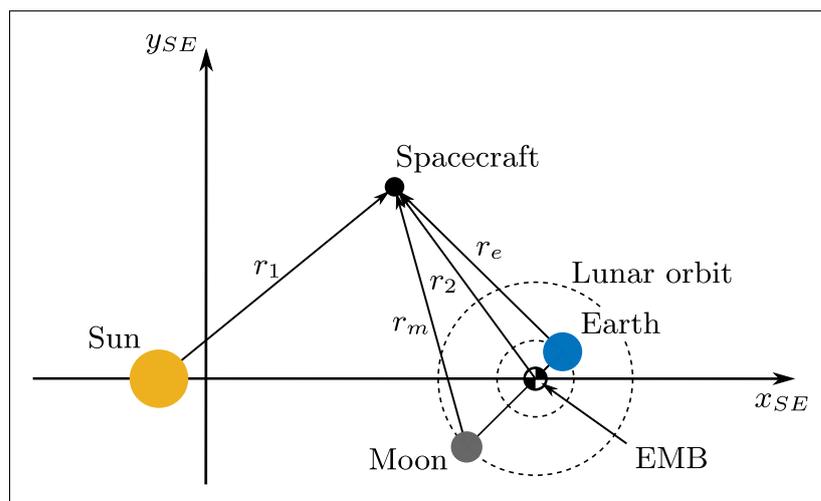
Figure 2.4: PBCM reference frame [21].

When working with the PCR3BP it is fundamental to consider normalized units of mass, length and time. As the normalization process is dependent on the characteristics of the individual system, here two sets of dimensional values are required. While, the length and time units maintain the same definition, i. e., distance between the two primaries and time unit such that the orbital period of the primaries is 2π, the mass parameter changes slightly its definition

$$\mu_{SE} = \frac{m_\oplus + m_\mathbb{C}}{m_\odot + (m_\oplus + m_\mathbb{C})} \qquad\qquad \mu_{EM} = \frac{m_\mathbb{C}}{m_\oplus + m_\mathbb{C}}$$

the subscripts $_{SE}$ and $_{EM}$ refer to the Sun-EMB system and to the Earth-Moon system respectively and are used throughout the analysis when referring not only to the normalization units but also to other features of the specific reference frames, e. g., Sphere of Influence (SOI), coordinates, etc. The relationships listed in Eq. 2.12 [19, Ch. 2.2] show how to pass from dimensional quantities, variables with a tilde, to nondimensional quantities, without tilde (following the nomenclature of Campagnola and Russell [29]).

$$
\begin{aligned}
\text{length:} \qquad & l = \frac{\widetilde{l}}{L^*}, \\
\text{time:} \qquad & t = \frac{2\pi\widetilde{t}}{T} = \frac{\widetilde{t}}{T^*}, \\
\text{velocity:} \qquad & v = \widetilde{v}\frac{T}{2\pi L} = \frac{\widetilde{v}}{V^*}
\end{aligned}
\tag{2.12}
$$

The coefficients normalization are listed in Table 2.1

	Sun-EMB ($i =_{SE}$)	Earth-Moon ($i =_{EM}$)
L_i^*, km	1.496×10^8	3.844×10^5
T_i^*, s	5.019×10^6	3.758×10^5
V_i^*, km/s	29.806	1.023

Table 2.1: Length, time and velocity units of Sun-EMB and Earth-Moon systems, data from DITAN software and by Wertz, Everett, and Puschell [30].

After defining the units for the normalization it is also necessary to define the two reference frames and which is the boundary between them. First, let's introduce the two reference frames, as discussed in Section 2.1, in the PCR3BP the two primaries are located on the x-axis at a distance of respectively $-\mu$ and $1-\mu$ from the origin. The two reference frames are represented in Figure 2.5. Note that, given the four orders of magnitude of difference between μ_{SE} and μ_{EM}, the 'shape' of the system varies slightly, specifically, the Sun is much closer to the origin of its system than the Earth is to the EMB, the numerical values are computed as μL^* for each system.
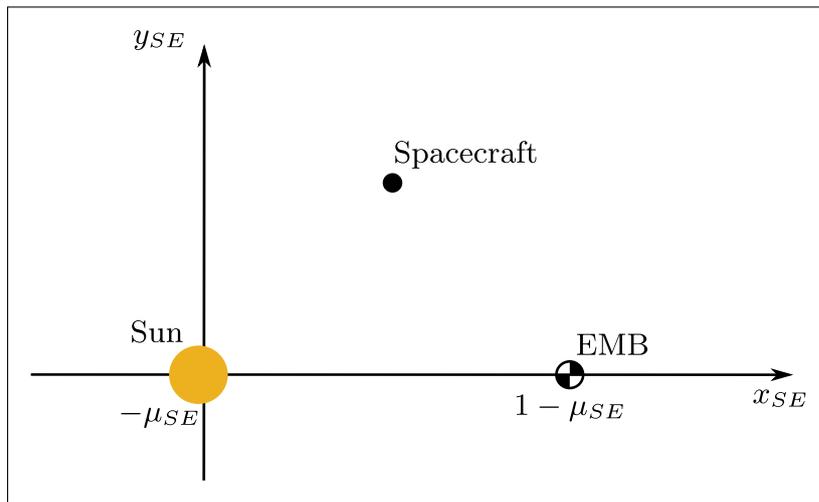
(a)
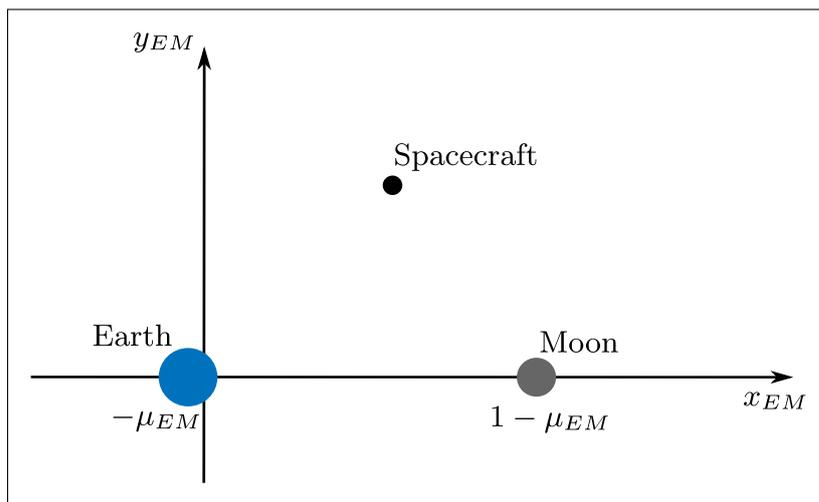
(b)

Figure 2.5: Synodic reference frames of the Sun-EMB (a) and the Earth-Moon (b) reference frames as described by Qi and Xu [21].

As the two reference frames move in time it is necessary to define their position relative to an inertial reference frame, identified by the *X-Y* plane. In fact, as the origin of the Sun-EMB system is stationary, the angle θ_{SE} is sufficient to completely define its relative position, see Figure 2.6. A similar consideration is made for the Earth-Moon system, but defining its position relative to the Sun-EMB system as, again, its origin is fixed in this system, and thus the relative angle $\theta_M = \theta_{EM} - \theta_{SE}$ is sufficient to describe completely its position.
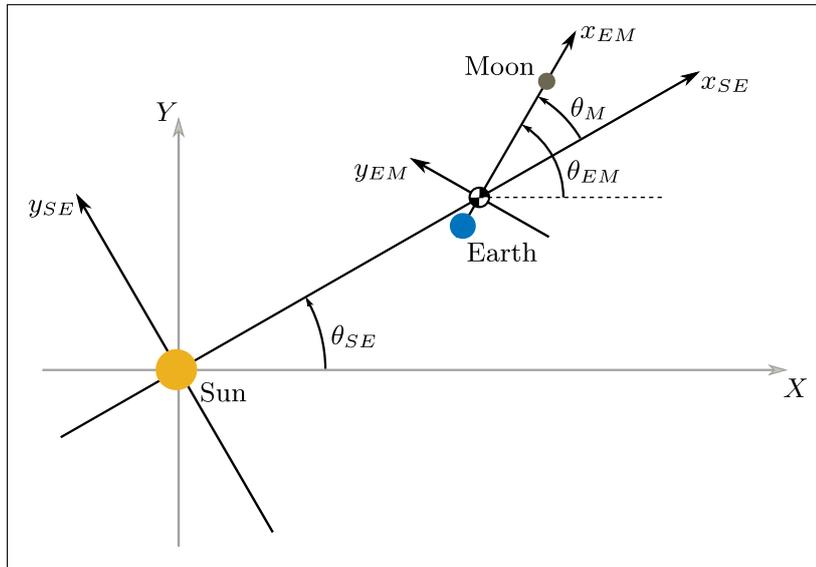
Figure 2.6: Positions of the Sun-EMB and Earth-Moon PCR3BP reference frames with respect to an inertial reference frame.

Furthermore, as the following analysis is performed solely in the synodic reference frames, θ_{SE} and θ_{EM} become irrelevant and the only angle used hereafter is θ_M. Note that, as the EMB and the Earth centre almost coincide, the relative angle between x_{EM} and x_{SE} is approximately the *lunar phase angle*, i.e., the angle between the Sun-Earth and the Earth-Moon directions.

Now that the reference frames are defined it is possible to analyse the boundary for the 'patched' approach. Different approaches for the study are followed by authors like Qi and Xu [21] and Castelli [28]. The former analyses the the variability of the Jacobi Constant, which for the restricted problem should be time invariant as

opposed to the four body model where it depends on the Moon position, and thus on time. On the other hand, the latter uses the difference of the norm of the accelerations governing the dynamics in the PBCM and in the two PCR3BP models once they are written in the same units and same reference systems (depending on which restricted problem is investigated).

While both approaches give similar results, hereafter only the first approach is briefly presented, for a detailed analysis see Qi and Xu [21, Ch. 3.2]. Starting from the definition of C, Eq. 2.11, and the PBCM equations of motion in the dimensionless Sun-EMB reference frame, see Figure 2.4,

$$
\begin{aligned}
\ddot{x}_{SE} - 2\dot{y}_{SE} &= \frac{\partial \bar{U}_4^{SE}}{\partial x_{SE}} \\
\ddot{y}_{SE} + 2\dot{x}_{SE} &= \frac{\partial \bar{U}_4^{SE}}{\partial y_{SE}}
\end{aligned}
\tag{2.13}
$$

where $\bar{U}_4^{SE}$ is an variation of the three body effective potential, and is defined as

$$
\bar{U}_4^{SE}(x_{SE}, y_{SE}, t) = -\bar{U}_3^{SE}(x_{SE}, y_{SE}) + \Phi(x_{SE}, y_{SE}, t)
\tag{2.14}
$$

$$
\Phi(x_{SE}, y_{SE}, t) = \mu_{SE} \left[\frac{\mu_{EM}}{r_m(x_{SE}, y_{SE}, t)} + \frac{1 - \mu_{EM}}{r_e(x_{SE}, y_{SE}, t)} - \frac{1}{r_2(x_{SE}, y_{SE})} \right]
$$

with r_m, r_e and r_2 defined as in Figure 2.4, the variation of C over time can be written as

$$
\begin{aligned}
\frac{\mathrm{d}C}{\mathrm{d}t_{SE}} &= -2(\dot{x}_{SE}\ddot{x}_{SE} + \dot{y}_{SE}\ddot{y}_{SE}) - 2\frac{\mathrm{d}\bar{U}_3^{SE}}{\mathrm{d}t_{SE}} \\
&= -2\left(\dot{x}_{SE}\frac{\partial \bar{U}_4^{SE}}{\partial x_{SE}} + \dot{y}_{SE}\frac{\partial \bar{U}_4^{SE}}{\partial y_{SE}} \right) - 2\frac{\mathrm{d}\bar{U}_3^{SE}}{\mathrm{d}t_{SE}}
\end{aligned}
\tag{2.15}
$$

Through the introduction of further definitions and the integration over $t_S E$, not shown here for the sake of brevity, an indicator of the accuracy of the approximation is obtained as

$$
C^* - C = 2\Phi
\tag{2.16}
$$

where C^* is the Jacobi Constant at infinity and C and Φ are evaluated at the same position. As the Jacobi Constant should not change, the magnitude of Φ is a direct sign if the PCR3BP is a good approximation of the PBCM, in fact as discussed in the mentioned paper, $\left|\frac{2\Phi}{C^*}\right| \leq 10^{-5}$ is considered as a suitable condition. In Figure 2.7 it can be observed that only a specific region, represented in the Earth-Moon reference frame, does not respect the requested condition, and thus is not suited for the Sun-EMB PCR3BP approximation.
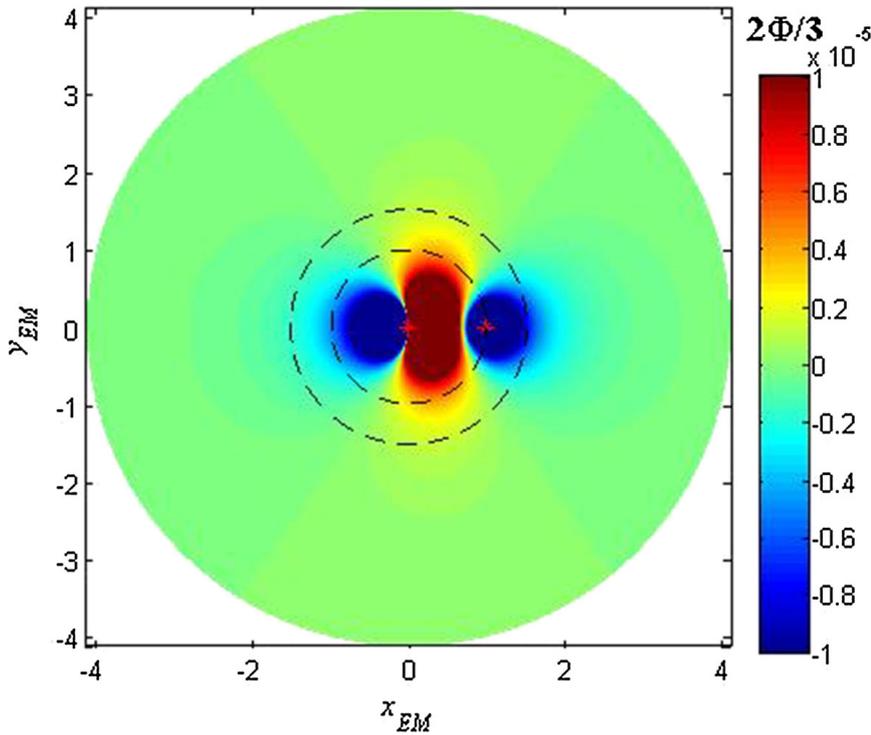
Figure 2.7: Distribution of the indicator function for the Sun-EMB PCR3BP approximation for a trajectory with $C^* \approx 3$ [21].

The inner circle in the figure represents the lunar orbit, the outer radius is $200\,000$ km larger and includes the above mentioned regions; thus, it is taken as the *boundary* between the the Sun-EMB problem, external region, and the Earth-Moon problem, internal region.

2.2.1 *Poincaré Map/Section*

A *Poincaré Map* is a useful tool when dealing with the dynamics of the CR3BP. A map is obtained by propagating a set of initial conditions and displaying the 'points' at which the obtained trajectories cross a particular surface Σ.

The use of Poincaré Maps reduces the dimensionality of the problem, in particular, considering the PCR3BP and fixed levels of the Jacobi Constant, it is possible to describe the full state space with a 2D representation. As an example, the use of Poincaré Maps is widely used in the design of free heteroclinic or homoclinic transfers between L_1 and L_2 periodic orbits [31–35]. In Figure 2.8 the two possible transfer trajectories are represented by the Poincaré sections of the L_1 unstable manifold (in red) and the L_2 stable manifold (in blue) in the Earth-Moon planar problem [36].
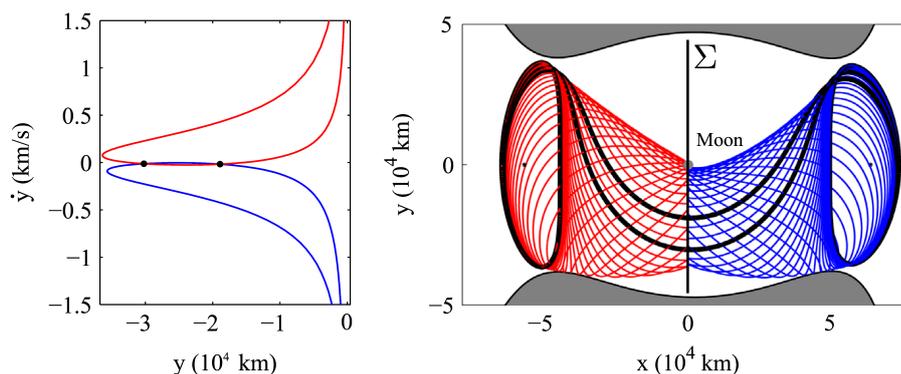
Figure 2.8: Example of y-$\dot{y}$ Poincaré Map used for the identification of heteroclinic transfers between L_1 and L_2 in the PCR3BP [36].

2.2.2 *Coordinates Transformation*

To correctly propagate a trajectory crossing both rotating reference frames, it is necessary to describe an algorithm to transform the coordinates from one system to the other. Such an algorithm is described by Koon et al. [19, Ch. 5.3] and reported hereafter.

Lets first define the notation:

- the superscripts indicate the type of system, in stands for inertial and ro stands for rotational;

- vectors are written in bold, e. g., $\mathbf{x}_A^{ro} = [x\ y\ u\ v]^T$ where x and y are the position components and u and v are the associated velocities;

- for brevity $c = \cos\theta(t)$ and $s = \sin\theta(t)$ where $\theta(t) = t + \theta_0$ is the angle between a specific reference frame and the inertial one, i. e., θ_{SE} or θ_{EM}.

The first step is to transform the coordinates from the synodic reference frame to the inertial one

$$\mathbf{x}_{SE}^{in} = \mathbf{R}(\mathbf{x}_{SE}^{ro} - \mathbf{d}_{SE}) \tag{2.17}$$

$$\mathbf{R} = \begin{pmatrix} R_{11} & 0 \\ R_{21} & R_{22} \end{pmatrix}$$

$$R_{11} = R_{22} = \begin{pmatrix} c & -s \\ s & c \end{pmatrix}, \qquad R_{21} = \begin{pmatrix} -s & -c \\ c & -s \end{pmatrix}$$

it is clear that this transformation does not only involve a rotation but also a translation under the form of $\mathbf{d}_{SE}$. This is necessary in order to move from a reference frame centred at the barycentre to one located at the Sun or at the EMB; thus, $\mathbf{d}_{SE} = [x_{SE}^0\ 0\ 0\ 0]^T$ where x_{SE}^0 is either $-\mu_{SE}$, Sun centred, or $1 - \mu_{SE}$, EMB centred.

The so obtained state vector is still normalized with the units of the Sun-EMB system; thus, it is necessary to change the normalization as follows

$$\text{length:} \qquad l_{EM} = \frac{L_{SE}^*}{L_{EM}^*} l_{SE},$$

$$\text{time:} \qquad t_{EM} = \frac{T_{SE}^*}{T_{EM}^*} t_{SE},$$

$$\text{velocity:} \qquad v_{EM} = \frac{V_{SE}^*}{V_{EM}^*} v_{SE}.$$

which translates into

$$\mathbf{x}_{EM}^{in} = \frac{L_{SE}^*}{L_{EM}^*}\begin{bmatrix} x_{SE,1}^{in} \\ x_{SE,2}^{in} \\ 0 \\ 0 \end{bmatrix} + \frac{V_{SE}^*}{V_{EM}^*}\begin{bmatrix} 0 \\ 0 \\ x_{SE,3}^{in} \\ x_{SE,4}^{in} \end{bmatrix}.$$

Finally it is possible to pass again from the inertial reference frame to the desired synodic frame, obtaining the final state vector:

$$\mathbf{x}_{EM}^{ro} = \mathbf{R}^{-1}\mathbf{x}_{EM}^{in} + \mathbf{d}_{EM}, \tag{2.18}$$

where, similarly to the previous case, $\mathbf{d}_{EM} = [x_{EM}^0\ 0\ 0\ 0]^T$ where x_{EM}^0 is either $-\mu_{EM}$, Earth centred, or $1 - \mu_{EM}$, Moon centred. Two considerations are worth mentioning:

- the rotation matrix, $\mathbf{R}$, needs to be adapted to the specific case as the time t is normalized differently for the two systems and the angle θ_0 is specific for each reference frame;

- the most intuitive centre for the inertial reference frame is obviously the Earth as it can be considered as the 'junction' between the two systems. This leads to the selection of: $x_{SE}^0 = 1 - \mu_{SE}$ and $x_{EM}^0 = -\mu_{EM}$

Note that this algorithm, written as such, transforms the state from the Sun-EMB to the Earth-Moon system. Obviously, with slight variations, the same algorithm is used also for the opposite transformation.

2.3 DIFFERENTIAL CORRECTION

When designing a trajectory, generally, some type of constraints need to be respected for the success of the mission. In order to implement these constraints in the three-body problem, a set of numerical tools needs to be applied to find the desired results, as, on the contrary to the two body problem where analytical analysis is possible, here numerical computation is the only way to go.

Once the dynamical model is defined, Eq. 2.7, the trajectory is uniquely defined by some initial (or final) conditions that are propagated forwards (or backwards) over a certain amount of time. In mathematical terms, the full trajectory is expressed as a single function denoted as the *flow map* as it maps the motion of the spacecraft from t_0 to time t. Since, the trajectory is uniquely defined

$$\Phi(t_0, t_1, \mathbf{x}_0) = \mathbf{x}_1. \tag{2.19}$$

Nonetheless, if the objective is to respect some constraints, for example on the final state, the initial condition needs to be precisely determined, especially in chaotic problems as the PCR3BP. For this purpose the *differential corrector* is applied, its aim is to evaluate the necessary variations of the initial conditions lead to the fulfilment of the required constraints. The following discussion is based on the work of different authors such as [19, 37]

In general, when a perturbation, $\delta\mathbf{x}_0$ is applied to the initial state, the entire trajectory will evolve in a different way leading to a different final condition, this is observed through the flow map.

$$\Phi(t_0, t_1, \mathbf{x}_0 + \delta\mathbf{x}_0) = \mathbf{x}_f$$

The difference between the two final states is obtained as

$$\delta\mathbf{x}(t) = \mathbf{x}_f - \mathbf{x}_1 = \Phi(t_0,t_1,\mathbf{x}_0 + \delta\mathbf{x}_0) - \Phi(t_0,t_1,\mathbf{x}_0) \neq \delta\mathbf{x}_0 \qquad (2.20)$$
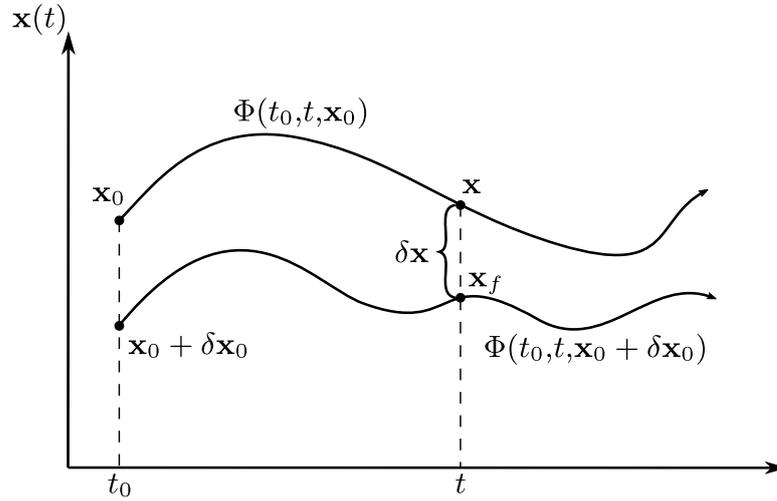
Figure 2.9: Visualization of the concept of Flow Map with initial conditions $\mathbf{x}_0$ and $\mathbf{x}_0 + \delta\mathbf{x}_0$.

Expanding the Taylor series of Eq. 2.20 to the first-order leads to an approximation of the desired quantity

$$\delta\mathbf{x}(t) \approx \Phi(t_0,t_1,\mathbf{x}_0) + \frac{\partial\Phi(t_0,t_1,\mathbf{x}_0)}{\partial\mathbf{x}_0}\delta\mathbf{x}_0 - \Phi(t_0,t_1,\mathbf{x}_0) = \frac{\partial\Phi(t_0,t_1,\mathbf{x}_0)}{\partial\mathbf{x}_0}\delta\mathbf{x}_0 \quad (2.21)$$

A linear relationship between between the two perturbations can be highlighted by defining the State Transition Matrix (Φ), see Eq. 2.22. Note that this approximation is accurate only for t_1 close to t_0 due to the fact that all higher order terms are neglected.

$$\Phi(t_0,t) = \frac{\partial\Phi(t_0,t,\mathbf{x}_0)}{\partial\mathbf{x}_0} \qquad (2.22)$$

As no analytical solution is present, $\boldsymbol{\Phi}$ needs to be integrated alongside the actual trajectory. To do so, a set of first-order differential equation of the form $\dot{\boldsymbol{\Phi}} = \mathbf{F}(\boldsymbol{\Phi})$ is derived starting from Eq. 2.22

$$\dot{\boldsymbol{\Phi}} = \frac{\partial \Phi(t_0,t,\mathbf{x}_0)}{\partial t} = \frac{\partial}{\partial t}\left(\frac{\partial \mathbf{x}}{\partial \mathbf{x}_0}\right) \tag{2.23}$$

The last term of the equation can be rewritten as $\frac{\partial}{\partial \mathbf{x}_0}\left(\frac{\partial \mathbf{x}}{\partial t}\right)$ since $\mathbf{x}_0$ and t are independent. In order to recover the desired form of the equation, the chain rule is applied to Eq. 2.23

$$\dot{\boldsymbol{\Phi}}(t_0,t) = \frac{\partial}{\partial \mathbf{x}_0}\left(\mathbf{F}(\mathbf{x}_0)\right) = \frac{\partial \mathbf{F}}{\partial \mathbf{x}} \cdot \frac{\partial \mathbf{x}}{\partial \mathbf{x}_0} = \frac{\partial \mathbf{F}}{\partial \mathbf{x}}\left(\mathbf{x}(t)\right) \cdot \boldsymbol{\Phi}(t_0,t)$$

Leading to the final form of the first-order differential equation which describes the evolution of the State Transition Matrix

$$\dot{\boldsymbol{\Phi}} = \frac{\partial \mathbf{F}}{\partial \mathbf{x}} \cdot \boldsymbol{\Phi} \tag{2.24}$$

The obtained equation is integrated starting from a known initial condition, but, as at $t = t_0$ $\delta\mathbf{x} = \delta\mathbf{x}_0$, by definition $\boldsymbol{\Phi}(t_0,t_0) = I_{4\times4}$. Note that $\boldsymbol{\Phi}$ is a 4-by-4 matrix because the planar problem is considered. It is fundamental to observe that, in Eq. 2.24, $\frac{\partial \mathbf{F}}{\partial \mathbf{x}}$ is the Jacobian matrix $\mathbf{J}(t)$ of the considered dynamical model, in this case the PCR3BP, which is evaluated together with the reference solution.

In the particular case of the PCR3BP the Jacobian is written as follows

$$\mathbf{J}(t) = \begin{bmatrix} 0 & 0 & 1 & 0 \\ 0 & 0 & 0 & 1 \\ & & 0 & 2 \\ & Q & -2 & 0 \end{bmatrix} \quad \text{with} \quad Q = \begin{bmatrix} \frac{\partial \ddot{x}}{\partial x} & \frac{\partial \ddot{x}}{\partial y} \\ \frac{\partial \ddot{y}}{\partial x} & \frac{\partial \ddot{y}}{\partial y} \end{bmatrix}$$

Where the partial derivatives are

$$\frac{\partial \ddot{x}}{\partial x} = 1 - \frac{1 - \mu_{SE}}{r_1{}^3} - \frac{\mu_{SE}}{r_2{}^3} + 3\frac{1 - \mu_{SE}}{r_1{}^5}(x - x_1)^2 + 3\frac{\mu_{SE}}{r_2{}^5}(x - x_2)^2$$

$$\frac{\partial \ddot{y}}{\partial y} = 1 - \frac{1 - \mu_{SE}}{r_1{}^3} - \frac{\mu_{SE}}{r_2{}^3} + 3\frac{1 - \mu_{SE}}{r_1{}^5}y^2 + 3\frac{\mu_{SE}}{r_2{}^5}y^2$$

$$\frac{\partial \ddot{x}}{\partial y} = \frac{\partial \ddot{y}}{\partial x} = 3\frac{1 - \mu_{SE}}{r_1{}^5}(x - x_1)y + 3\frac{\mu_{SE}}{r_2{}^5}(x - x_2)y$$

where x_1 and x_2 are respectively the positions of the first and the second primaries, e.g., Sun and EMB, and r_1 and r_2 are defined in .
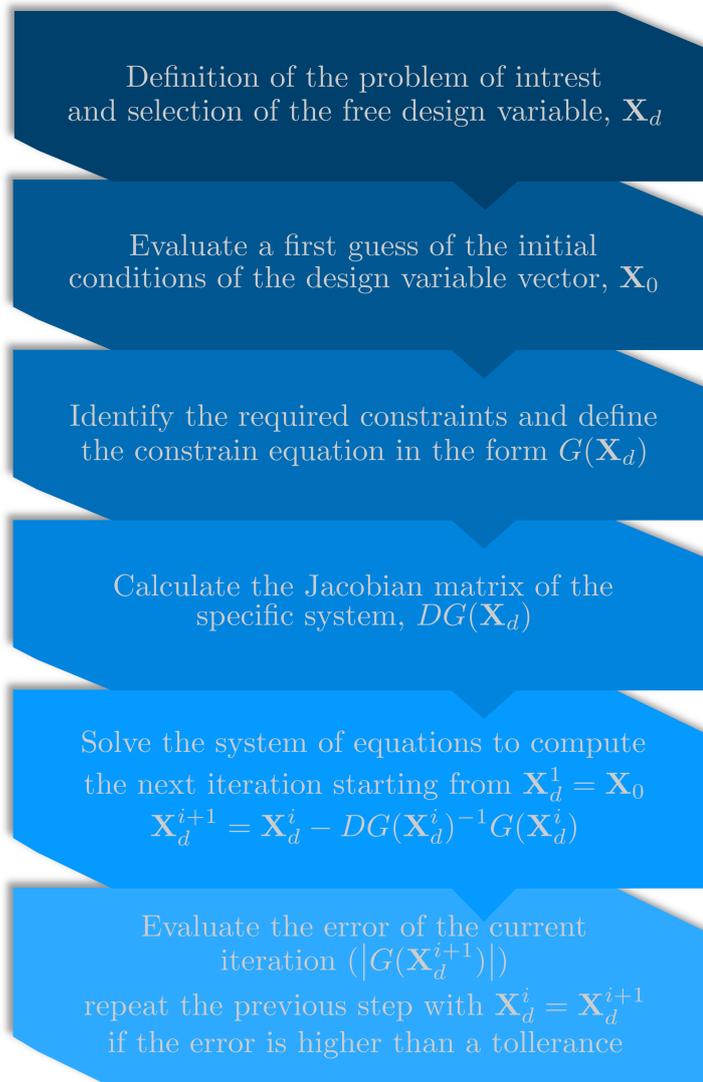
Figure 2.10: Outline of the general differential correction algorithm.

Although the algorithm finds application in a variety of fields, here it is specified for the problem at hand, i. e., the targeting of the desired location of the lunar gravity assist, $\mathbf{x}_{ga}$. Given the problem at hand, the selected design variables are the velocity components at $t = t_0$.

$$\mathbf{X}_d = \begin{bmatrix} \dot{x}_0 \\ \dot{y}_0 \end{bmatrix} \tag{2.25}$$

Note that, for the problem at hand, the *tof* is not a design variable as the location for the gravity assist is strictly bound to the timing problem. As introduced, the objective is to find the correct perturbation of the initial velocity components, the design variables, to reach the correct location for the gravity assist. This means that the *constraints* are written as functions of $\mathbf{x}_{ga}$; and thus,

$$G(\mathbf{X}_d) = \mathbf{\Phi}(t_0, t_0 + tof, \mathbf{x}_0) - \mathbf{x}_{ga} = \begin{bmatrix} x - x_{ga} \\ y - y_{ga} \end{bmatrix} \tag{2.26}$$

The objective of the algorithm is to find $\mathbf{X}_d$ such that $G(\mathbf{X}_d) = 0$, to do so an iterative method is derived starting from the first-order Taylor Series of Eq. 2.26 computed around an initial guess $\mathbf{X}_0$.

$$G(\mathbf{X}_d) = G(\mathbf{X}_0) + \frac{\partial G}{\partial \mathbf{X}_d}(\mathbf{X}_d - \mathbf{X}_0) \tag{2.27}$$

Looking at Eq. 2.25 and Eq. 2.26 it can be noted that they have the same dimensionality, i. e., there are the same number of design variables and constraints. As a consequence, the iterative equation is easily written starting from Eq. 2.27,

$$\mathbf{X}_d^{i+1} = \mathbf{X}_d^i - DG(\mathbf{X}_d^i)^{-1}G(\mathbf{X}_d^i) \tag{2.28}$$

where the first iteration starts with $\mathbf{X}_0$. It is possible to write the equation in this form as $DG(\mathbf{X}_d) = \frac{\partial G(\mathbf{X}_0)}{\partial \mathbf{X}_d}$ is square and can thus be inverted. In particular, in this

case, its components are the same as the components of the $\boldsymbol{\Phi}$ that correlate the velocity components of the initial state and the position of the final state.

$$DG(\mathbf{X}_d) = \frac{\partial G(\mathbf{X}_0)}{\partial \mathbf{X}_d} = \begin{bmatrix} \frac{\partial x}{\partial \dot{x}_0} & \frac{\partial x}{\partial \dot{y}_0} \\ \frac{\partial y}{\partial \dot{x}_0} & \frac{\partial y}{\partial \dot{y}_0} \end{bmatrix} = \begin{bmatrix} \boldsymbol{\Phi}_{13} & \boldsymbol{\Phi}_{14} \\ \boldsymbol{\Phi}_{23} & \boldsymbol{\Phi}_{24} \end{bmatrix} \qquad (2.29)$$

The final form of Eq. 2.28 is

$$\begin{bmatrix} \dot{x}_0 \\ \dot{y}_0 \end{bmatrix}^{i+1} = \begin{bmatrix} \dot{x}_0 \\ \dot{y}_0 \end{bmatrix}^{i} - \begin{bmatrix} \boldsymbol{\Phi}_{13} & \boldsymbol{\Phi}_{14} \\ \boldsymbol{\Phi}_{23} & \boldsymbol{\Phi}_{24} \end{bmatrix}^{-1} \begin{bmatrix} x - x_{ga} \\ y - y_{ga} \end{bmatrix} \qquad (2.30)$$

At each iteration of the above equation it is necessary to compute the residual error on the constraint equations, in fact, as in Eq. 2.21 a linearisation is considered, the longer the considered time span for the integration the higher the error on the constraints. This means that the convergence of the method can be observed by looking at

$$\left| G(\mathbf{X}_d^{i+1}) \right|$$

The iterations are stopped when the error associated to the last iteration is less than a fixed tolerance ϵ.

2.4 TWO-BODY FLYBY

While in the 'patched' PCR3BP the consequences of the passage in the vicinity of the Moon arise naturally, it is quite cumbersome to perform the design and optimisation of the desired trajectory within this model. Thus, initially, it is preferred to neglect the lunar gravitational field up until the spacecraft enters the SOI of the Moon, with radius of $66\,200$ km [16, App. A], moving to a more traditional patched 'conic' approach, where two separate trajectories in the PCR3BP are patched by an instantaneous rotation of the velocity vector [19, Ch. 8.9].

The study of this rotation is performed under the assumption of the Two Body Problem, where the main body is represented by the Moon and all other gravitational forces are neglected. This results in the study of an hyperbolic trajectory relative to the Moon.

To analyse the effect of the lunar flyby the *relative velocity vector* between the Moon and the spacecraft is computed

$$\mathbf{v}_{r,1} = \mathbf{v}_1 - \mathbf{v}_{\mathbb{C}} \tag{2.31}$$

where $\mathbf{v}_1$ is the nondimensional velocity of the spacecraft in the Sun-EMB syndic reference frame and $\mathbf{v}_{\mathbb{C}}$ is the velocity of the Moon. Note that, since in the considered reference frame the Earth is fixed in position, the lunar velocity is tangential to its orbit around the Earth and is computed as $1/V_{SE}^* \sqrt{\mu_{\oplus}/a_{\mathbb{C}}}$ where $a_{\mathbb{C}} = \widetilde{a}_{\mathbb{C}}/L_{SE}^* = 0.0026$ is the nondimensional radius of the lunar orbit.

The post-flyby conditions not only depend on the relative velocity but also on the type of approach. In particular there are two types:

- leading-side flyby, Figure 2.11a: here the spacecraft passes in front of the Moon, in this case the spacecraft loses energy as it reduces its speed in the Sun-EMB system. In the case of a *prograde* hyperbola, a counter-clockwise rotation is obtained, the opposite is true for a *retrograde* hyperbola

- trailing-side flyby, Figure 2.11b here the spacecraft passes behind of the Moon, in this case the spacecraft gains energy as it increases its speed in the Sun-EMB system. The rotation is opposite as for the leading-side flyby.
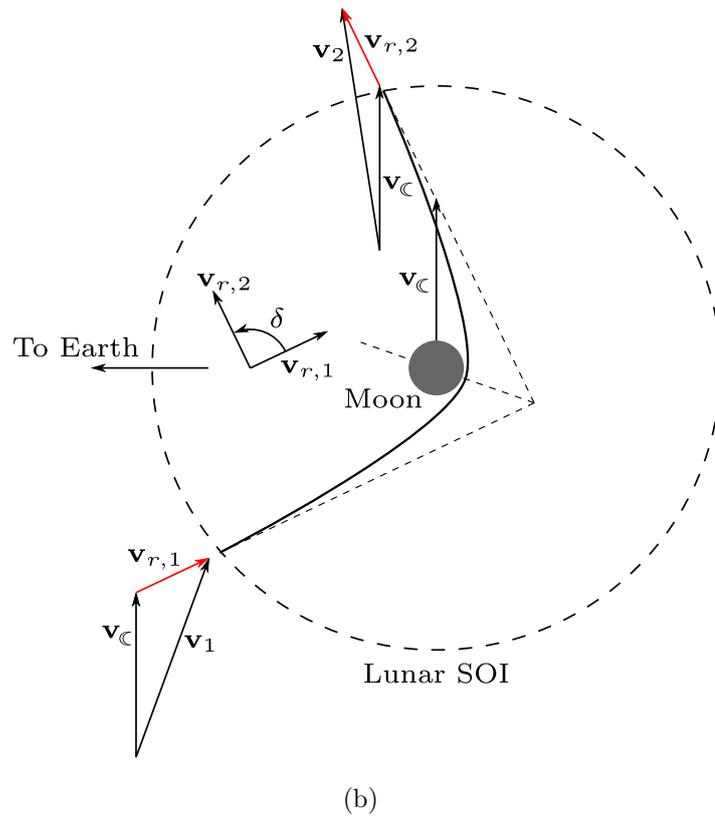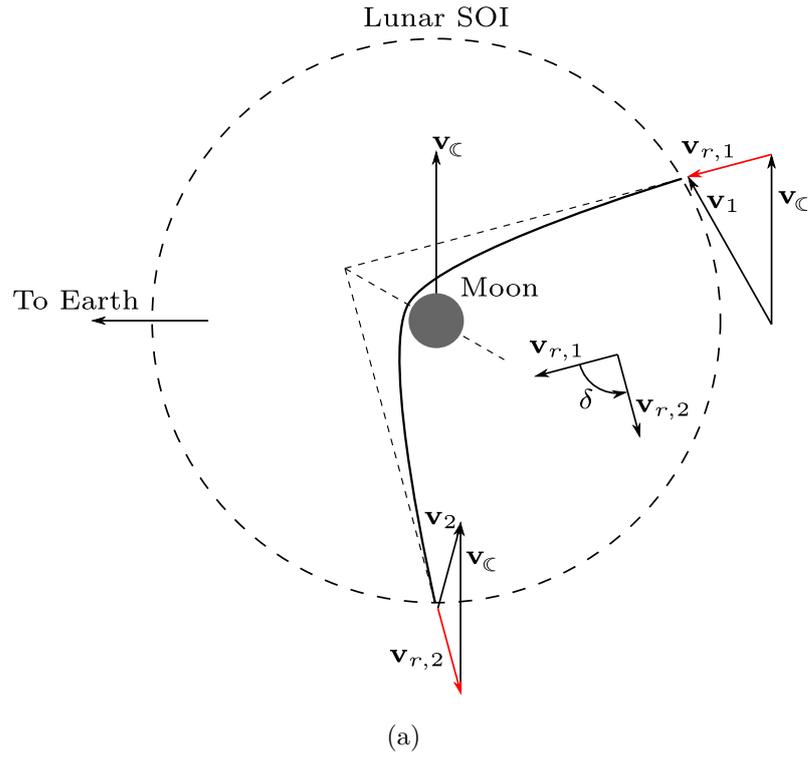
Figure 2.11: Leading-side (a) and trailing-side (b) flyby schematic, analysed in the Moon-centred 2BP.

Mathematically, the rotation is performed by the the multiplication of the velocity vector times the Rotation Matrix ($\mathbf{R}$) which assumes different forms in the case of a clockwise or a counter-clockwise rotation.

$$\mathbf{R}_{CW} = \begin{bmatrix} \cos\delta & \sin\delta \\ -\sin\delta & \cos\delta \end{bmatrix} \qquad \mathbf{R}_{CCW} = \begin{bmatrix} \cos\delta & -\sin\delta \\ \sin\delta & \cos\delta \end{bmatrix}$$

As defined in Figure 2.11, δ is the angle between the pre- and post-flyby relative velocity vector and is known as the Bending Angle (δ). This angle is a function of the altitude of the flyby h, in fact, the closer the flyby the higher is the influence of the Moon on the trajectory; and thus, larger rotations can be achieved.

$$\delta = 2\,\mathrm{asin}\,\frac{1}{e} \tag{2.32}$$

where e is the eccentricity of the Moon centred hyperbola

$$e = 1 + |\mathbf{v}_{r,1}|^2 \frac{R_M + h}{\mu_\mathrm{C}}$$

with R_M as the radius of the Moon and μ_C as its gravitational parameter. Finally, the post-flyby velocity vector is computed as

$$\mathbf{v}_{r,2} = \mathbf{R}\mathbf{v}_{r,1} \tag{2.33}$$

and is added again to $\mathbf{v}_\mathrm{C}$, note that, since the flyby is assumed to be instantaneous, the velocity vector is assumed to maintain the same direction (the magnitude is constant since its trajectory is assumed to be circular)

$$\mathbf{v}_2 = \mathbf{v}_\mathrm{C} + \mathbf{v}_{r,2} \tag{2.34}$$

This post-flyby condition is then propagated forwards in time to obtain the trajectory after lunar encounter.

STATE OF THE ART

T HIS chapter provides an overview of the existing literature, allowing the reader to get a better understanding of past missions which exploited lunar flybys to achieve their objectives. Furthermore, some of the key questions of this work are addressed focusing only on already existing research, trying to gain some insight of the results that can be expected at the end of this thesis.

Initially non-powered and powered escape trajectories are discussed based on the analysis provided by ESA in their Mission Analysis Guidelines (MAG). This initial analysis completely neglects the availability of the Moon for a gravity assist and is only presented for completeness. Then, gravity assists are introduced presenting a variety of missions which took advantage in different ways of single or multiple lunar flybys. Finally, three different approaches to the design of lunar gravity assist trajectories are presented giving the foundation for the work presented in this thesis.

3.1 NON-POWERED AND POWERED DIRECT ESCAPE

The L_2 Libration Point, as the other collinear equilibrium points is *unstable*, therefore, the simplest way in order to depart towards an escape trajectory is simply following the natural evolution of the dynamics. In fact, given the differences between the numerical model and reality, i.e., presence of external perturbations, errors in the positioning of the satellite, non-zero velocity of the satellite, ecc., the spacecraft

will autonomously depart from L_2 following one of the so called *unstable invariant manifolds* [19, 23]. The preliminary study provided by ESA [8] demonstrates that, while the manifold leading away from the Earth results in a direct escape trajectory with an heliocentric velocity of 500 m/s with respect to the Earth, the departure towards the terrestrial realm leads to a close encounter with the Earth and possibly with the Moon before leaving towards interplanetary space.

Due to the asymptotic behaviour of non-powered escape [19, Ch. 7.2], a powered escape is preferred as it reduces the time of flight of the satellite and introduces some manoeuvrability at departure. The analysis of the powered escape is performed by scanning Δv values between $0 - 2$ km/s and evaluating the behaviour of the trajectory for different impulse directions (always departing from L_2). As a figure of merit for this analysis, different quantities are evaluated when the spacecraft reaches 0.02 AU from the Earth. In particular, regarding the escape velocity, the ratio $v_\infty/\Delta v$ is very interesting as it highlights that efficient transfers ($v_\infty/\Delta v \gg 1$) are available only for low intensity manoeuvres, see Figure 3.1, in fact, in the leftmost region an efficiency close to five can be expected.
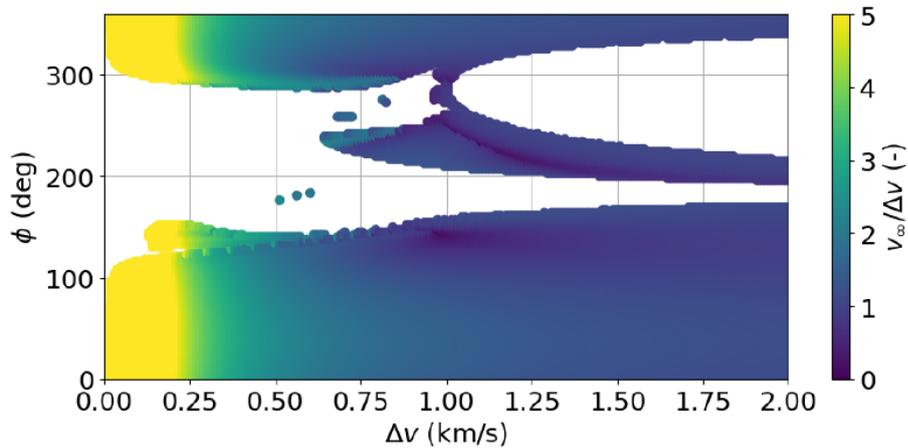
(a) Escape towards $R_c > 1$ AU
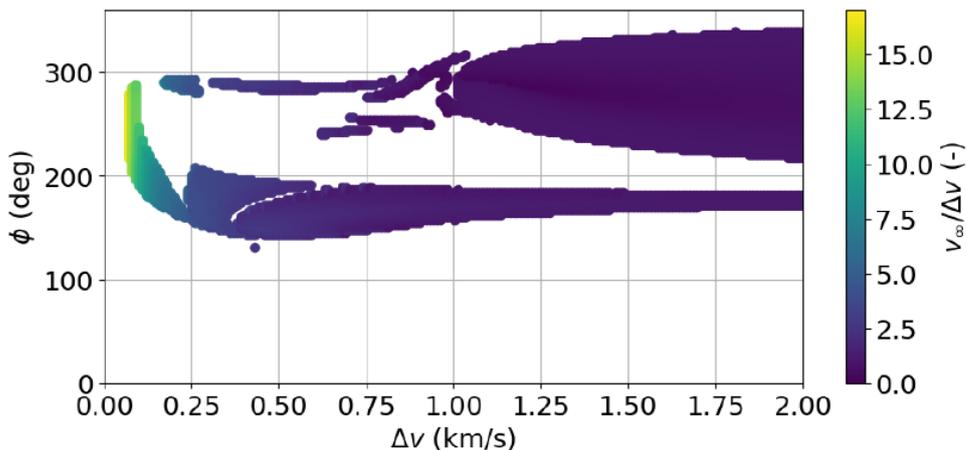
(b) Escape towards $R_c < 1$ AU

Figure 3.1: Example of a Figure of Merit for the powered escape from L_2. Φ indicates the angle between the impulse direction and the Sun-Earth direction [8].

It is important to note that this type of transfer does not inherently exploit the dynamics of the CR3BP.

Furthermore, as CI will be placed around L_2 (located behind the Earth when looking from the Sun), it is understandable that the dynamics of the system favours departure trajectories towards $R_c > 1$ AU. This becomes clear when looking at Figure 3.1 where the majority of conditions depart towards $R_c > 1$. Similar results can be found in the literature [9] where, with the same Δv budgets, greater heliocentric distances are achieved when departing towards the exterior realm.

Moreover, the fact that, in reality, the spacecraft is in an orbit around L_2 and not placed at L_2 is completely neglected. The analysis of this particularity is introduced in the CReMA [38]. In order to determine the influence this has on the originally computed cost, two example transfers to comets 73P and 26P (two backup targets for the mission) are computed starting from L_2; the same trajectories are then computed starting on different points of a quasi-Halo orbit and the reduction or penalty of Δv is computed. From this analysis it appears clear that, while some sections of the quasi-Halo orbit favour the departure with reductions between 100 and 400 m/s,

some others have negative impact on the propulsive budget with penalties of 200-300 m/s.

3.2 EXPLOITATION OF LUNAR FLYBYS

While the discussion above gives some insight in the problem at hand, limitations are rapidly reached as relatively high values of v_∞ can be reached only through an intense departure burn from the desired parking orbit. Not only could the selected propulsive system not be capable of such high impulsive manoeuvres (above 0.5 km/s), but, the total propulsive budget for the mission would be greatly compromised for the departure, leaving less space for following navigation and/or correction manoeuvres.

To overcome this issue, many researches in the field of astrodynamics have analysed the possibility of an Earth escape trajectory that exploits the Moon through a lunar gravity assists[18, 39–42]. This type of strategy has been exploited the first time for the extension of the ISEE-3 of ICE mission. In this case the spacecraft was initially placed in an orbit around L_1 from where it departed towards the L_2 in order to, initially, analyse the Earth's geomagnetic tail, and finally, intercept the comet Giacobini-Zinner in 1985 . In particular, the Moon encounters were programmed in order to adjust the timing with the comet and to achieve the required escape velocity of ≈ 1.57 km/s [43].

The design of a variety of missions over the last decades is based on the correct exploitation of the Moon. While, in some cases, the mission was impossible to accomplish without the gravity assist, see STEREO mission, in some others it decreased the Δv budget for the transfer reducing the costs or increasing the life of the mission as more propellant was available for eventual correction manoeuvres or required station keeping manoeuvres.

In the work of Wilson and Howell [42], two different applications of lunar gravity assists are presented, in the first case, Figure 3.2a, a sequence of lunar flybys are scheduled in order to change the apogee direction of the final orbit (from the antisolar to the solar direction) while in the second case, Figure 3.2b, a single flyby is used to insert the spacecraft into a transfer trajectory leading to the L_2 Libration point.

(a)

(b)
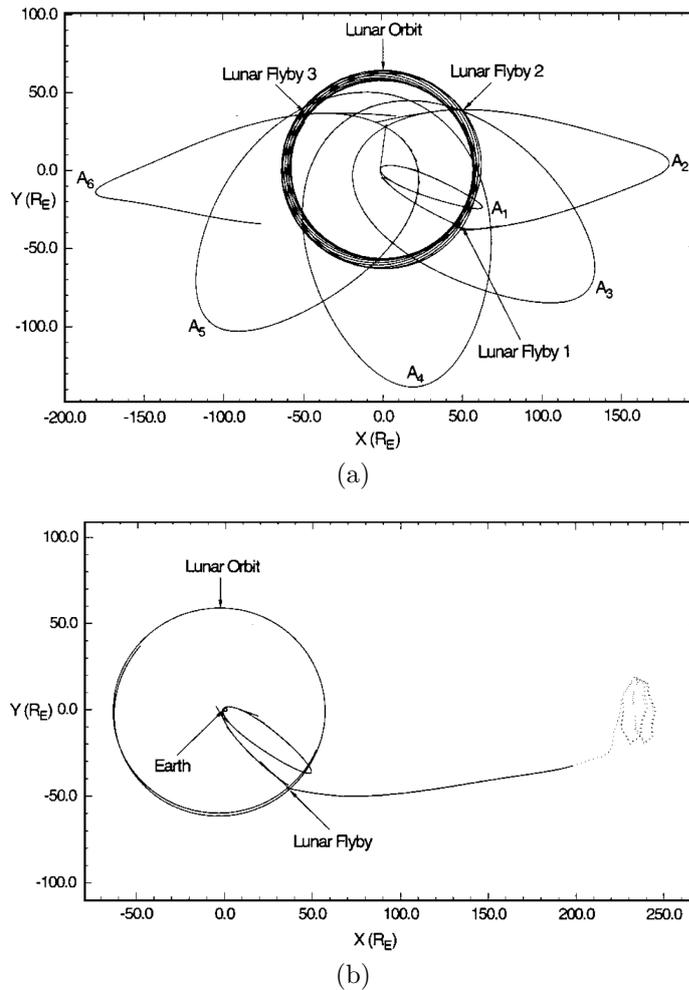
Figure 3.2: Example trajectories where lunar flybys are exploited in order to change the final orientation/type of the orbit [42].

This second example is quite explicative of what can be obtained via a lunar flyby, as an example, for the EQUULEUS mission, it was possible to design a low-cost transfer trajectory to an Earth-Moon L_2 Halo orbit. In fact, after separation, the spacecraft is inserted in its final science orbit using only 10.2 m/s of its total 77 m/s Δv budget.

For LUNAR-A a single lunar flyby was used in order to transfer the spacecraft from its Earth centred parking orbit to its final orbit around the Moon. The objective of the flyby was to increase the size of the initial transfer orbit in order to better exploit the Sun's gravitational field leading to a ballistic capture by the Moon and reducing the Δv budget of the transfer by 176 and 152 m/s with respect to a Hohmann or a bi-elliptic transfer, respectively [18].
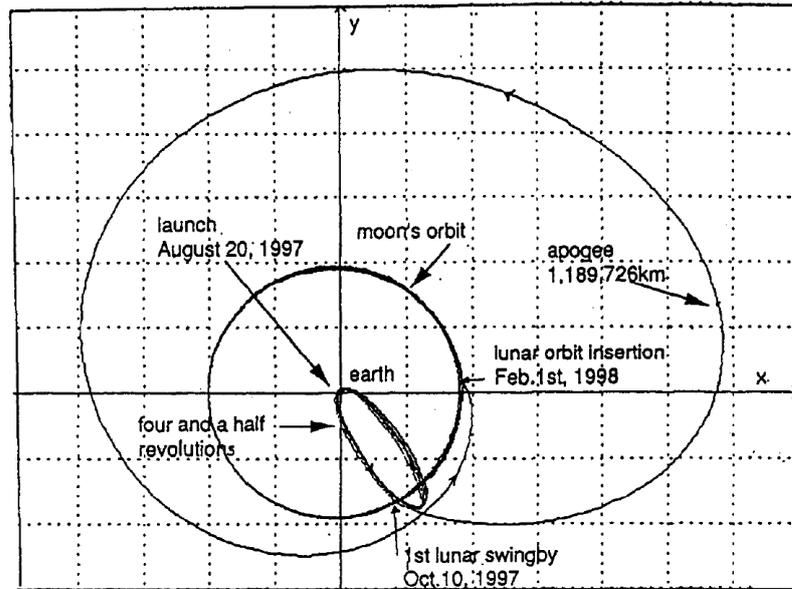
Figure 3.3: Trajectory of the LUNAR-A mission in the Earth centred inertial reference frame Kawaguchi et al. [18].

The concept of programming a lunar flyby to increase the size of the orbit to better exploit the Sun's perturbation, is widely discussed in the literature [17, 20, 44, 45] and naturally considered in the work hereafter by analysing the trajectory in the CR3BP.

As the objective of numerous missions is the exploration of interplanetary space, various examples of missions can be found when looking for lunar flybys devoted to put the spacecraft onto an escaping trajectory. The DESTINY+ mission [45, 46] is a noticeable example, its trajectory is designed to intercept the Moon once before leaving the Earth-Moon region on its way to (3200) Phaethon. Figure 3.4 shows

some example trajectories which achieve the required $v_\infty = 1.5$ km/s in the correct direction with lunar flyby altitudes above 200 km.
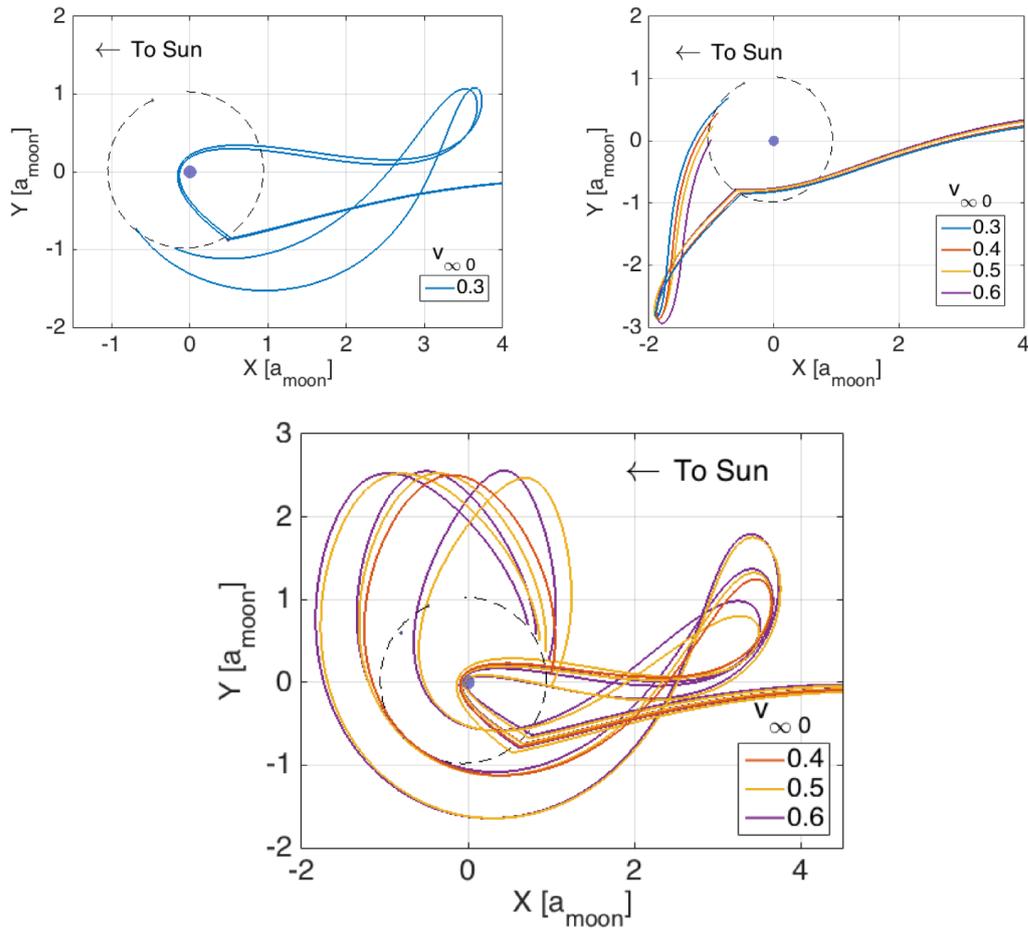
Figure 3.4: Example escape trajectories for JAXA's DESTINY+ mission directed towards (3200) Phaethon [45].

For NASA's STEREO mission the use of lunar gravity assists was fundamental. The objective of the mission was a stereoscopic observation of the Sun, to achieve this goal two spacecraft (STEREO A and B) were positioned Ahead and Behind the Earth in its orbit. Since both spacecraft were launched together, the final orbits were only possible by designing different lunar flyby sequences. In fact, while STEREO A performed a single flyby, STEREO B performed two of them and with different characteristics in order to enter a completely different departure trajectory [47].
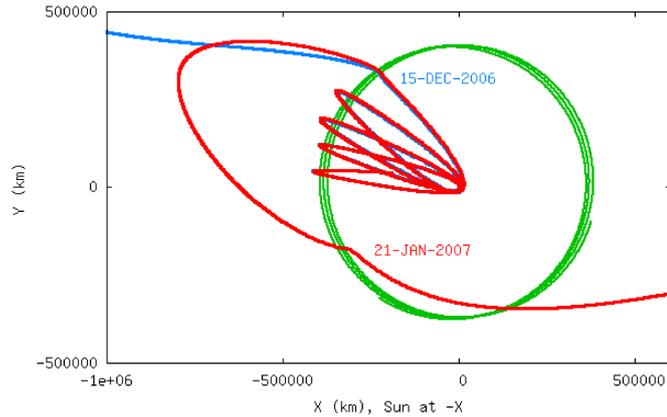
Figure 3.5: Trajectories of NASA's STEREO A (in blue) and B (in red) spacecrafts. Mcelrath et al. [48].

Furthermore, for STEREO B, an additional lunar swing-by could be implemented as an insertion manoeuvre into a L_2 Halo orbit [49].

In the case of ESA's BepiColombo mission, an initial lunar flyby is exploited in order to send the spacecraft into its heliocentric orbit. The analysis is presented by Campagnola, Jehn, and Van Damme [50] showing that escape velocities (V_{SOL} in the paper) between 1.1 and 1.75 km/s are achievable.

While the presented problem is different (departure from a Halo-orbit instead of Earth departure), similar results are presented by Chen, Kawakatsu, and Hanada [44] and Yárnoz et al. [45], where escape velocities as high as 1.87 km/s are obtained when considering a sequence of two flybys and around 2.1 km/s with a triple-flyby strategy s for the PLANET-B mission [18]. The introduction of additional flybys allows for a better 'tuning' of the final encounter while already increasing the energy with respect to the initial value. Obviously, this type of strategies lead to an extended flight time.

3.3   DIFFERENT APPROACHES TO THE DESIGN

Looking at the scientific literature, the problem was tackled in different ways, but mainly three approaches can be found. The first approach is based on the initial approximation of the trajectory as a sequence of Moon-to-Moon conic arcs [42]. This first approximation is then improved by using a *multiconic approach* in order to incorporate neglected force models. This is done by evaluating each gravitational contribution, i. e., Sun, Earth and Moon, separately as 2BP which are then 'overlapped' [51, 52]. Finally, the trajectory is optimized by reducing the velocity discontinuities at the patching points.
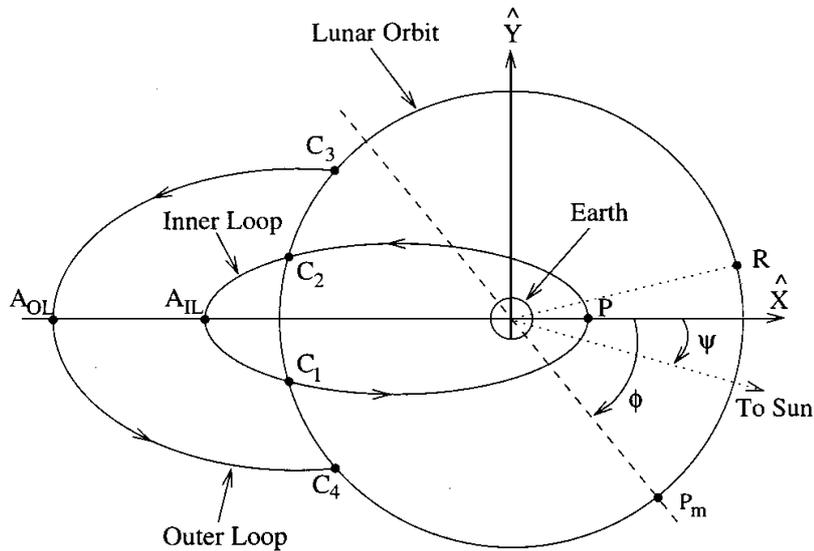
Figure 3.6: Definition of conic arcs used as initial approximation by Wilson and Howell [42].

In the second approach the trajectory is propagated under the influence of the Earth's and the Sun's gravities, while the Moon is considered only at encounter through an instantaneous rotation of the relative velocity vector [44, 45]. Multiple

lunar gravity assists are analysed by building families of Moon-to-Moon trajectories, Figure 3.7, solving the timing condition for a variety of post flyby conditions,

$$\{(\alpha, ToF) \,|\, \Delta\theta = 0 \wedge \Delta d = 0\} \tag{3.1}$$

where α is the angle between $\boldsymbol{v}_{\infty,M}^{+}$ and the Earth-Moon direction, ToF is the time of flight of the Moon-to-Moon segment, $\Delta\theta$ is the phase difference to the lunar phase and Δd is the distance difference to the lunar position. As the lunar gravity is considered only at encounters, the generated families are completely independent of the Moon's position in its orbit. Different flyby sequences are generated by patching together sequences of Moon-to-Moon transfers until the desired final condition is met.
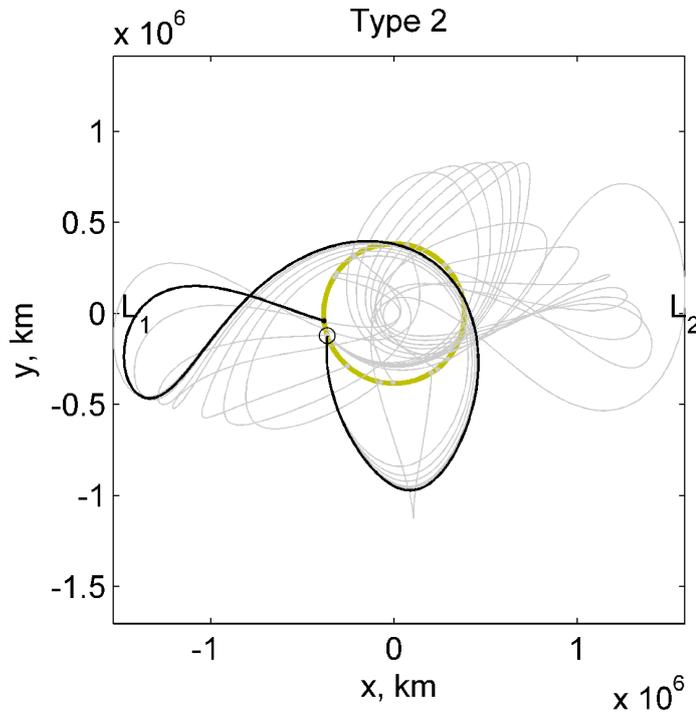
Figure 3.7: Example of a family of Moon-to-Moon transfers with two Sun-perturbed loops [44].

The third approach is the one introduced by Qi and Xu [21], while in the previous approaches the Moon's gravity is considered only at encounter to 'patch' together two subsequent legs, here the full four-body problem is divided into two CR3BP. In fact, it

is shown that, while being close to the Earth-Moon system, the influence of the Sun can be neglected leading to a simpler analysis of the problem. Similarly, the Earth-Moon system can be 'condensed' to a single body when the spacecraft is at a great distance. While in the presented paper the objective was different than the one of the present work, its approach is still useful when a more accurate description of the full trajectory is desired. In fact, as discussed by Prado [53], while in the majority of the cases the patched problem well approximates the more accurate three-body problem for the swing-by, in some particular cases, i.e., low energy orbits, this accuracy is not guarantee.

ANALYSIS OF THE DIRECT ESCAPE TRAJECTORY

T O start the analysis of the problem, it is fundamental to understand the set of initial conditions that can be expected. These conditions can be determined once the final parking orbit and its characteristics are known. The identification process of a suitable parking orbit is described in the first part of this chapter. After setting the general initial conditions of the spacecraft, it is necessary to estimate the required base values for the escape velocity and for the *tof* of 'traditional' departure trajectories. These values can then be utilized to evaluate the advantages of alternative trajectories which enter the cislunar space to target and exploit a lunar flyby.

As the traditional definition of v_∞ is based on the energy conservation in the 2BP, the first part of this chapter will be devoted to the definition of the escape velocity in the PCR3BP and to the discussion of its validity. Only after this point is discussed, giving a figure of merit for the different trajectories, it is possible to analyse possible departure strategies studying their individual advantages.

4.1   COMET INTERCEPTOR PARKING ORBIT

Comet Interceptor, after separating from ARIEL M4, will be placed in a quasi-halo orbit around the Sun-Earth/Moon L_2 point. As discussed in the MAG, indicative values for the orbit sizes, shown in Table 4.1, can be obtained looking at the ARIEL 2026 launch window [8].

Maximum distance from Earth, x_{max}	1770700 km
Maximum A_y amplitude	871000 km
Maximum A_z amplitude	611000 km
Declination	43.1 deg

Table 4.1: Extremes of a quasi-Halo orbit for the 2026 launch window [8].

The numerical propagation of a suitable transfer from the Earth to such an orbit is presented in Figure 4.1.
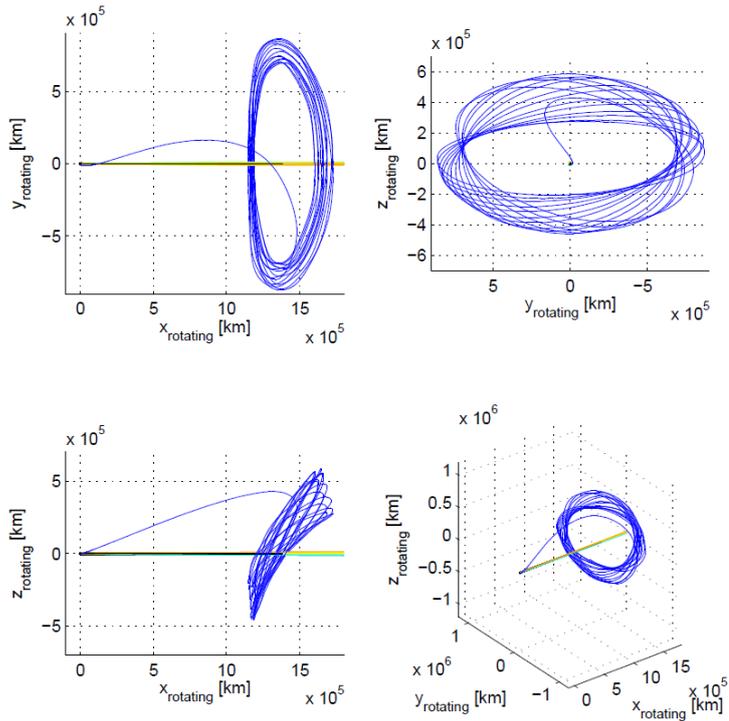
Figure 4.1: Sample of transfer to the quasi-halo orbit around the Sun-Earth L_2 point [8].

As expected, final orbit is in three dimensional space, but, as the scope of this thesis is only a preliminary study of the departure phase, the problem is approximated with its two dimensional counterpart. In particular, instead of the quasi-Halo orbit, a Planar Lyapunov orbit is considered.

The desired Lyapunov orbit is generated starting from a database of already computed orbits provided by Professor Sánchez. In it, a list of energy levels is associated to the state of the initial point of the orbit ($\mathbf{x}_{po,0}$), identified by the furthest point on the x-axis. As, by definition, the orbit is symmetric about the horizontal axis, the initial state takes the form

$$\mathbf{x}_{po,0} = \begin{bmatrix} x_{po,0} \\ 0 \\ 0 \\ \dot{y}_{po,0} \end{bmatrix}$$

To maintain a close relationship with the original problem, it is necessary to compute an orbit with a similar Jacobi constant. For an orbit around L_2, C can be written as a function of C_{L_2} and C_{L_3} (Jacobi constants for the L_2 and L_3 Lagrangian points) as these can be considered as extremes of its interval.

$$C \in (C_{L_3}, C_{L_2}) \qquad C = C_{L_3} + \frac{C_{L_2} - C_{L_3}}{k} \tag{4.1}$$

where $k = k_{po}$ determines the size of the selected orbit and its Jacobi Constant, C_{po}. The suitable value for the k_{po} coefficient is found via a bisection method which 'compares' the obtained size to the limits given in Table 4.1. This numerical procedure is necessary as in the literature it was impossible to find an analytical relationship which correlates the maximum dimensions of the desired orbit and its Jacobi Integral. Furthermore, as the provided database collects only discrete values for C, *numerical continuation* and *differential correction* [19, 37] need to be applied to compute the initial state for the desired C_{po}. After selecting the initial coefficient interval as $k \in [k_L, k_U] = [1, 10]$ the iterative procedure is as follows:

1. C^i is computed via Eq. 4.1 where $k^i = k_L + k_U/2$;

2. the closest value of C in the database is identified;

3. continuation and differential correction are applied to find the initial condition which exactly matches C^i;

4. the full Lyapunov orbit is propagated evaluating x_{max} and A_y

5. if the limits, i.e., x_{max} and A_y are respected then $k_L = k^i$ otherwise $k_U = k^i$

the bisection method is stopped when $\left| k^i - k^{i-1} \right| \leq 10^{-5}$.

In Figure 4.2 the final orbit is shown together with the representation of the forbidden region for its specific energy level. Furthermore, the characteristics of the obtained Parking/Periodic Orbit (PO) are listed in Table 4.2, these will be used throughout the work in order to uniquely identify the initial conditions of the spacecraft before departure.
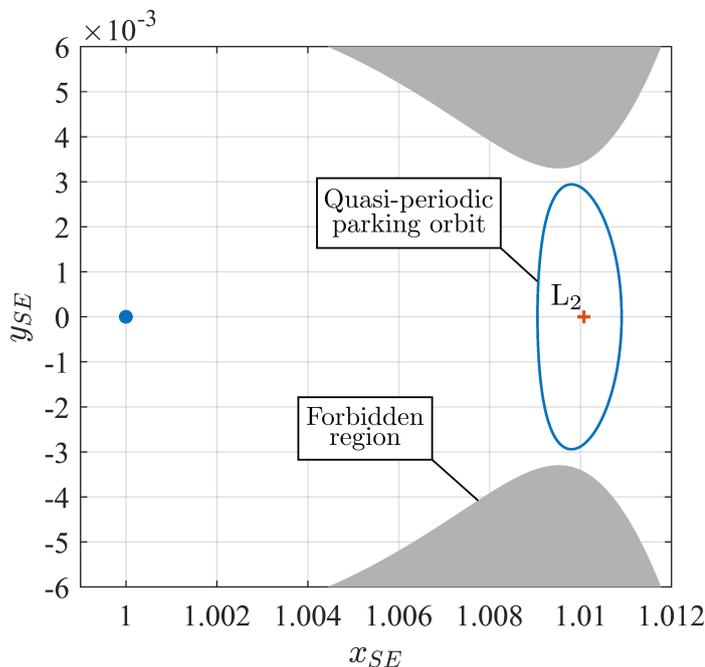
Figure 4.2: Planar Lyapunov orbit obtained after the bisection method.

C_{po}	3.000867937
Initial State, $\mathbf{x}_{po,0}$	$\begin{bmatrix} 1.0109 & 0 & 0 & -0.0059 \end{bmatrix}^T$
Orbital Period, T_{po}	3.0741 (178.6 days)
x_{max}	$1\,629\,502$ km
A_y	$864\,234$ km

Table 4.2: Characteristics of the Planar-Lyapunov orbit used for the continuation of this work.

4.2 THE HELIOCENTRIC ESCAPE VELOCITY

In the 2BP the escape velocity, also known as *hyperbolic excess speed*, is the velocity of a spacecraft when it reaches virtually infinite distance from the main attractor following an hyperbolic trajectory. Thus, by considering the energy conservation law, described mathematically in Eq. 4.2, it is possible to obtain a first definition of the escape velocity [16, Ch. 2.9].

$$\frac{V^2}{2} - \frac{\mu_{2B}}{r} = \frac{V_\infty^2}{2} \tag{4.2}$$

Note that here μ_{2B} refers to the gravitational parameter of a particular celestial body in the two body problem. Nevertheless, this definition is based on the assumption that the given trajectory is hyperbolic, making it unsuitable for the problem at hand as the spacecraft is placed in a quasi-periodic orbit around L_2 and not on an hyperbolic arc with respect to the Earth. Consequently, an alternative description needs to be implemented taking into account the 'three-body nature' of the problem.

As discussed by Perry [54], v_∞ can be considered as the 'additional velocity' required to reach a specific *semi-major axis* launching the spacecraft from the Earth instead of departing from the quasi-periodic orbit around L_2. Mathematically, this is expressed as

$$\frac{V^2}{2} - \frac{\mu_\odot}{r_E} = -\frac{\mu_\odot}{2a} \tag{4.3}$$

where $\mu_\odot$ is the gravitational parameter of the Sun, r_E is the radius of the Earth's orbit ($r_E = 1$ AU), a is the semi-major axis of the orbit reached after the departure from L$_2$ and V is the velocity required to satisfy the energy law and can be expressed as the sum between the Earth's orbital velocity ($V_E = \sqrt{\mu_\odot/r_E}$, for a circular orbit) and v_∞. Thus, from Eq. 4.3 and the definition of V_E, the following equation for v_∞ is obtained.

$$v_\infty = \sqrt{2\left(\frac{\mu_\odot}{r_E} - \frac{\mu_\odot}{2a}\right)} - \sqrt{\frac{\mu_\odot}{r_E}} \tag{4.4}$$

Note that all the quantities are dimensional and defined in the Sun-centred *inertial* reference frame.

As opposed to the previous case, here the escape velocity definition is based on the assumption that the spacecraft is on a heliocentric trajectory and not on an Earth centred hyperbola. In fact, while initially the force exerted on the spacecraft by the Earth is comparable to the one exerted by the Sun, the latter gradually prevails as the spacecraft moves further away from the Earth. This leads to the observation of two separate regions:

1. one region close to Earth, where the two gravitational forces are comparable, and where the use of the 3BP is necessary, undermining the validity of Eq. 4.4;

2. the second region far from Earth, where the spacecraft is mainly influenced by the Sun's gravitational field, and where the 2BP well approximates the motion.

In order to evaluate at which distance from the Earth the spacecraft can be considered in a purely heliocentric trajectory, the osculating conic orbit is evaluated at each point of the integrated trajectory computing its keplerian elements. Observing the evolution of the specific elements it is possible to evaluate the accuracy of the 2BP approximation, in particular, in Figure 4.3 the osculating semi-major axis, a, is plotted over the nondimensional distance from Earth. This element is chosen as it is the one of main interest looking at the definition of v_∞ in Eq. 4.4.
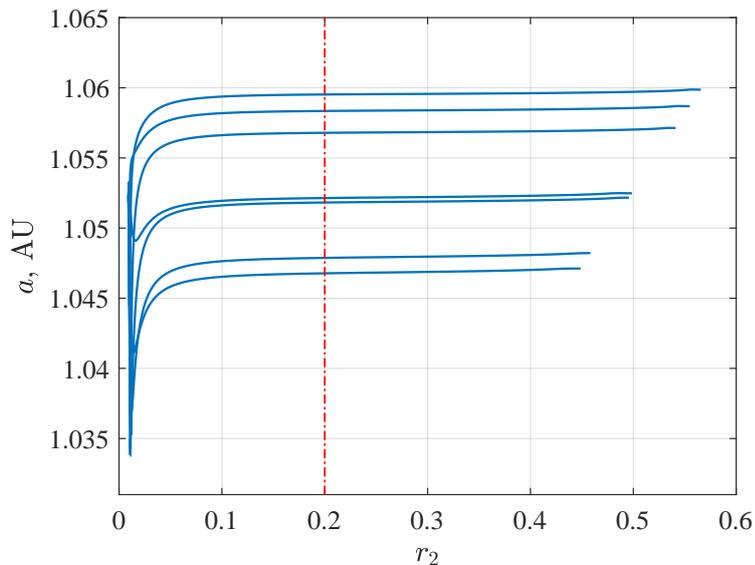
Figure 4.3: Convergence of the osculating semi-major axis over the nondimensional distance from Earth.

As expected, close to the Earth the 2BP is a bad approximation of the propagated trajectory, leading to high variations of a for r_2 close to zero. Although, already after $r_2 = 0.1$ the convergence of a is apparent, for the continuation of this work, the trajectory is propagated until reaching $r_2^* = 0.2$ before computing v_∞. This distance is deemed as sufficient for obtaining good results from the computation of v_∞ , as it lies in between what is used in his work by Perry [54], where the trajectory is propagated until it reaches an angle of $\pm\pi/8$ with respect to x_{SE} corresponding to a distance of ≈ 0.38 and 0.02 which is used as control radius in the CReMA [38]. Furthermore, the selection of r_2^* is not only based on the required precision on the escape velocity, but also on the trade of with respect to the integration time necessary to propagate the trajectory at a greater distance.

4.3 DIRECT ESCAPE VELOCITY AND TIME OF FLIGHT

After giving the definition of the escape velocity, it is now possible to obtain first results which will serve as a baseline for what can be expected from an L_2 departure.

To do so, as described in detail in Chapter 2, a series of departure conditions are generated on the unstable manifolds going towards the exterior realm, targeting $R_c > 1$ AU, or towards the interior realm, targeting $R_c < 1$ AU.

Typically, the initial state of the invariant manifold is obtained by adding a small perturbation to an initial state on the LPO as described in Eq. 4.5. The 'direction' of the perturbation, i. e., $Y^u(X_0)$, is selected from the eigenvectors of the monodromy matrix and represents the unstable direction, for a detailed explanation see Koon et al. [19, Ch. 7.2].

$$X^u(X_0) = X_0 + \epsilon Y^u(X_0) \tag{4.5}$$

X^u is the initial state on the invariant manifold, X_0 is the 'departure' state on the LPO and ϵ is the magnitude of the perturbation ($Y^u(X_0)$ is normalized). The value of ϵ should be small enough to maintain the validity of the linear approximation [19, Ch. 4.3], but not too small as otherwise the time of flight tends to infinity, suitable values are around 10^{-6} which leads to position displacements of ≈ 200 km and velocity changes of ≈ 0.07 m/s as suggested by Gómez et al. [55].

Although the above described procedure is widely accepted, for the continuation of this work Eq. 4.5 is slightly modified introducing ϵ_p and ϵ_v as follows

$$X^u(X_0) = X_0 + \epsilon_p \begin{bmatrix} Y_1^u \\ Y_2^u \\ 0 \\ 0 \end{bmatrix} + \epsilon_v \begin{bmatrix} 0 \\ 0 \\ Y_3^u \\ Y_4^u \end{bmatrix} \tag{4.6}$$

where

$$\epsilon_p = \frac{\delta P}{L_{SE}} \quad \text{and} \quad \epsilon_v = \frac{\delta V t_{SE}}{L_{SE}},$$

This form gives a more physical description of the perturbation as δP and δV are actually the position displacement and the velocity impulse, in km and km/s respectively, needed to depart in the desired trajectory. Clearly, the variation in position

(a) Departure towards $R_C < 1$ AU.

(b) Departure towards $R_C > 1$ AU.
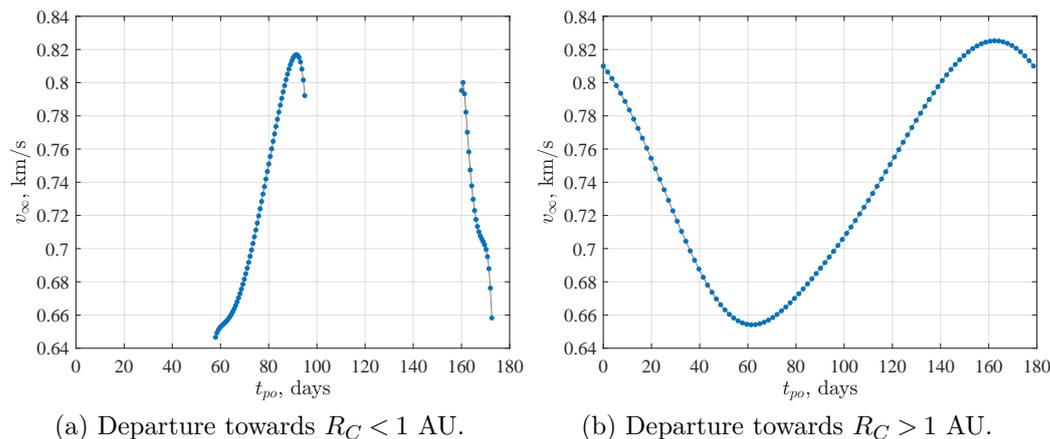
Figure 4.4: Escape velocity for direct departure trajectories.

cannot be achieved instantaneously, the obtained position is intended as a target which is reached with an appropriate station-keeping strategy.

While for the analysis of the cislunar trajectory δP and δV are considered to be variable between $0 - 200$ km and $0 - 10$ m/s, here the perturbation applied to the L_2 LPO is 200 km in position and 10 m/s in velocity, as it is maximum manoeuvrability of the spacecraft when departing from its parking orbit and results in the minimum time of flight, as smaller perturbations lead to asymptotic behaviour Koon et al. [19, Ch. 7.2].

The so obtained initial conditions are then propagated until r_2^* is reached; trajectories with $tof > 2$ years are neglected as they are not of interest for this analysis. The obtained departure trajectories are virtually at *zero-cost*, as they exploit the natural dynamics of the system through a negligible manoeuvre. The results are reported in Figures 4.4 and 4.5 plotting respectively v_∞ and the *tof* versus the departure position in the quasi-periodic orbit defined by t_{po}, as described in Section 4.1.

It is clear that, even in the case of a direct departure, an optimisation process is possible. In fact, v_∞ and *tof* vary over one period of the parking orbit; assuming that the available time is sufficient, 0.82 km/s is considered as the optimistic baseline for the available escape velocity through a direct escape for the continuation of this

work for both departure directions. These values are in line with what is obtained by Perry [54] and Matsumoto and Kawaguchi [56] and with what is used as a preliminary value for the analysis performed by Sánchez [9]. It is worth noting that the obtained results are almost double of what can be found in the CReMA [38] as there various simplifications are considered. Specifically, the two body problem theory is applied to the spacecraft placed at L_2 considering it to be in a circular orbit around the Sun with the same orbital period as the Earth but at a greater distance, for departure towards the exterior realm. This leads to a difference between the actual velocity of the spacecraft and the theoretical velocity for the circular trajectory

$$v_\infty = v_{L_2} - v_{circ} = \sqrt{\frac{\mu_\odot}{r_E^3}(1 + \mu_{SE})r_E} - \sqrt{\frac{\mu_\odot}{r_E(1 + \mu_{SE})}} \approx 0.5 \text{ km/s}$$

The escape velocity is not the only variable of interest, in fact, as there is only a limited time budget between the observation of a DNC and its interception, the analysis of the *tof* is equally important.

(a) Departure towards $R_C < 1$ AU.   (b) Departure towards $R_C > 1$ AU.
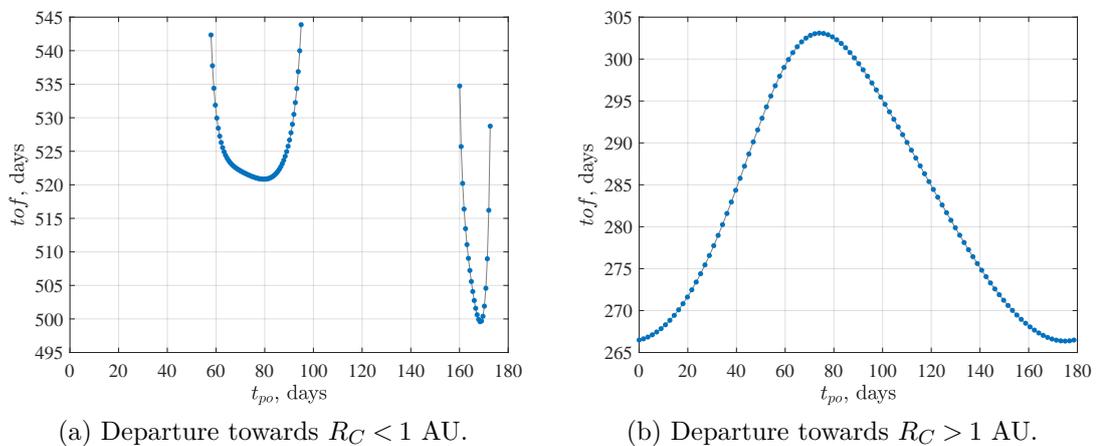
Figure 4.5: *tof* for direct departure trajectories.

While, in terms of v_∞ there is not a substantial difference between departing towards R_c greater or smaller than 1 AU, this is not true for the time of flight. In fact, when departing towards $R_c > 1$ the time of flight is between 265 and 305 days, but, increases drastically to values above 500 days when departing towards $R_c < 1$

AU. Whilst flight times of less than one year are acceptable for the departure phase as a sufficient budget is left for the rest of the trajectory, values above 500 are not reasonable if not supported by a substantial advantage of v_∞ which would facilitate the design of the interplanetary trajectory.

As the spacecraft is placed around L$_2$, the departure towards the exterior realm, and thus towards $R_c > 1$ AU is advantaged with respect to a departure towards the Earth. This translates in a more regular behaviour of the departure trajectory, and consequently, of the values in Figures 4.4b and 4.5b with respect to the ones in Figures 4.4a and 4.5a. This is due to the fact that, when targeting $R_c < 1$ AU, the spacecraft passes close to the Earth, influencing the 'available' trajectories in different ways:

1. the perigee is limited above an altitude of $36\,000$ km, equivalent to geostationary orbit, this lower boundary is selected as it facilitates the *collision avoidance* analysis during future studies;

2. as the spacecraft enters deeper in the Earth's gravitational well, the spacecraft performs multiple revolutions around the Earth before eventually escaping (see Figure 4.6), this leads to a drastic increase in flight time , and in extreme cases, $tof > 2$ years, to the exclusion of such transfers.

Therefore, considering for simplicity a constant departure manoeuvre of 10 m/s, escape trajectories are not granted for each position on the quasi-periodic orbit, further increasing the difficulty of the design of a suitable escape towards $R_c < 1$ AU. In Figure 4.6 the two types of escape trajectories are shown in order to give the reader a better understanding of the issues associated with the Earth-bound departure. Especially the inefficiency in terms of tof becomes clear when looking at the orange trajectory.
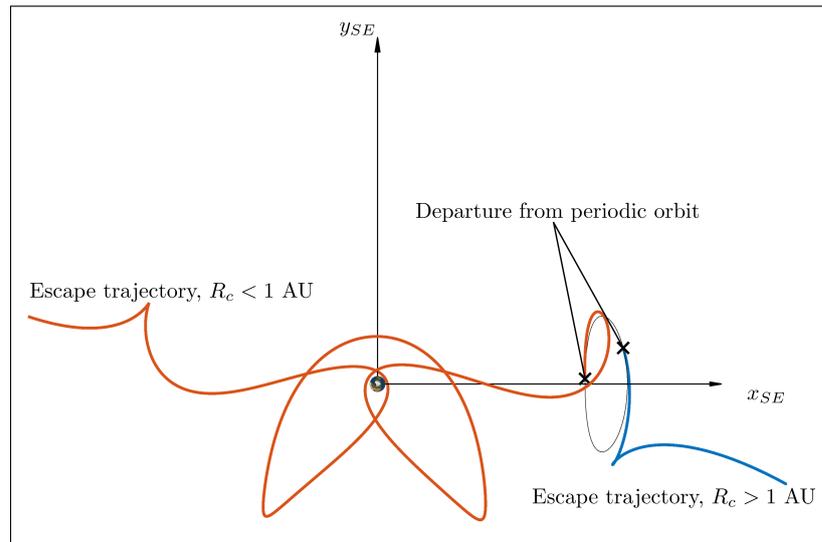
Figure 4.6: Direct escape trajectories with maximum escape velocity.

Looking at these results, it becomes clear that, while the main objective is still the maximization of the escape velocity, particular attention needs to be given to the time of flight as well, limiting the maximum time, i.e., from the first available periodic orbit departure to the time of escape at r_2^*, to 1.5 years, and ideally, under 1 year.

ANALYSIS OF THE SWING-BY TRAJECTORY

IN the previous chapter the direct escape strategy has been discussed, concluding that, even without the influence of the Moon, $v_\infty \neq 0$ can be obtained with a negligible departure manoeuvre. As discussed in Chapter 3, it can be expected that, including a gravity in assist in the design of the escape trajectory, higher escape velocities are achievable for still negligible departure manoeuvres.

In the following chapter the applied methodology is presented in detail, highlighting the reasoning behind the different steps of the design and the hypothesis or simplifications that have been applied.

Initially, the full trajectory is divided into two parts which are then studied separately. The first part is the trajectory leading the spacecraft from its parking orbit to the encounter to the Moon and the second part is the trajectory after the lunar encounter. This procedure is based on the assumption that the Moon's gravity is negligible in this preliminary analysis.

This particular division of the trajectory, suggests the introduction of a new set of variables which are better suited than the normal $[x \quad y \quad \dot{x} \quad \dot{y}]$ state variables, in particular when representing the flyby location and effects. Assuming that in the Sun-Earth PCR3BP the Earth is located at the coordinate of the second primary, it is possible to define the position relative to the Earth of the encounter using *polar coordinates* [21]. Since the radius is fixed, i. e., $\tilde{a}_M$, a single variable is sufficient to

fully describe the position, α is defined positive in counter-clockwise direction starting from the x_{SE}-axis. A second variable is β, it describes the direction of the velocity vector with respect to the tangent of the lunar orbit, it is also known as *flight path angle*. A graphical representation of these variables is presented in Figure 5.1. Finally, the Jacobi constant is selected as the third variable as, together with the position, it describes the magnitude of the velocity vector. The selection of this new system of variables allows the reduction of the dimensionality of the problem, from 4 to 3.
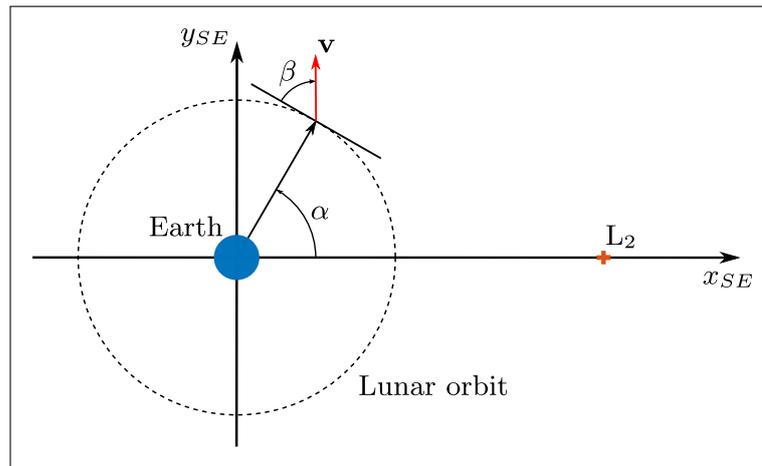
Figure 5.1: Graphical representation of α and β in the Earth-centred synodic reference frame (the Earth is assumed to be at the same position of the EMB).

Furthermore, given the definition of β, i. e., Clockwise (CW) = positive and Counter-Clockwise (CCW) = negative, it is possible to categorize the trajectory at encounter as:

- $\beta < 0$: identifies an *inbound trajectory* , which means that the spacecraft crosses the lunar orbit from the outside to the inside;

- $\beta = 0$: identifies an *outbound trajectory*, which means that the spacecraft crosses the lunar orbit from the inside to the outside.

As the flyby involves a rotation of the velocity vector, see Section 2.4, β can have different sign before and after the flyby, in these cases the representation of the trajectory appears to 'bounce' against the lunar orbit.

5.1 UNSTABLE INVARIANT MANIFOLDS

For the discussion about the advantages of the direct escape the analysis focused on both unstable manifolds associated to the L_2 Lyapunov orbit, one leading towards Earth and one leading away from it. Clearly, now the spacecraft needs to be directed towards Earth as the objective is to intercept the Moon.

As mentioned before, the the departure condition is considered to be variable and is defined as in Eq. 4.6. This variability is introduced as it allows to better target a specific encounter. To analyse how a change in position or velocity affects the encounter conditions, a series of initial states on the periodic orbit are propagate with different levels of perturbation until the trajectory reaches the lunar orbit. At this point α and β are evaluated for each theoretical encounter. As the perturbation in position and velocity are independent, their effects are also studied independently by changing only a single term (δP or δV) at a time.
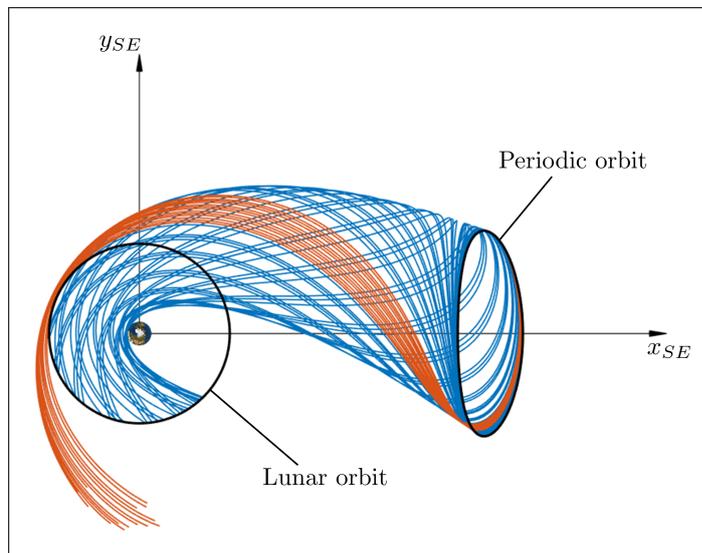

Figure 5.2: Example of departure manifolds for $\delta P = 0$ km and $\delta V = 1$ m/s.

From this study it emerges that the variability due to changes in position is negligible, in fact, from Figure 5.3a the different curves are almost indistinguishable. On the other hand, already slight changes in the departure manoeuvre allow for a wide

range of encounter locations when departing from the same initial position on the parking orbit. However, it can be observed that all the crossings appear to be in similar regions of the lunar orbit, specifically, for the inbound crossing, α_{in} is bound between 15 and 160°, limiting the available configurations for the flyby. Furthermore, from Figure 5.3b, it appears that the 'manoeuvrability' is not the same when departing from different points on the PO, for example, when departing at $t_{po} = 60$ days the range reduces to $15 - 30°$ as opposed to $15 - 130°$ when departing at $t_{po} \approx 95$ days. While here only the Inbound Crossing (IC) is shown, a similar behaviour is observed also for the Outbound Crossing (OC).
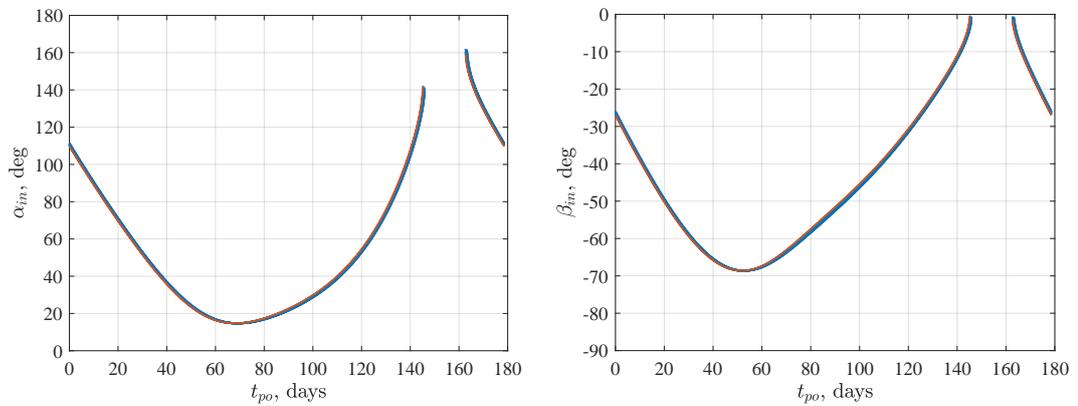
(a) Variability of the encounter as function of δP. The curve in orange indicates $\delta P = 0$ km, then steps of 10 km are considered.
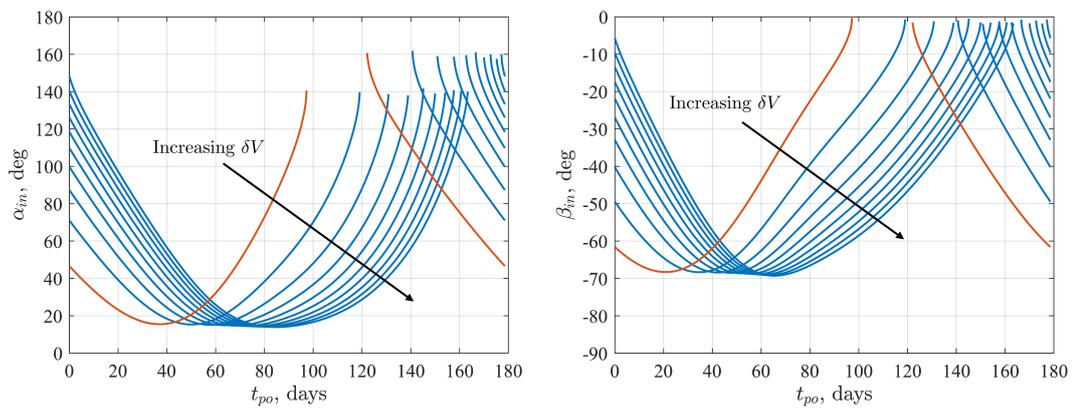
(b) Variability of the encounter as function of δV. The curve in orange indicates $\delta V = 1$ m/s, then steps of 1 m/s are considered.

Figure 5.3: Variability of the encounter conditions α_{in} and β_{in}.

However, for some departure intervals, the propagated trajectories do not intercept the Moon during the allotted amount of time (9 months). As can be seen in Figure 5.2, the trajectories in orange pass outside of the lunar orbit resulting in the discontinuities in Figure 5.3. An analogous behaviour is observed by Qi and Xu [21] for the stable invariant manifolds; he has observed that after a certain value of C, the critical value changes with the size of the considered *Poincaré section*, some of the crossing points are located in a chaotic region which arises from the complexity of the PCR3BP. As a result, these possible encounters are not considered during the rest of the analysis.

As discussed, the third variable, besides α and β, necessary to fully describe the pre-flyby condition is the Jacobi Integral. As the departure perturbation, in position and in velocity, are both negligible in intensity, all manifolds can be considered to have the same energy as the the PO, precisely $C = C_{po} \pm 10^{-6}$.

The main point that needs to be highlighted at the end of this analysis is that, although the manifolds cross the lunar orbit in a bounded region, it is possible to precisely target a desired point inside this region via a programmed manoeuvre of negligible intensity. This ability to target the required encounter is fundamental when the timing between the spacecraft and the Moon is introduced in the analysis.

5.2 ESCAPE TRAJECTORY

As mentioned, for the preliminary analysis of the flyby escape strategy the full trajectory is divided into two independent sections. From the analysis of the first section it was possible to characterize the manifolds departing from the PO and the associated inbound and outbound crossings. It was noted that the unstable manifolds encounter the lunar orbit only in specific sections. However, in order to keep the analysis as

general as possible, it is desirable to analyse the escape from every location on the lunar orbit, i. e., $\alpha \in [0, 360]$ deg.

Normally, in the PCR3BP the energy of an orbit remains constant, as it is an integral of motion. Its value can be modified only by applying a manoeuvre or via a flyby. This means that from the initial value C_{po} it is possible to obtain a variety of post-flyby conditions as to each possible incoming velocity vector and rotation angle corresponds a different post-flyby state vector and thus Jacobi Constant.

In order to fully cover the design space the description of the post-flyby state is adapted from the work by Nakamiya and Yamakawa [57]. In their work, they study the optimal escape trajectory from L_2 in order to reach a certain C_3 when escaping the Earth's SOI. To do so, the magnitude of the escape velocity at SOI is computed from C_3 . Similarly, once the post-flyby Jacobi Constant is fixed, it is possible to compute the magnitude of the associated velocity vector at each position on the lunar orbit, see Figure 5.4.

$$\mathbf{v}_2 = f(C_2, \, \alpha_2, \, \beta_2)$$

where the subscript $_2$ indicates the post-flyby condition. The function for v can is directly derived from Eq. 2.11, defining $v = \sqrt{\dot{x}^2 + \dot{y}^2}$

$$v = x^2 + y^2 + 2\frac{\mu_1}{r_1} + 2\frac{\mu_2}{r_2} + \mu_1\mu_2 - C_2 \tag{5.1}$$

$$x = x_\oplus + \tilde{a}_M \cos\alpha_2 \qquad\qquad y = \tilde{a}_M \sin\alpha_2$$

where $x_\oplus = 1 - \mu_{SE}$ as the Earth is assumed to be located at the EMB. Once the magnitude it is computed, the vector is obtained by spanning over β_2. The final velocity vector is then evaluated by rotating the local velocity vector (in the tangential-radial reference frame) to the desired location on the lunar orbit.

$$\mathbf{v}_2 = v \begin{bmatrix} \cos\alpha_2 & -\sin\alpha_2 \\ \sin\alpha_2 & \cos\alpha_2 \end{bmatrix} \begin{bmatrix} \cos\frac{\pi}{2} - \beta_2 \\ \sin\frac{\pi}{2} - \beta_2 \end{bmatrix} \tag{5.2}$$

To explore all possible post-flyby conditions, α_2 changes between 0 and 360° with steps of 0.5° while β_2 changes between 0 and 180°, again with 0.5° steps.

The so obtained states are then propagated forward in time over 1 year or until r_2^* is reached. In the case where the spacecraft does reach r_2^* the escape velocity is computed and stored in a matrix, otherwise the trajectory is considered to be *non-escaping.*
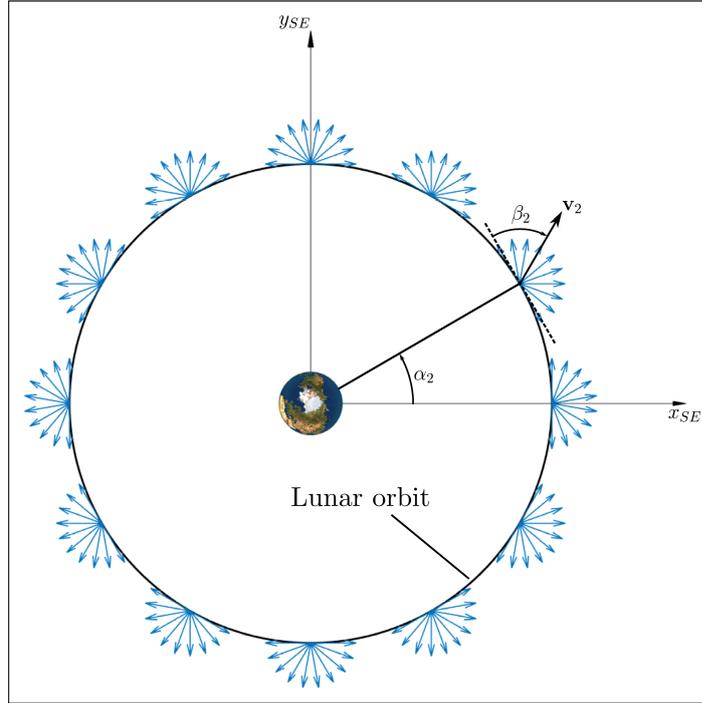
Figure 5.4: Definitions of the post-flyby conditions used for the analysis of the escape trajectory.

This computation is repeated for various energy levels ranging $C_2 = 2.9988 - 3.0009$ with a 5×10^{-5} step. While the lover limit was chosen arbitrarily, the upper limit comes from observation that lower energy departure conditions (higher Jacobi Constant) never escaped in the given amount of time. Some of the obtained results are shown in Figure 5.5 as higher-dimensional Poincaré sections constructed at the boundary of the SOI$_{SE}$; normally, Poincaré sections are only two dimensional, e. g., y-$\dot{y}$ or α-β planes, here the 'third dimension' is introduced as a *colormap* in order to represent the magnitude of the escape velocity.
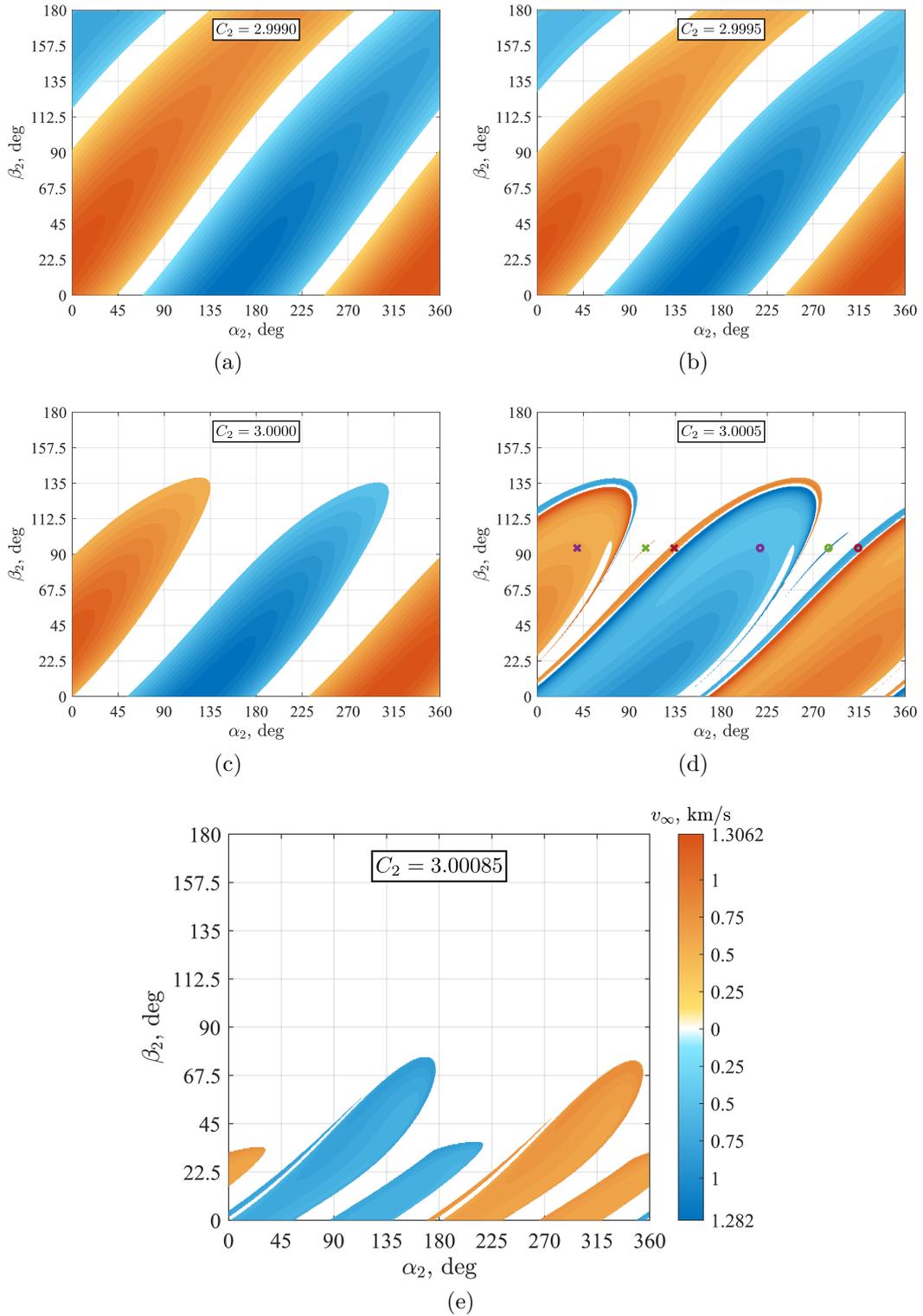
Figure 5.5: SOI_{SE} Poincaré sections representing the escape velocity for a variety of Jacobi Constant levels. Trajectories departing towards $R_c > 1$ AU are in orange and trajectories departing towards $R_c < 1$ AU are in blue.

The so obtained graphs give provide great insight in the behaviour of escape trajectories departing from the lunar orbit. As only the escape velocity is represented, it is impossible to directly observe the shape of the trajectory, however, some interesting conclusions can be drawn. It is apparent that, for increasing values of energy (decreasing C_2), the available initial conditions that ensure escape increase, covering more of the α_2-β_2 plane.

Furthermore, looking for example at Figure 5.5a, it can be observed that v_∞ is not independent of α_2 and β_2, in fact, the escape conditions can be divided into two regions, one going towards $R_c > 1$ AU (in orange) and one going towards $R_c < 1$ AU (in blue). Each of the *escape regions* appears to be convex, meaning that for each energy level unique 'optimal' initial departure condition can be found for both departure directions. While the value of $\alpha_{2,opt}$ varies between the two cases, for $R_c > 1$ it is approximatively 315° while for $R_c < 1$ it is approximatively 135°, the value of β_2 is in both cases equal to 0°, indicating a departure tangent to the lunar orbit. Note that this is also the optimal result of the gravity assist in terms of energy exchange, in fact, a departure parallel to the velocity vector of the exploited body indicates that $\mathbf{v_2} \parallel \mathbf{v}_{r,2}$, see Section 2.4, resulting in the maximum post-flyby velocity [44, 58].

Nonetheless, it is critical to understand that these optimal conditions are not always reachable for a variety of reasons, for example, in the case where $|\beta_1| \gg 0°$ the available bending angle could not be sufficient to obtain the desired tangential departure condition due to limitations on the flyby altitude. In some other cases, although $\beta_2 = 0$ would be achievable, it would not give the highest v_∞, as an example, in Figure 5.5b with $\alpha_2 = 225°$ the optimal value for β_2 is approximatively 67.5°.

Clearly this discussion is valid only when looking at a single energy level, differences become clear when taking a series of different C_2s, Figure 5.5. In particular, for increasing values of the Jacobi Constant a drift of $\alpha_{2,opt}$ towards lower values is observed introducing an additional difficulty in the design of the escape trajectory. Moreover, the aforementioned *regularity* of the escape regions is lost; while the main

lobe of each region is still present, some additional escape conditions can be identi-
fied. As discussed by Marchal [22] and Smith and Szebehely [59] in the special case
of the 'Copenhagen Problem' (PCR3BP with $\mu = 0.5$) and in accordance with the
numerical results in this more general case, the appearance of these irregular regions
is associated to the onset of chaotic behaviour in some of the obtained trajectories,
leading to an increased dependency on the initial conditions. The 'trigger' for this
behaviour can be found in the increase of the Jacobi Constant to a value close to the
one of the L_2 Libration point, $C_{L_2} = 3.0008968740$ [59].

To get a better understanding of what is intended with *chaotic behaviour*, a series
of trajectories are propagated taking the initial conditions from the main lobe and
the two chaotic region respectively, see Figure 5.5d. To prove the similarity between
the two departure directions, the three points are selected in both the orange and
the blue regions.

(a)

(b)
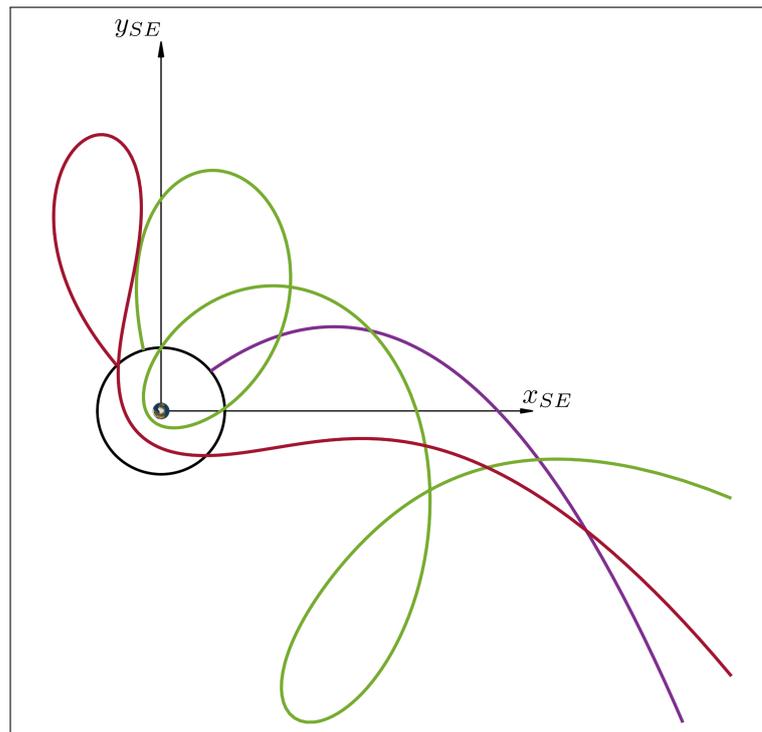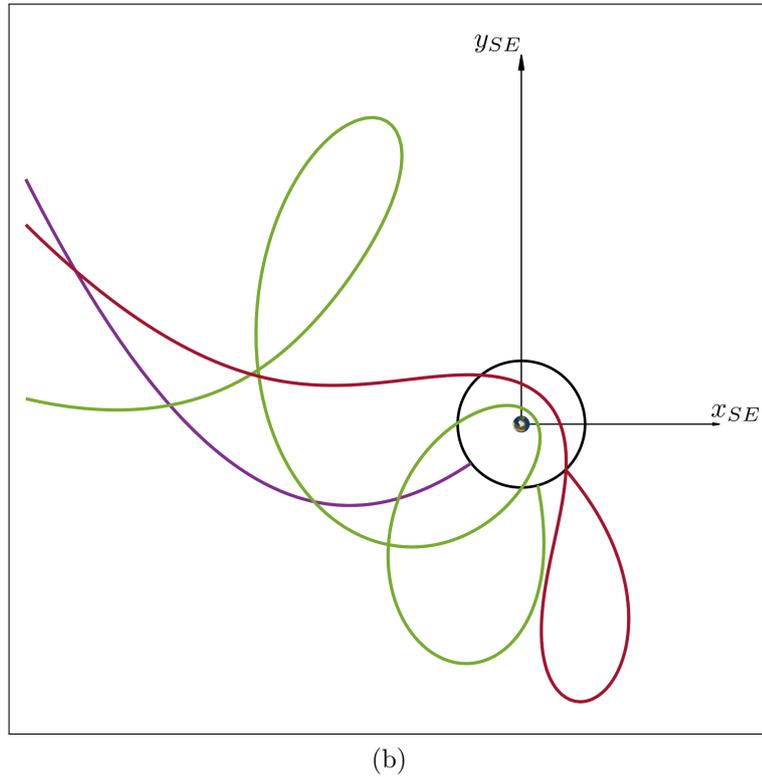
Figure 5.6: Examples of possible escape trajectories towards $R_c > 1$ AU (a) or towards $R_c < 1$ AU (b), identified respectively by $\times$ and $\mathbf{O}$ in Figure 5.5d.

The propagated trajectories clearly reflect the results depicted in the Poincaré sections. While the purple trajectory directly departs from the lunar orbit, both the green and the red ones (departing from the chaotic regions) return towards the cislunar spaces before finally departing, performing one or more revolutions around the Earth.

At this point it is useful to understand if these chaotic conditions should be included in the design process or if it would be better to neglect them. One one hand, going back to Figure 5.5, it appears that higher v_∞ values are achieved when departing in the neighbourhood of these regions; on the other hand, some arguments against their exploitation can be made:

- before departing towards interplanetary space, the spacecraft spends a considerable amount of time close to the Earth-Moon system. As the Moon's gravity is considered only at encounter, the used model for the propagation could be

inadequate to capture the real behaviour, and a higher-order model would be necessary also for an initial design;

- as mentioned, chaotic trajectories are highly dependent on the initial conditions. While for the nominal design this would not give particular problems, the real trajectory would be particularly susceptible to navigation errors during the transfer and during the flyby leading to stringent constraints for the Guidance, Navigation and Control (GNC) system which would not be necessary when targeting the regular regions.

In conclusion, the selection of the optimal departure condition is extremely complicated as multiple factors play their role, i.e., achievable α_2 and β_2 angles, variation of the behaviour due to changes in the energy levels, navigation constraints when exploiting chaotic regions, etc. Furthermore, until here the discussions of the two sections of the trajectory were considered as two separate problems. In fact, when they are considered together more problems arise:

- as the flyby is instantaneous $\alpha_1 = \alpha_2$, this limits the regions of possible departure;

- as each IC and OC has different relative velocity with respect to the Moon, also the available range for β_2 varies with each invariant manifold;

- the rotation of the velocity vector during the flyby not only impacts β_2, but also the value of C_2. This means that, considering a single encounter location, v_∞ for each β_2 needs to be identified on a separate energy level.

5.3   DESIGN APPROACH FOR THE FULL TRAJECTORY

In light of the aforementioned additional issues in the analysis of the coupled problem, it appears clear that an optimisation algorithm is necessary when the full problem is studied.

Furthermore, since the time at which a possible target is detected and the positions of the spacecraft and the Moon in their respective orbits cannot be predicted, a simple optimisation is not sufficient to obtain meaningful predictions of the v_∞ values that can be expected, and thus, considered for the optimisation of the interplanetary arc. However, both issues, i. e., the coupling of the two sections and the timing problem, can be readily integrated through the setup of a Monte Carlo Simulation (MCS).

5.3.1   *Optimisation Algorithm*

The objective of the coupled analysis is to identify particular trajectories, that involve a single lunar flyby, to achieve the maximum escape velocity. This objective translates into an optimisation problem which needs to be defined by identifying:

- the vector of design variables that drive the problem;

- the lower and upper bounds of these variables;

- the so called *fitness function* that needs to be minimised.

For the problem at hand the selected design variables are: the time between $t_{po,0}$ and the departure from the parking orbit, t_{dep}, this variable uniquely identifies the departure location of the spacecraft (without perturbation), and the altitude of the lunar flyby, h.

As discussed in Section 5.1, from a single departure location, a variety of possible manifolds can be identified, it is thus necessary to select the correct initial conditions

to precisely cross the lunar orbit when the Moon is in the right position. This requires the solution of a so called *timing problem* which is mathematically defined in Eq. 5.3.

$$\min \left|\alpha_{1,in} - \theta_{M,in}\right| \quad \text{and} min\left|\alpha_{1,out} - \theta_{M,out}\right| \tag{5.3}$$

where α_1 identifies the crossing location and θ_M the lunar position at the same instant for respectively the IC and the OC. The values of $\theta_{M,in}$ and $\theta_{M,out}$ can be readily computed knowing the the departure location on the periodic orbit and the initial phase of the Moon, $\theta_{M,0}$, in particular,

$$\frac{\theta_{M,0} + 2\pi(t_{coast} + tof)}{T_{\mathbb{C}}} \; (\text{mod } 2\pi) \tag{5.4}$$

where $t_{coast} = t_{dep} - t_{po,0}$ and $T_{\mathbb{C}}$ is the nondimenisonal orbital period of the Moon.

Clearly Eq. 5.3 depends on multiple variables such as the initial positions of the Moon and the spacecraft, but also of the considered invariant manifolds. The minimization process is thus extremely time consuming as there is no analytical correlation between the values of δP, δV and the time of flight or the crossing location making it necessary to use numerical propagation. However, the computational cost of the minimization is reduced by building a database of invariant manifolds where the required characteristics are stored, e. g., α_1, β_1 tof, etc. This database is obtained by finely discretizing the δP and δV intervals for a set of initial points on the PO, in particular, for the present study 1 000 points on the periodic orbit are considered and the discretization steps are 10 km and 0.1 m/s. Once t_{dep} is known, it is then possible to write Eq. 5.3 in vectorial form leading to a much simpler solution of the timing problem. In general, with the considered discretization, the obtained angular distances are around $10^{-3\circ}$ resulting in an extremely accurate targeting of the flyby.

The bounds adopted for the optimisation are $[0, 8]$ months for the waiting phase on the parking orbit and $[5\,000, 35\,000]$ km for the altitude. The limit of 8 months is

considered as valid as it allows for more than one complete rotation on the periodic orbit, giving the possibility to identify the optimal departure location and phasing with the Moon, without excessively compromising the total time budget for the full trajectory, in fact, it was observed that with waiting phases longer than 8 months there was not sufficient time to reach r_2^* leading to a 'no-escape' trajectory. Both limits of the flyby altitude are suggested in the CReMA [38], the selection of the lower limit aims at simplifying the navigation of the lunar flyby while 35 000 km is considered as the maximum distance at which the Moon as appreciable influence on the escape conditions, higher flybys lead to trajectories asymptotic to the direct escape. However, in light of the work done by other researchers, after a first analysis with the original limit, it was considered to analyse escape trajectories with flyby limits as low as 100 km [43, 44, 60, 61]; the results are presented in Section 6.2.

Finally, as the objective is to maximise the escape velocity, the definition of the fitness function, J, is straightforward. However, since Eq. 4.4 returns results with opposite sign when computed for trajectories going towards $R_c > 1$ AU or $R_c < 1$ AU, two separate functions need to be defined. Furthermore, going back to Section 2.4 and Section 5.1 and considering the selected design variable, it appears that the trajectory is not uniquely defined. In fact, considering a single manifold, two possible encounters can theoretically happen, one at the IC and one at the OC. In addition to that, the flyby can result in a CW or in a CCW rotation. These two considerations lead to four different trajectories for each combination of the design variables. To avoid the introduction of additional design variables in the optimisation, which furthermore would be *integers*, it is chosen to propagate all four trajectories and 'collect' the respective escape velocities in a vector, $\bar{v}_\infty$ to then consider only the optimal one.

$$
\begin{aligned}
&\text{- } R_c > 1 \text{ AU} &&\rightarrow &&J = \min\left(-\bar{v}_\infty\right) \\
&\text{- } R_c < 1 \text{ AU} &&\rightarrow &&J = \min\left(\bar{v}_\infty\right)
\end{aligned}
\tag{5.5}
$$

Due to the complexity of the problem, e. g., numerical integration, number of variables, nonlinearity of the equations, etc., it is not possible to apply traditional search techniques which involve the use of gradients, Hessians or other characteristics of the problem. For this type of problems it is suggested to use *stochastic sampling methods*, these are iterative methods which determine the next iteration by following stochastic sampling or a particular set of rules. For the solution of this problem it was opted for the use of a *genetic algorithm.*

Genetic algorithms are initialized by sampling the entire design space, for each member of the initial population the fitness function is then evaluated. The following iterations are computed following the rules of reproduction and mutation of the individuals with the best fitness function. The advantage of such methods is that multiple 'promising' regions of the design space can be evaluated at the same time reducing the risk of converging to local minima. A more detailed discussion can be found in the works by [62–65].

For the solution of the optimisation problem the Matlab's built-in *genetic algorithm* is used with the following options.

Maximum number of iterations	150
Maximum number of stall iterations	20
Initial population size	1 000
Function tolerance	0.001

Table 5.1: Options applied to Matlab's genetic algorithm for the optimisation of the trajectory.

While initial simulations were run on a laptop with a smaller population size, it was observed that, it was not possible to converge regularly to the same solution (or to its neighbourhood). Thus, the simulation was finally run on the High Performance Computer (HPC) of the University of Cranfield, allowing for a larger population due to the increased computational power.

As mentioned, a single optimisation does not give meaningful results for the problem at hand, thus the Monte Carlo Simulation is performed in order to give a statistical description of the obtained results.

5.3.2 *Monte Carlo Simulation Setup*

The main quantity of interest of the analysis is the *expected value* of the escape velocity, as it influences the rest of the design of the mission. Mathematically this value can be defined as

$$E[v_\infty(X_1, X_2, ... X_n)] = \iint ... \int v_\infty(x_1, ..., x_n) f(x_1) f(x_2) ... f(x_n) dx_1 dx_2 ... dx_n \quad (5.6)$$

where $f(x_1)f(x_2)...f(x_n)$ are the density distributions of the random variables X_i. In general, it is impossible to evaluate analytically this equation, however, by following the Monte Carlo simulation approach it is possible to obtain a reasonable close approximation of the integrals [66]. In fact, by performing N simulations of the same process

$$Y^1 = v_\infty^1(X_1^1, X_2^1, ... X_n^1) \qquad Y^2 = v_\infty^2(X_1^2, X_2^2, ... X_n^2) \qquad (5.7)$$

where each set of random variables is independent and generated following its density function, f it can be concluded that

$$\lim_{N \to \infty} \frac{Y^1 + ... + Y^N}{N} = E[Y_i] = E[v_\infty(X_1, X_2, ... X_n)] \qquad (5.8)$$

In the problem at hand the random variables X_i are the position of the Moon in its orbit, $\theta_{M,0}$, and the position of CI in its parking orbit, $t_{po,0}$, at $t = 0$, i. e., the moment at which the orbital characteristics of the comet are known allowing for the design of the trajectory, as these quantities cannot be predicted during the initial design phase of the mission. Both variables are sampled following a uniform distribution, f

in Eq. 5.6, between 0 and 360° for the Moon phase angle and between 0 and T_{po} for the position of Comet Interceptor. Since each simulation is independent, it is possible to parallelize the simulation and fully exploit the capabilities of the HPC reducing drastically the computational time.

Combining together the Monte Carlo approach and the optimisation it is expected to find a series of optimal escape trajectories for both departure direction, furthermore, the distribution of the obtained v_∞ will provide the reader with an indication on how the optimal escape behaves with different initial conditions.

5.4   RESULTS FROM THE MONTE CARLO SIMULATION

In light of the presented analysis it is possible to design two escape trajectories, one for each direction. Since the optimisation process does not find the exact minimum of the fitness function, each run of the Monte Carlo Simulation gives a slightly altered result, however, the overall behaviour of the trajectories is the similar . In Figure 5.7 two examples of the obtained trajectories are represented, each one is divided into three section:

1. the waiting phase: here the spacecraft continues on its path on the parking orbit until it reaches the designed departure point;

2. the invariant manifold: this section was previously discussed and connects the departure point to the lunar encounter where the flyby happens;

3. the escape trajectory: also this section was previously discussed and considers the entire trajectory after the flyby until r_c^* is reached.
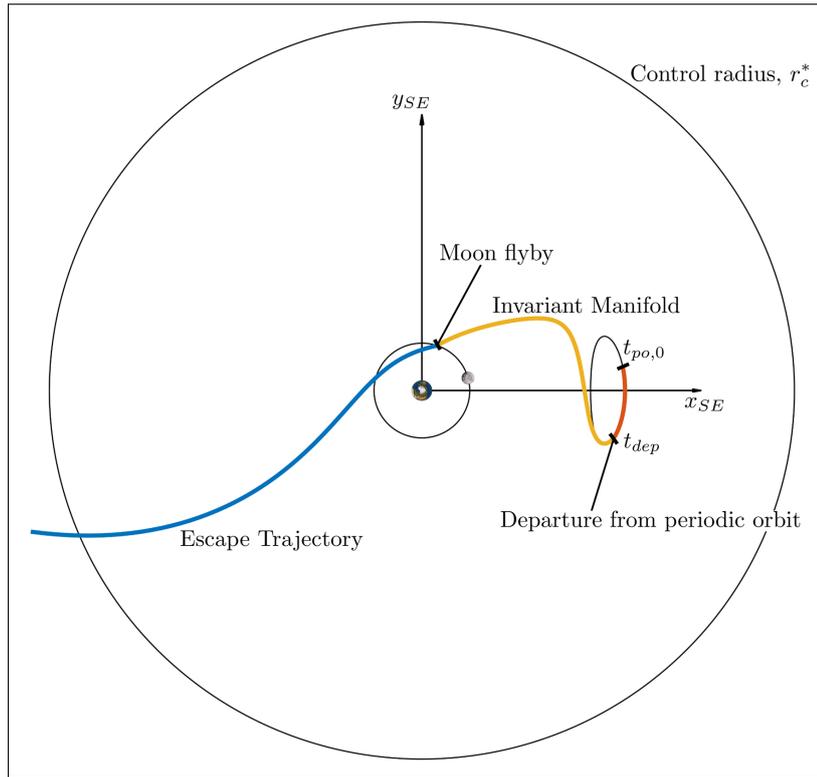
(a)
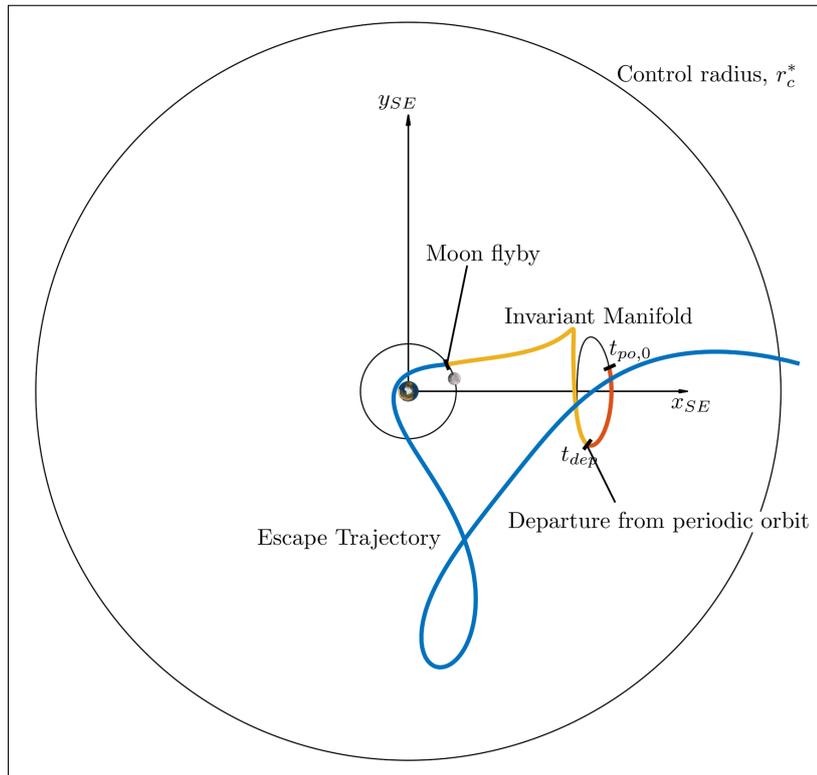
(b)

Figure 5.7: Optimised escape trajectories towards $R_c > 1$ AU (b) and towards $R_c < 1$ AU (a) obtained from one run of the Monte Carlo Simulation. r_c^* is not in scale.

While it is interesting to observe the shape of the obtained trajectory, the fundamental result is the Probability Density Function (PDF) of the escape velocities in Figure 5.8. It is estimated that 400 simulations are sufficient to obtain a good approximation of $E[v_\infty]$, this estimation is based on the fact that the simulation was divided into four batches of 100 simulations which all presented the same behaviour.

From Eq. 5.8 and observing the figure above it can be estimated that

$$
\begin{aligned}
- R_c > 1 \text{ AU} &\quad \rightarrow \quad E[v_\infty] = 0.98 \text{ km/s} \\
- R_c < 1 \text{ AU} &\quad \rightarrow \quad E[v_\infty] = 1.04 \text{ km/s}
\end{aligned}
\tag{5.9}
$$

resulting in a 'free' increase of approximatively 180 m/s with respect to the direct departure. Furthermore, as the available tof is limited, due to the limited notice time, it is also necessary to observe how the time of flight behaves for these trajectories. As for the flyby trajectories the waiting time on the periodic orbit is considered in the total tof, it is necessary to include it also in the computation of the time of flight of the direct trajectories. The obtained results are summarized in Table 5.2.
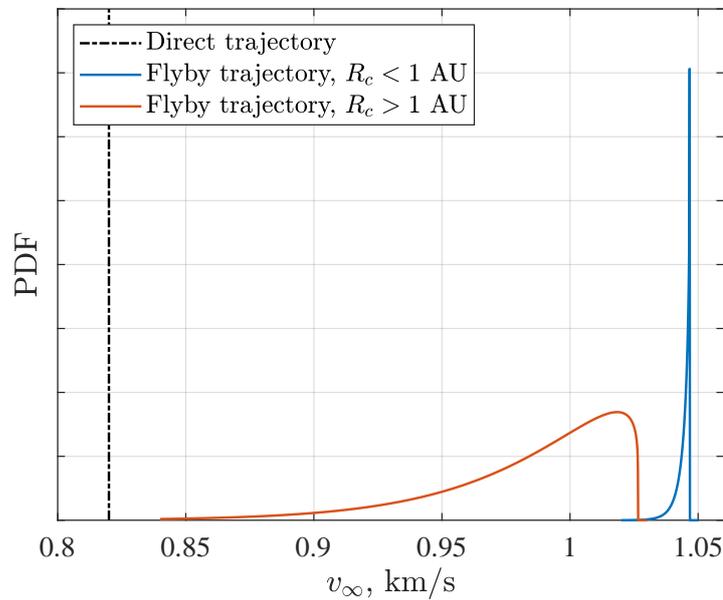

Figure 5.8: PDF of the escape velocities obtained from the Monte Carlo Simulation.

(a) $R_c < 1$ AU

(b) $R_c > 1$ AU
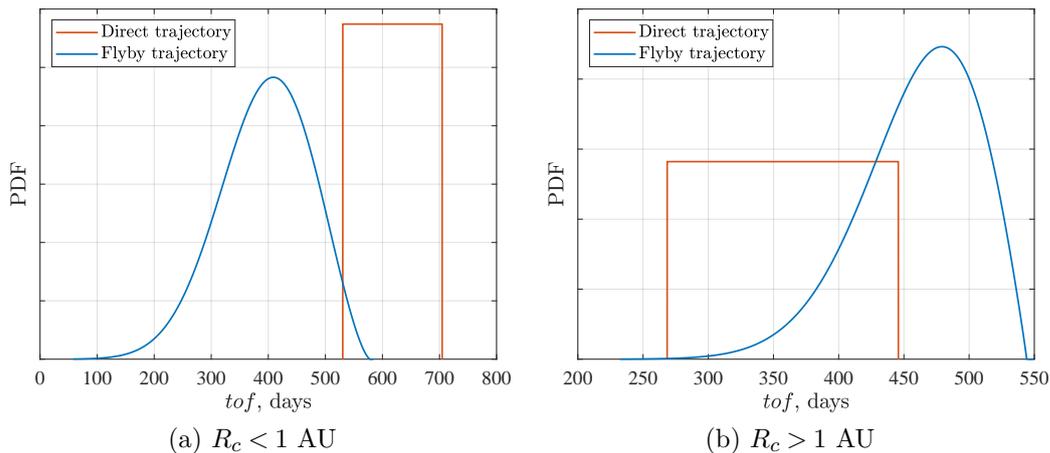
Figure 5.9: Comparison between the time of flight of the direct escape and the flyby escape obtained from the Monte Carlo Simulation.

Combining the information in Figure 5.8 and Figure 5.9a it appears that the introduction of the gravity assist when targeting a comet flyby closer than 1 AU to the Sun does only have positive effects. In fact, not only is there an increase of around 200 m/s in escape velocity, increasing the regions which can be targeted [9], but the tof is also clearly reduced, allowing for a shorter notice period between the discovery of a DNC and the programmed flyby time.

On the other hand, while an increase of escape velocity can be observed also for the trajectories going towards regions further than 1 AU from the Sun, around 160 m/s, here the required time of flight increases sensibly as the spacecraft needs to enter the cislunar space before actually escaping towards interplanetary space. This introduces an additional variable in the design process as for each specific comet it is necessary to evaluate if the increase of tof is balanced by an adequate increase of v_∞.

Target region	$R_c < 1$ AU		$R_c > 1$ AU	
	$E[...]$	Δ	$E[...]$	Δ
$v_{\infty,dir}$, m/s	816.9		825.2	
$v_{\infty,fb}$, m/s	1044.2	227.3	983.7	158.5
tof_{dir}, days	621.2		361.0	
tof_{fb}, days	392.5	228.7	460.5	99.5

Table 5.2: Summary of the results and the comparison between the direct and the flyby escape strategies.

5.4.1 *Optimal Design Variables*

While the results above answer some of the key questions of this thesis, they do not give the complete picture of the problem. In order to fully understand and validate the obtained results it is also necessary to analyse the *design variables* as they describe two fundamental moments of the trajectory, i. e., the departure from the periodic orbit and the flyby.

Clearly t_{dep} by itself does not provide any information, only when taken together with $t_{po,0}$ it describes the departure position on the PO. Figure 5.10 shows a selection of departure locations represented on the PO as it is clearer then the time information.
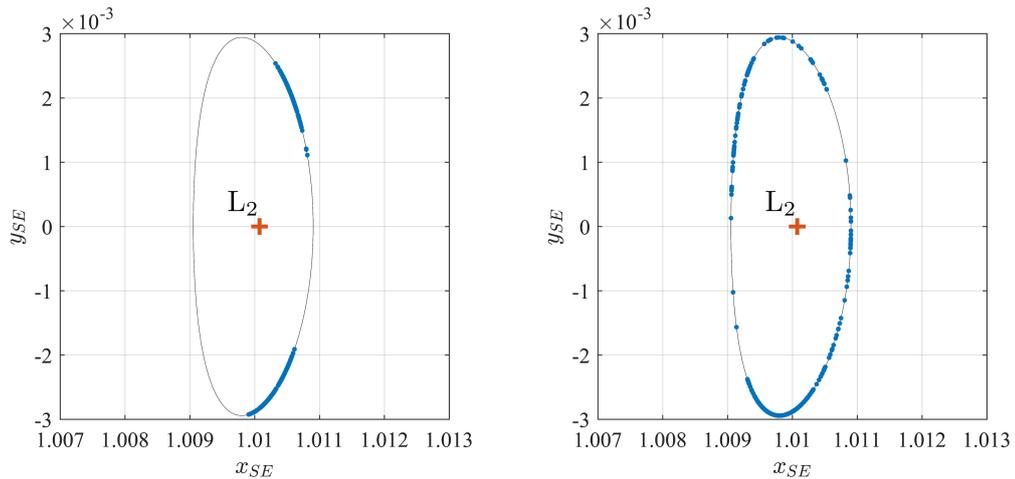
(a) Departure locations towards $R_c < 1$ AU   (b) Departure locations towards $R_c > 1$ AU
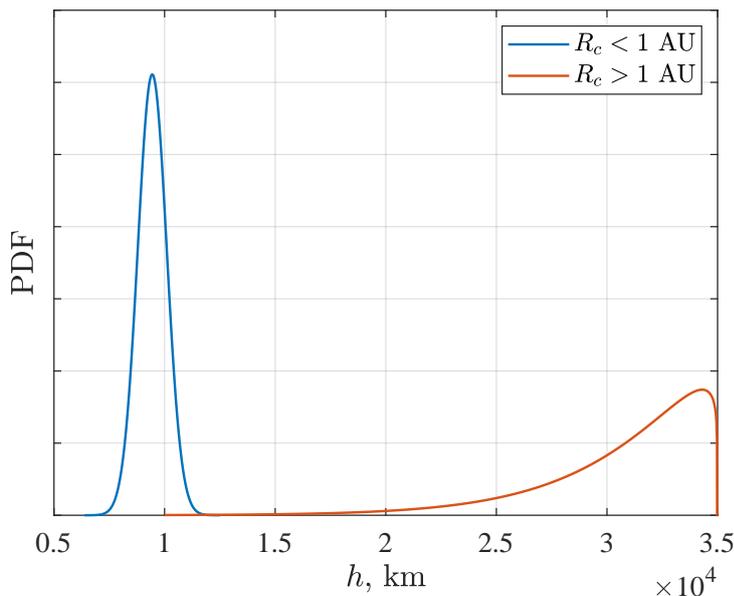
(c) Moon flyby altitudes

Figure 5.10: Optimal design variables obtained through the optimisation process.

As for the PDF of v_∞ and the tof, also here it can be observed that the design variables present a greater variety when departing towards $R_c > 1$ AU. In particular, while in Figure 5.10a it is clearly possible to distinguish two preferred departure regions, in Figure 5.10b this is much more difficult, it seams that the 'bottom' of the periodic orbit is advantaged by the optimisation but a variety of trajectories depart also from other regions. Furthermore, this behaviour is also visible in Figure 5.10c, where the optimal flyby altitudes are tightly distributed around the expected value $E[h] = 9\,442.3$ km when going towards $R_c < 1$ AU, whilst, when the target is $R_c > 1$ AU the distribution is much wider with $E[h] = 30\,697.3$ km.

Considering the differences between the PDFs when changing from one escape direction to the other and by comparing the obtained trajectories with Figure 5.6, it appears that the trajectory towards $R_c > 1$ AU is close to a chaotic trajectory. In fact, this would explain the wider distributions as in presence of chaotic behaviours a variety of local minima could appear. Furthermore, the appearance of the 'loop' in the optimal trajectory, similar to the trajectories in Figure 5.6a, also suggests that

the post-flyby Jacobi Constants is close to the value considered for Figure 5.5d and thus close to the critical value that indicates the onset of chaotic behaviours.

However, in order to confirm this suspicion it is necessary to locate the optimal trajectories on the previously defined Poincaré section, note that the characteristics represented there are considered when leaving the lunar orbit and are not necessary the post-flyby conditions. Figure 5.11 is constructed by computing the mean $C_{2,opt}$ of the optimal post-flyby trajectories in order to have a good approximation of the two energy levels (one for $R_c < 1$ AU and one for $R_c > 1$ AU). Then the post-flyby condition is propagated until leaving the lunar orbit where $\alpha_{2,opt}$ and $\beta_{2,opt}$ are evaluated for each trajectory, for a clearer representation only a fraction of the obtained results are displayed.

As expected, the use of a Poincaré section and the positioning of the optimal trajectories in it gives a better understanding of the obtained results as it is possible to characterise the different trajectories.
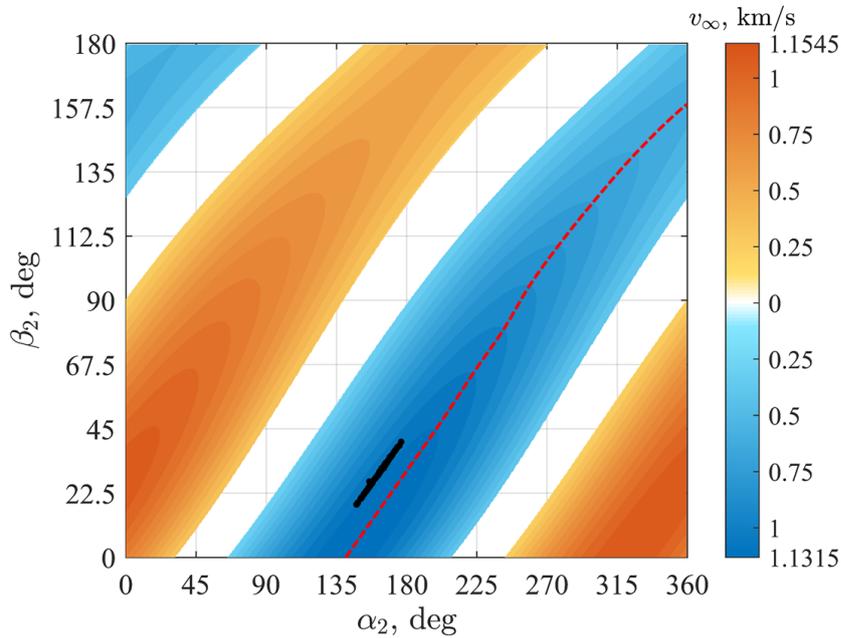

(a) $R_c < 1$ AU, $C_{2,opt} \approx 2.99943$

(b) $R_c > 1$ AU, $C_{2,opt} \approx 3.00034$
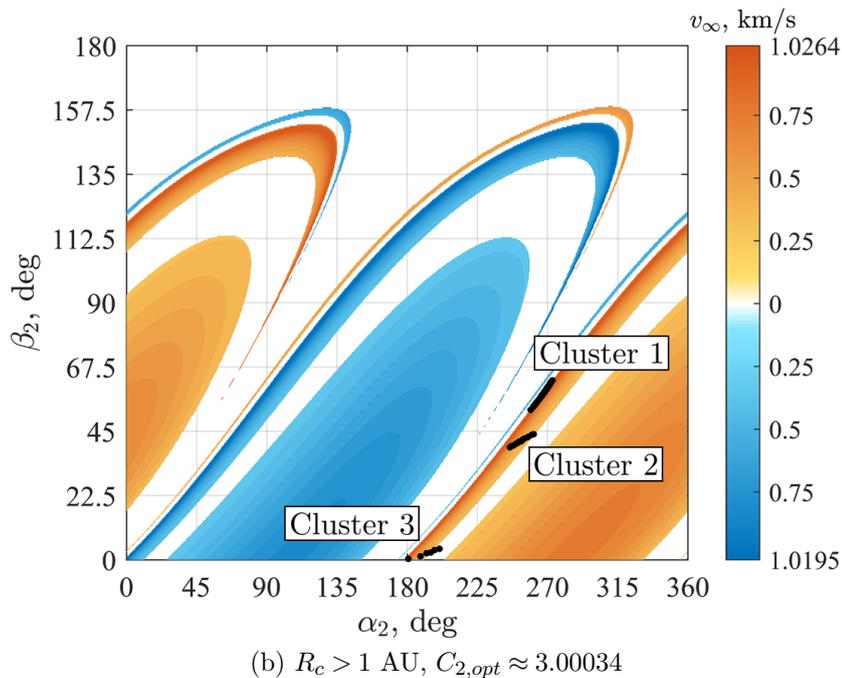
Figure 5.11: Poincaré Maps of the optimal C_2 levels with a selection of obtained trajectories shown as black points.

In fact, starting from Figure 5.11b, the aforementioned suspicion is confirmed as all the trajectories lie inside the chaotic region. Furthermore, it is possible to identify three different types of orbits thanks to the clustering of the different points, this difference is also reflected by the actual shapes of the trajectories shown in Figure 5.12.

Clearly only cluster 1 follows exactly the optimal curve of the chaotic region, while clusters 2 and 3 appear to be 'non-optimal' looking at the maximum v_∞ values that appear in the same region. Assuming that the optimisation converged to the global minimum for every cluster, the differences could be explained by the variability of the initial conditions, $\theta_{M,0}$ and $t_{po,0}$ which presented encounters only when departing from non-optimal regions of the periodic orbit, only the trajectory from cluster 1 in Figure 5.12 departs from the 'bottom' region which, recalling Figure 5.11b, appears to present the optimal departure conditions.
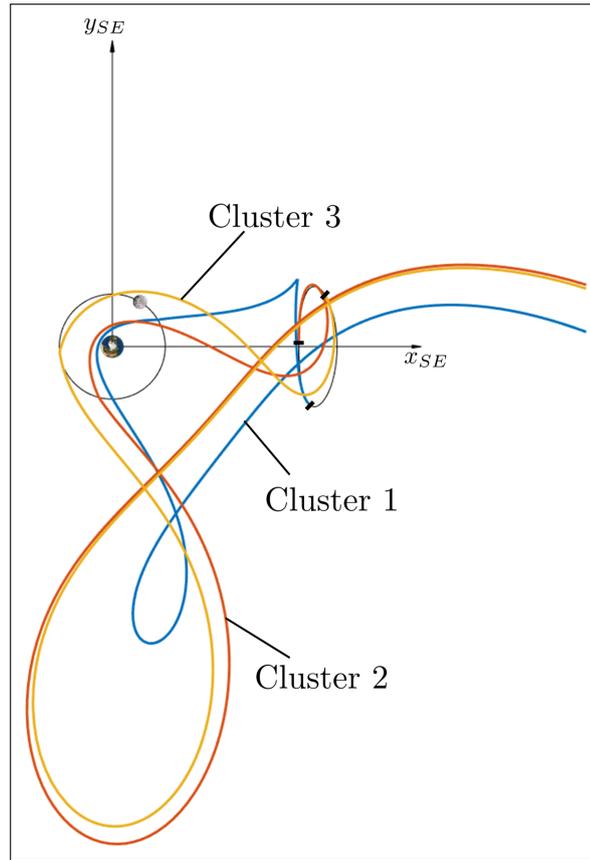
Figure 5.12: Examples of escape trajectories from the three clusters identified in Figure 5.10b.

Moving now to the trajectories departing towards $R_c < 1$ AU in Figure 5.11a, it is immediately clear that the behaviour is more regular as all obtained trajectories nicely follow the optimal curve. However, despite presenting this regular behaviour, the obtained results do not follow the 'centre-line' (in red) representing the optimal departure flight path angle as function of α_2, $\beta_{2,opt} = f(\alpha_2)$. It is thus considered to lower the altitude of the flyby closer to h_{LB} resulting, theoretically, in an increased post-flyby energy and thus higher escape velocities. However, as can be seen in Figure 5.13, the lower flyby did not simply increase the energy level, effectively increasing the maximum v_∞ levels, it also changed the position of the α_2-β_2 points resulting in and escape trajectory with lower Jacobi Constant, 2.99899 vs 2.99943 but lower escape velocity.
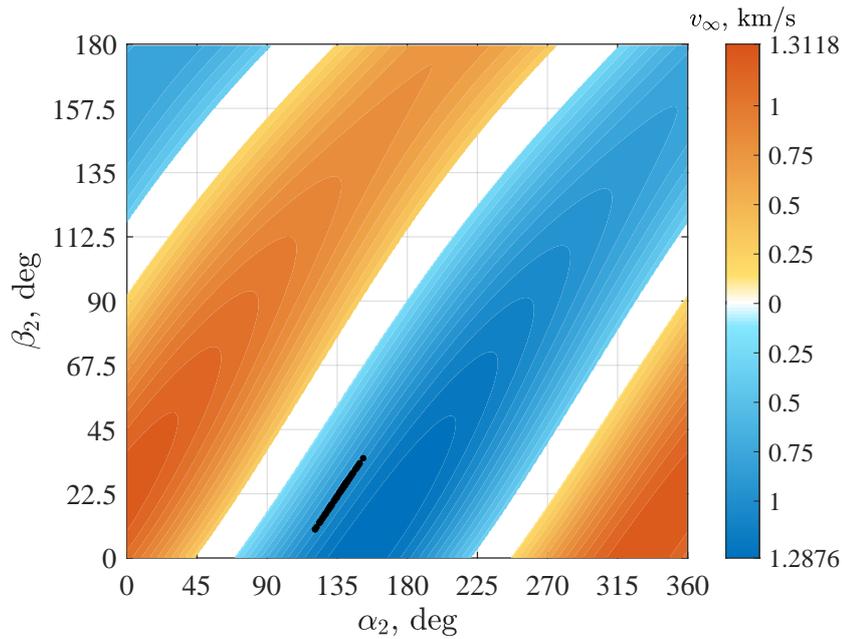
Figure 5.13: Poincaré section of the optimal trajectories of Figure 5.11a recomputed with a lower flyby altitude.

In conclusion, while it is possible to perform an initial analysis separating the two section of the trajectory, in order to obtain meaningful results it is necessary to study the coupled problem introducing also the correct timing conditions. Only through this complete analysis it is possible to compute an estimate of the escape velocity without committing the error of considering escape trajectories impossible to achieve with a single flyby strategy. Furthermore, it is observed that a fundamental step in the analysis process is the fine tuning of the optimisation algorithm, in particular when departing towards $R_c > 1$ AU where the onset of chaotic behaviour can be expected.

6

ADDITIONAL ANALYSIS

THE scope of this chapter is the analysis of some additional aspects regarding the trajectory design of Comet Interceptor. While the main focus of this work was the estimation of the expected value of the escape velocity, with the developed framework it is possible to further analyse some fundamental aspects of the trajectory design, laying the basis for future future work. The aspects which are analysed hereafter are:

1. the estimation of the navigation cost for the designed trajectory;

2. the analysis of the advantages achievable through lower flyby altitudes;

3. the propagation of the obtained trajectories in a higher-order model;

4. the evaluation of the full transfer from L_2 to a desired comet.

6.1 NAVIGATION

The entire analysis until here focused on the evaluation of possible escape trajectories and are based on the perfect knowledge of the spacecraft's state. However, a variety of factors, e. g., modelling errors due to non considered additional forces, orbit injection errors, tracking errors, manoeuvre execution errors, etc., influence in an unpredictable way the dynamics of the spacecraft, in fact, while some errors can be reduces by

considering high-fidelity models, some others are inevitable due to limitations of the used systems.

When studying the Δv budget of a mission, it is thus necessary to analyse the *navigation cost* of the nominal trajectory. The following analysis makes use of the differential correction algorithm to compute the required manoeuvre to follow as closely as possible the original trajectory but considering uncertainties in the state of the spacecraft $(x, y, \dot{x}, \dot{y})$ and in the execution of the required manoeuvre. These errors are stochastic in nature, thus cannot be evaluated exactly. The only way to account for these errors is by performing multiple simulations (Monte Carlo approach) where the perturbed trajectory is propagated over a certain amount of time before applying the correction manoeuvres. Finally, the different costs are summed together to get the total Δv required for the navigation. The elapsed time between one manoeuvre and the other is necessary in order evaluate the parameters of the real trajectory, compare it with the nominal one and compute the required correction manoeuvre, for simplicity, in this analysis the Δt is kept constant over the entire trajectory.

In general, due to their nature, the considered errors are modelled as Gaussian distributions that can be described by their mean, η, and their standard deviation, σ. η indicates the *median* or *mode* of the error and in general is 0 (otherwise constant errors are present and can be included in the model) and σ indicates the dispersion of a set of values, in particular, it tells that 68.2% of the random values are in an interval of $\pm\sigma$ around η, sometimes 3σ is used to account for the 99.7% of the values.

Starting from the nominal departure state, $\mathbf{x}_{0,pert}^0 = \mathbf{x}_{dep}$, the trajectory is iteratively perturbed and propagated until the desired target is reached, hereafter a description of each cycle is presented:

1. a perturbation is applied to the nominal/corrected state before the propagation in order to consider errors in the orbit determination: $\mathbf{x}_{0,pert}^i = \mathbf{x}_0^i + \Delta\mathbf{x}$;

2. the perturbed state is integrated over the time span Δt obtaining the final state $\mathbf{x}_{pert}^i$;

3. the differential corrector is applied to the final state of the perturbed trajectory, obtaining the nominal correction manoeuvre, $\Delta\mathbf{v}$, needed to reach the desired target from $\mathbf{x}_{pert}^i$;

4. a perturbation is applied to the magnitude of the nominal manoeuvre obtaining $\Delta\mathbf{v}_{pert}^i$, the direction is considered as fixed;

5. the perturbed manoeuvre is applied to $\mathbf{x}_{pert}^i$: $\mathbf{x}_0^{i+1} = \mathbf{x}_{pert}^i + \Delta\mathbf{v}_{pert}$;

Note that no manoeuvre is performed when $|\Delta\mathbf{v}|$ is of the same order of magnitude as the hardware limitations of the propulsive system, this limit is set to 0.15 cm/s [37]; in these cases step 3 is directly followed by step 1, and thus, $\mathbf{x}_0^{i+1} = \mathbf{x}_{pert}^i$.

As the distribution of the error very much depends on the characteristics of the orbit determination systems, various Monte Carlo simulations are performed with different σ-values; the uncertainties can be found in Table 6.1 together with the total Δv budgets.

Taking as a reference ESA's guidelines, the maximum allowable budget for the navigation should be 25 m/s [38]. Looking at the results in Table 6.1, it is observed that the obtained results are, not only under the allowed budget, but also in line with what was achieved for the ISEE-3 mission where 5 m/s were required for the navigation [43].

Reference	$\Delta\mathbf{x}$ error* (σ), km mm/s	$\|\Delta\mathbf{v}\|$ error (σ)	$E[\Delta v_{tot}]$**, m/s Δt			
			14 days	21 days	28 days	56 days
[67, 68]	[1.46, 2.64] [1.40, 1.85]	10 %	0.47 0.18	0.56 0.11	0.10 0.28	0.41 0.27
[69, 70]	[1.50, 2.50] [1.00, 1.00]	2.5 %	0.38 0.13	0.44 0.08	0.07 0.20	0.22 0.20
[71]	[1.70, 2.20] [1.40, 1.40]	2.5 %	0.41 0.16	0.51 0.10	0.08 0.25	0.27 0.25
[72, 73]	[3.00, 30.0] [15.0, 15.0]	2.5 %	4.27 1.69	5.14 1.00	0.82 2.64	2.35 2.61
[74]	[3.00, 30.0] [15.0, 15.0]	5 %	4.32 1.70	5.19 1.02	0.83 2.60	2.66 2.61
[75]	[3.00, 30.0] [15.0, 15.0]	10 %	4.38 1.75	5.20 1.05	0.87 2.70	3.59 2.65

* 1st row: perturbation of x and y, 2nd row: perturbation of $\dot{x}$ and $\dot{y}$

** 1st row: departure towards $R_c < 1$ AU, 2nd row: departure towards $R_c > 1$ AU

Table 6.1: Expected navigation budgets computed via Monte Carlo simulation.

However, the expected value does not give the entire picture of the analysis, in fact, looking at Figure 6.1 it appears that only in some cases the results are tightly distributed around $E[\Delta v_{tot}]$, in particular for $\Delta t = 28$ days ($R_c < 1$ AU) and for $\Delta t = 21$ days ($R_c > 1$ AU).
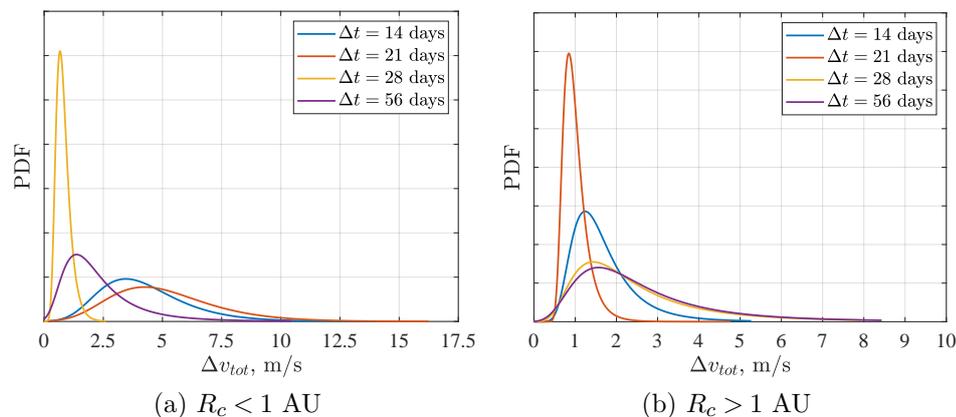

Figure 6.1: PDFs of the total navigation budget computed from the error values considered by Howell and Keeter [72, 73].

Furthermore, while in the represented cases the maximum values are still under 25 m/s, it was observed that for some of the considered error levels values as high as 30 m/s are required to navigate the full trajectory when considering a propagation time span of 56 days. All considered, it is expected that the available budget is sufficient to navigate the trajectories obtained from the optimization process, especially when considering the 28 and 21 days 'strategies'.

6.2 EVALUATION OF A LOWER FLYBY ALTITUDE

As aforementioned, in the literature it is possible to find a variety of missions that exploit flybys at altitudes lower than $5\,000$ km. In the following section it is evaluated if a closer flyby could be advantageous in light of the increased difficulty in the navigation of such a flyby. In particular, closer flybys would increase the range of achievable bending angles, δ, obtaining larger trajectory changes from the lunar encounter. As the upper-bound is kept constant, the already obtained results should be obtained when the global h_{opt} lies above $5\,000$ km.

The analysis is performed by re-optimizing the entire trajectory varying the lower-bound of the flyby altitude, h_{LB}, in the *genetic algorithm* options while the rest of the optimization process is analogue to the previous analysis. The selected interval of interest for h_{LB} is $[100, 4900]$ km, thus, 49 independent optimizations are performed to find the optimal flyby for the new trajectories. However, as the focus lies on the analysis of h_{LB}, the initial conditions are kept constant over all simulations eliminating the variability coming from different positions of the Moon and the spacecraft in their respective orbits.

(a) Optimized escape velocities

(b) Flyby altitudes of the optimized trajectories
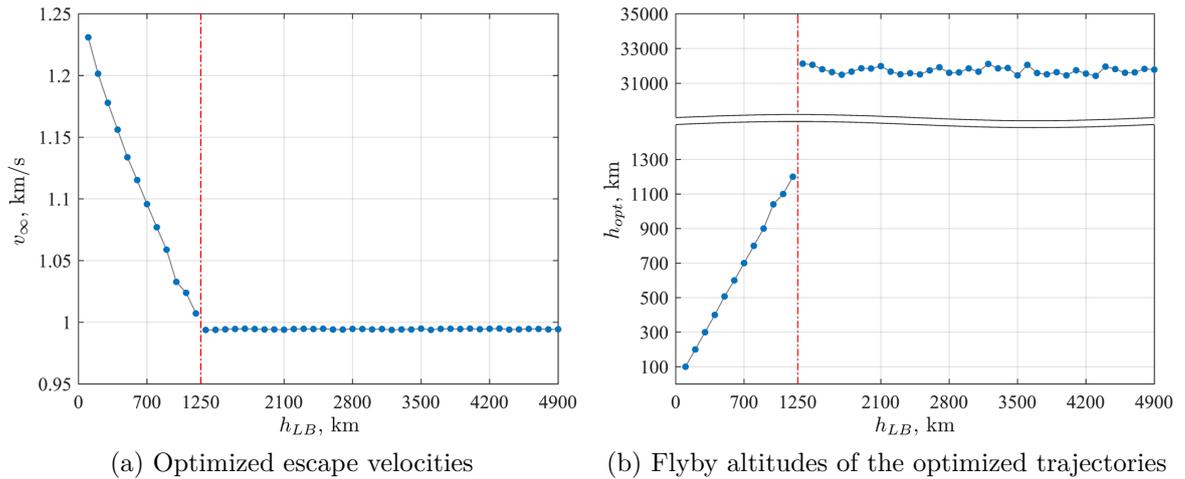
Figure 6.2: Results of the optimization process when a lower altitude bound, h_{LB}, is considered

Since when departing towards $R_c < 1$ AU there was no improvement with respect to the analysis with the nominal flyby limit, its analysis is not discussed hereafter. However, when departing towards $R_c > 1$ AU the obtained results are very interesting. Looking at Figure 6.2 two regions can be identified, one above $1\,250$ km and one below. In the former a quasi-linear behaviour can be observed between the increase of v_∞ and the decrease of h_{LB}, while in the latter the optimization process leads to the same results as for $h_{LB} = 5\,000$ km. A similar behaviour is observed for the optimal flyby altitudes of these escape trajectories, see Eq. 6.1. To illustrate the difference between the nominal and the 'improved' trajectory, the two are represented together in Figure 6.3.

$$h_{opt} \approx \begin{cases} h_{LB}, & \text{if } h_{LB} \in [100, 1\,250] \text{ km} \\ \\ 31\,733 \text{ km}, & \text{if } h_{LB} > 1\,250 \text{ km} \end{cases} \tag{6.1}$$

In conclusion, while a sensible improvement in the escape characteristics of the trajectory can be achieved, at best an additional 240 m/s, by lowering the flyby, the difference between the initial limit and the required one is substantial, one order of

magnitude, introducing potential issues connected to the low flyby, e. g., interruption of Earth-S/C communication, stricter GNC system requirements.
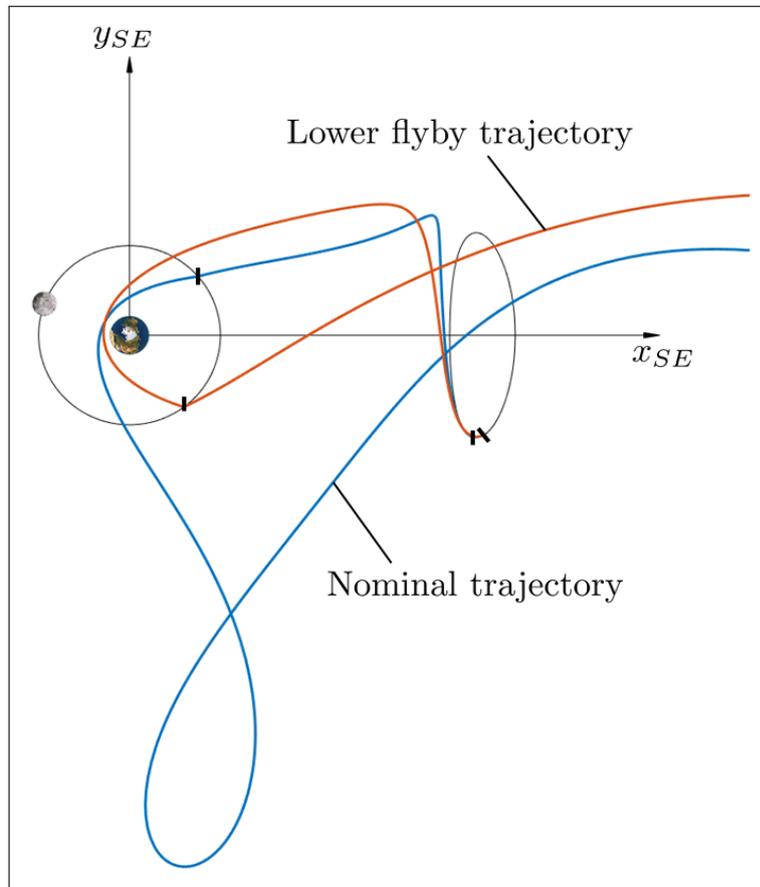

Figure 6.3: Comparison between the nominal trajectory and one with a 300 km low flyby.

6.3 HIGHER-ORDER MODEL

In order to simplify the analysis and the design the lunar gravity was only considered at encounter obtaining two trajectories in the Sun-EMB PCR3BP patched together by the Moon flyby. This approximation is accurate enough for an initial analysis but, when moving to the next phases of the design, more precise models are required. The objective of this section is to accurately reproduce the obtained trajectories by moving to the Sun-EMB and the Earth-Moon PCR3BP coupled analysis described in Section 2.2.

Initially, the PO departure condition was propagated directly, alternating between the Sun-EMB and the Earth-Moon equations of motions each time the spacecraft passed between the SOI$_{SE}$ and the SOI$_{EM}$. It was observed that, without corrections, the spacecraft would miss the encounter with the Moon, due to bad timing, and thus depart via a direct escape trajectory. In order to ensure the encounter, a bisection method was applied to find the zero of Eq. 6.2, where $\mathbf{x}_{ext}$ is the state of the spacecraft when it leaves the SOI$_{EM}$ with the 2BP, $\mathbf{x}$ is the same state but with the full PCR3BP and T is the time required from the departure to the encounter with the Moon.

$$\|\mathbf{x}_{ext} - \mathbf{x}(T + t_{corr})\| \tag{6.2}$$

At each iteration of the bisection method the differential corrector was used to compute the required departure conditions to obtain a manifold with $tof = T + t_{corr}$, the obtained state is then propagated in the full PCR3BP to obtain $\mathbf{x}$. This way it is possible to compute the required *time correction*, which for the example trajectories in Figure 6.4 is 1.44 and 1.99 days.
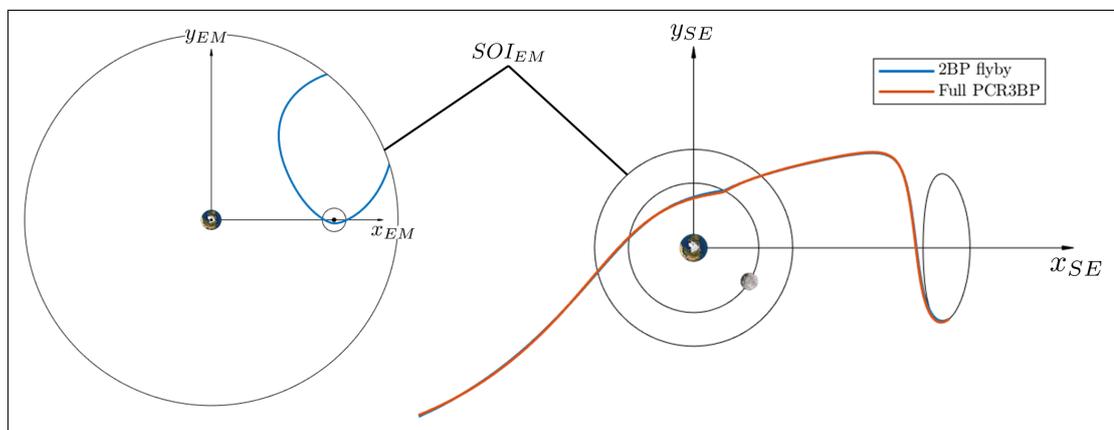

(a) $R_c < 1$ AU
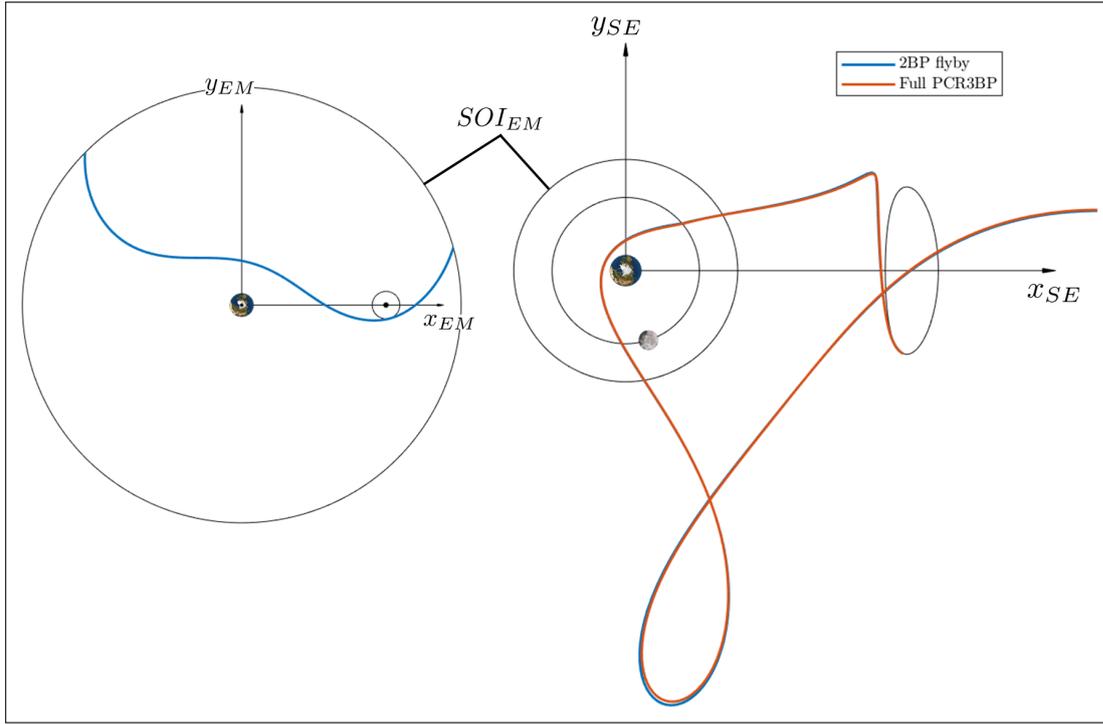
(b) $R_c > 1$ AU

Figure 6.4: Trajectories in the full PCR3BP. The trajectory sections in the SOI$_{EM}$ are represented also in the Earth-Moon synodic reference frame on the left.

In this particular cases both time corrections resulted to be positive and quite low, i. e., departure manifold with longer tof, however, also negative values were observed as the encounter is heavily influenced by the flight path angle, β, when entering the SOI$_{EM}$ and the time spent inside the SOI$_{EM}$ before the flyby. In particular it was observed that trajectories with steeper entry angles and with flybys at the IC presented less timing errors as opposed to trajectories with shallow entry angles and OC flybys. Since during the design the Moons gravity is completely neglected before and after the encounter, this type of behaviour was expected as the difference between the to models is greater the longer the spacecraft remains inside the SOI$_{EM}$.

However, as can be seen in Figure 6.4, both trajectories are well approximated by the higher-order model, meaning that the analysis performed under the 2BP flyby assumption is valid also when passing to more complex models.

6.4 EXAMPLE OF FULL MISSION TRAJECTORIES

The final objective of this work is to develop a methodology for the optimization of the departure trajectory in order to reduce the required Δv budget for the mission. To prove the validity of this concept and of the obtained results, three example transfers strategies are designed:

1. the trajectory is completely designed in the 2BP and the total Δv comprises the Earth escape cost and the DSM;

2. the Earth escape trajectory is computed in the PCR3BP without a lunar flyby and the interplanetary segment is still computed in the 2BP;

3. the Earth escape and the interplanetary segments are computed as for strategy 2, but here the lunar flyby is considered;

each strategy is optimized to intercept comets C2017T1 ($R_c < 1$ AU) and C2020N1 ($R_c > 1$ AU) which was recently discovered and works as an initial dry-run for the mission although the interception point is slightly outside the achievable region (due to thermal constraints). Note that the boundary between the PCR3BP and the 2BP is considered to be at 0.1 AU from the Earth.

The optimization of the interplanetary leg is performed by Professor Sánchez as it is out of the scope of this thesis. However, the main points of the process are briefly summarized hereafter:

- the transfer is computed in the heliocentric 2BP under the 'patched-conics' assumption;

- the full trajectory is divided into two Lambert arcs: one from the Earth (or the PCR3BP-2BP boundary) to the DSM and the second from the manoeuvre to the encounter;

- the design variable is the *tof* from Earth departure to the DSM;

- the value to minimize is the magnitude of the DSM plus the escape manoeuvre when only the 2BP is considered.

To correctly design the cislunar trajectory, at 0.1 AU a target state is identified from the full 2BP trajectory, the flyby optimization process is then adapted to the current problem in order to match as closely as possible this target by exploiting the lunar flyby. As the description of the cislunar trajectory remains the same, the only required adaptation concerns the fitness function which here is defined as

$$J = \left\| \begin{bmatrix} x^* - x \\ y^* - y \end{bmatrix} \right\| + 10^3 \left\| \begin{bmatrix} \dot{x}^* - \dot{x} \\ \dot{y}^* - \dot{y} \end{bmatrix} \right\|$$

where the superscript * indicates the components of the target state The coefficient before the velocity components is added as a weighting factor due to the difference in order of magnitude between the position and the velocity components. On the other hand, when considering the direct escape trajectory, the maximum v_∞ escape is considered. For completeness, as it was proven that lower flybys could improve the obtained escape trajectory, also escape trajectories with 100 and 500 km flyby altitudes were analysed to understand how the additional 200 m/s influence the total Δv budget in a 'real' case scenario. The obtained results are summarized in Table 6.2 together with a representation of the full transfer (from the Earth to the comet) in Figure 6.5.

| Model	Full 2BP	PCR3BP + 2BP	
Target	Δv^*, km/s		Δv^{**}, km/s
C2017T1	1.237	Direct	1.836
		Flyby	0.481
C2020N1	2.189	Direct	2.715
		Flyby, $h_{LB} = 5\,000$ km	2.025
		Flyby, $h_{LB} = 500$ km	1.444
		Flyby, $h_{LB} = 100$ km	1.234

* $\Delta v = \Delta v_{DSM} + \Delta v_{esc}$

** $\Delta v = \Delta v_{DSM}$

Table 6.2: Expected navigation budgets computed via Monte Carlo simulation.

The total Δv budget for the mission is estimated to be $1\,500$ m/s in the case of a hybrid propulsion system, i. e., chemical+electrical, or 750 m/s in the case of a pure chemical propulsion system [38]. Through the full 2BP analysis and considering the estimated budgets, it appears that C2017T1 is reachable only with in the case of a hybrid system while C2020N1 is never reachable.

Introducing the analysis under the PCR3BP leads to interesting results. In fact, while direct escapes do not provide any advantage, the introduction of the lunar flyby is essential for the success of the mission, in particular, in the case of C2017T1 a reduction of more than 750 m/s is observed. As the mentioned budget is allocated not only for the programmed manoeuvres, but also for the station-keeping in the PO and for the navigation, this cost reduction greatly improves the success rates of the missions as more propellant can be allocated for the initial waiting phase or for an extension of the mission after the comet swing-by.

In the case of C2020N1 the analysis is more problematic as the cost for the full 2BP is almost double of the available budget for the hybrid system. However, also here an improvement is observed, in particular when considering flyby altitudes of 100 and 500 km, for these trajectories the mission becomes achievable as the trajectory cost drops to 1.234 km/s.
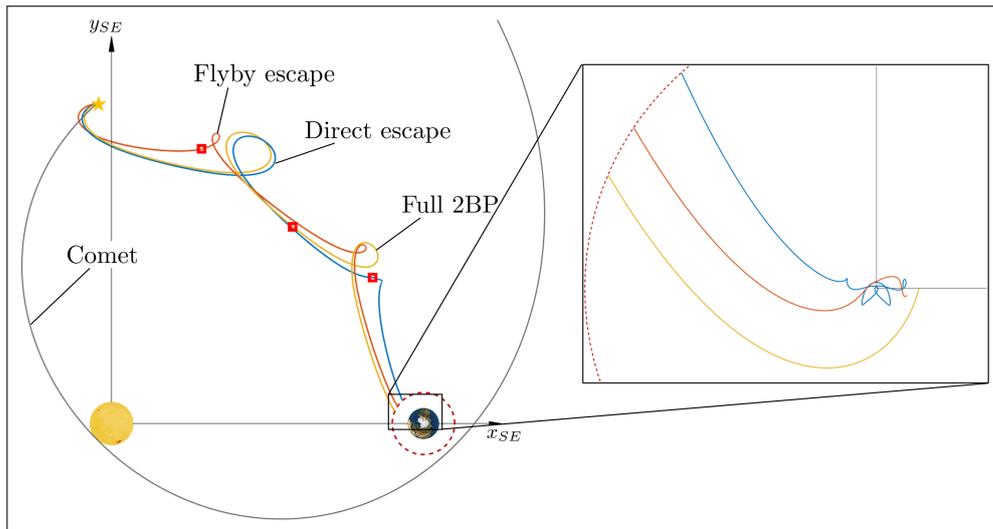
(a)
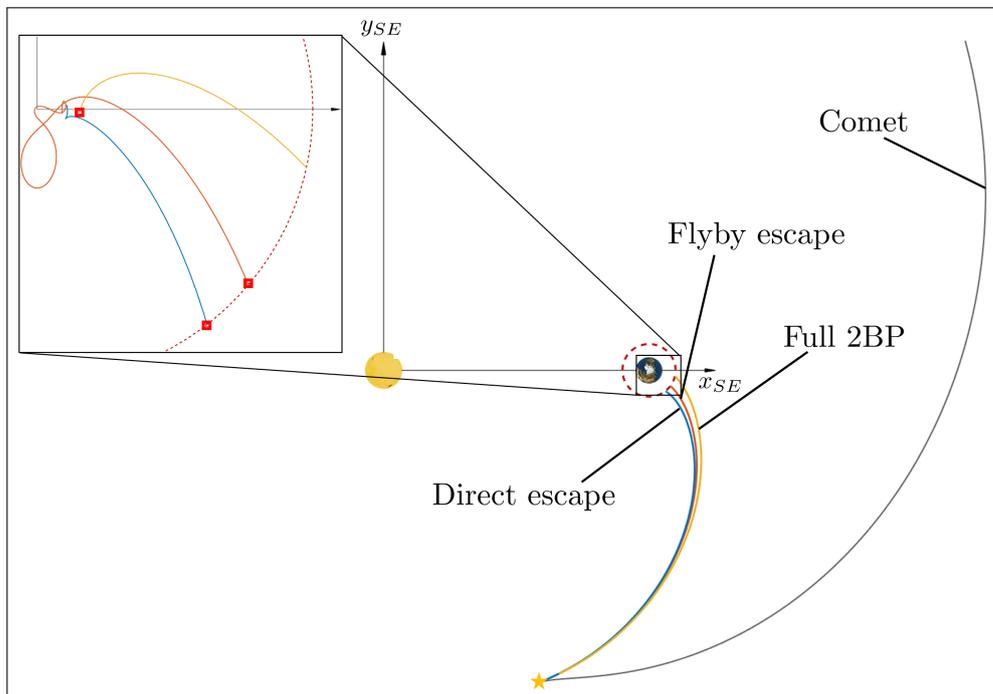
(b)

Figure 6.5: Optimized transfer trajectories from Earth (or L₂) to comets C2017T1 (a) and C2020N1 (b). The programmed DSM are represented with a □

7

CONCLUSIONS AND FURTHER DEVELOPMENT

THE aim of this thesis was to investigate the escape trajectory of Comet Interceptor when departing towards a comet. To maximize escape velocity with respect to the Earth, while minimizing the departure cost, it was fundamental to not only exploit the natural dynamics of the PCR3BP by following the unstable manifolds, but also to exploit the capabilities of a single flyby to achieve the optimal departure conditions.

It was already demonstrated that single and multiple lunar flybys can be programmed to obtain increased escape energy [43, 44]. However, these results were obtained under 'ideal' conditions: in the case of ISEE-3 it was possible to program a series of flybys to obtain the optimal final flyby, while, in the analysis by Chen et al., the optimal results were obtained by assuming the correct Moon position for the first flyby. It was thus necessary to evaluate the expected value of v_∞ under random initial values for the Moon's and the spacecraft's initial positions.

The work presented in this thesis demonstrates that, with a sufficient long waiting phase on the periodic orbit, values close to 1 km/s can be expected for the escape velocity. Furthermore, looking at the tof, it was proven that, when going towards $R_c < 1$ AU, the obtained strategy is also faster. This is not the case when going towards $R_c > 1$ AU, but the durations are still acceptable given the achieved increase of v_∞. These results were obtained through an optimization process which exploits

the genetic algorithm, as it is an iterative method it is not assured that the absolute minimum in found, this becomes clear when looking at the trajectories going towards $R_c > 1$ AU as the results obtained in this case are wider spread around the expected values. This behaviour is traced back to the onset of chaotic motion at the obtained energy levels, leading to the appearance of multiple local minima which 'trap' the final solutions, these local minima can be clearly as separated clusters in the Poincaré map drawn in Section 5.3.

Furthermore, it was demonstrated for trajectories towards $R_c > 1$ AU closer flybys could benefit the design resulting in higher escape velocities as high as 1.24 km/s and regularizing the optimization due to a sufficient increase of the energy which 'cancels' the chaotic behaviour. However, this benefit was not observed until the flyby limit is set under 1 250 km, and is never observed for trajectories towards $R_c < 1$ AU. This led to the conclusion that the optimal flyby does not only maximize the post-flyby energy but targets also the optimal escape conditions α_2 and β_2 leading to a final compromise of the two objectives.

7.1 FURTHER DEVELOPMENTS

The performed analysis is based on the assumption of planar orbits, i.e., the spacecraft and the Moon are located in the plane defined by the Sun-Earth system. However, CI will be placed in a quasi-Halo orbit around L$_2$ which, by definition, lives in the 3D space introducing additional complexities in the targeting of the lunar encounter. In particular, as pointed out by Chen, Kawakatsu, and Hanada [44], only a fraction of the propagated manifolds intersect the lunar orbit and can thus be utilized for the mission, see Figure 7.1. Furthermore, also the lunar flyby causes a rotation of the velocity vector in three dimensional space, changing the overall behaviour of the

trajectory after lunar encounter. It is thus necessary to extend the analysis to the CR3BP, in particular for the analysis of the invariant manifolds and the 3D flyby.
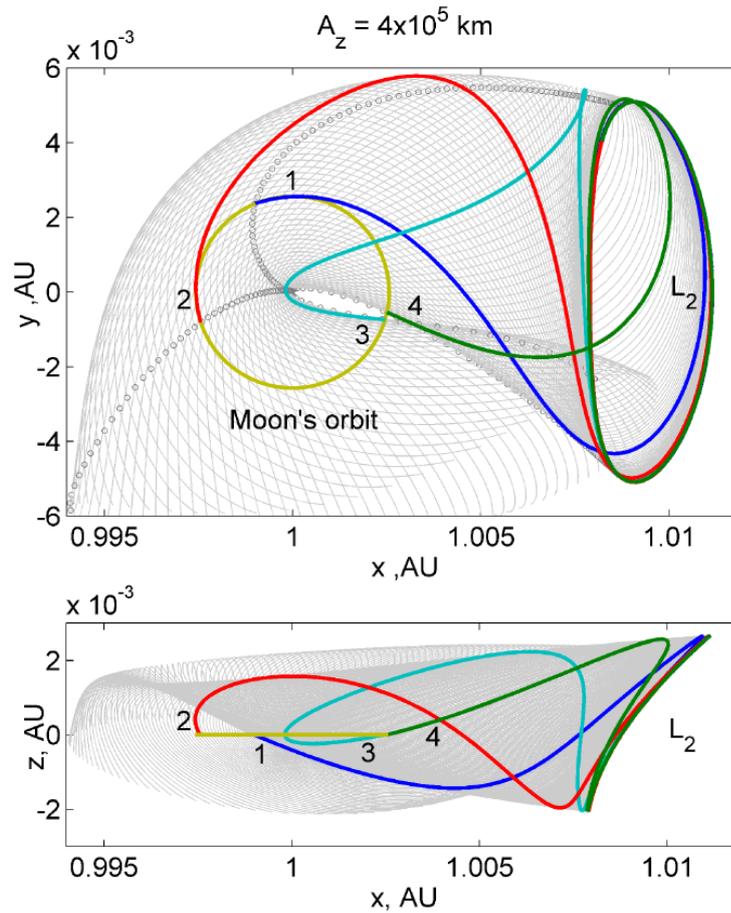

Figure 7.1: Three dimensional invariant manifolds; the manifolds which intersect the lunar orbit are highlighted [44].

Moreover, the current analysis identifies only single flyby strategies and does not consider any manoeuvre in the cislunar trajectory. However, as discussed by various authors, multiple flybys and the introduction of a manoeuvre could highly improve the escape conditions of the spacecraft [29, 45]. This can also be concluded by looking at the results of Section 5.2; in fact, it was observed that the possible encounter locations (after a single revolution around the Earth) are limited to a certain region of the obtained Poicaré sections from which is not always possible to reach the optimal post-flyby condition. By introducing the additional flyby and/or a manoeuvre it could

be possible to accurately target the second encounter in order to obtain the optimal escape condition, $(C_{2,opt}, \alpha_{2,opt}, \beta_{2,opt})$.

Finally, the obtained transfers to comets C2017T1 and C2020N1 were obtained by separating the trajectory into two independent optimization problems, one for the lunar flyby and one for the interplanetary leg. While this approach is valid for an initial study, the design would clearly benefit by optimizing the entire transfer at once. In fact, this could result in trajectories which do not present the highest escape velocity, but nonetheless naturally drift towards the final target requiring only a minimal DSM.

BIBLIOGRAPHY

[1] Paul R. Weissman. "The Oort cloud." In: *Nature* 344.6269 (1990), pp. 825–830. ISSN: 00280836. DOI: 10.1038/344825a0.

[2] Jian-Yang Li et al. "Early pre-perihelion characterization of Comet C/2012 S1 (ISON)." In: *DPS* (2013).

[3] R. Stevenson et al. "Neowise Observations of Comet C/2013 A1 (Siding Spring) as it approaches Mars." In: *Astrophysical Journal Letters* 798.2 (2015), p. 31. ISSN: 20418213. DOI: 10.1088/2041-8205/798/2/L31.

[4] Sean N. Raymond et al. "Implications of the interstellar object 1I/'Oumuamua for planetary dynamics and planetesimal formation." In: *Monthly Notices of the Royal Astronomical Society* 476.3 (2018), pp. 3031–3038. ISSN: 13652966. DOI: 10.1093/mnras/sty468. arXiv: 1711.09599.

[5] ESA. *ESA's new mission to intercept a comet.* 2019. URL: https://sci.esa.int/web/cosmic-vision/-/61416-esa-s-new-mission-to-intercept-a-comet.

[6] R. Reinhard. "The Giotto mission to Halley's Comet." In: *Exploration of Halley's Comet.* Springer Berlin Heidelberg, 1988, pp. 949–958. DOI: 10.1007/978-3-642-82971-0_165.

[7] Karl Heinz Glassmeier et al. "The Rosetta mission: Flying towards the origin of the solar system." In: *Space Science Reviews* 128.1-4 (2007), pp. 1–21. ISSN: 00386308. DOI: 10.1007/s11214-006-9140-8.

[8] Jose M. Sánchez Pérez et al. *Comet Interceptor - Mission Analysis Guidelines.* Tech. rep. European Space Operations Centre, 2020.

[9] Joan P. Sánchez. "ESA F-Class Comet Interceptor: A first close-up study of a dynamically "new" object." 2019.

[10] Paul J. Francis. "The Demographics of Long-Period Comets." In: *The Astrophysical Journal* 635.2 (2005), pp. 1348–1361. ISSN: 0004-637X. DOI: 10.1086/497684.

[11] David W. Hughes. "The magnitude distribution, perihelion distribution and flux of long-period comets." In: *Monthly Notices of the Royal Astronomical Society* 326.2 (2001), pp. 515–523. ISSN: 00358711. DOI: 10.1046/j.1365-8711.2001.04544.x.

[12] Asif A. Siddiqi. *Beyond Earth: a chronicle of deep space exploration, 1958-2016.* 2018. ISBN: 978-1-62683-043-1.

[13] John Uri. *45 Years Ago: Mariner 10 First to Explore Mercury.* 2019. URL: https://www.nasa.gov/feature/45-years-ago-mariner-10-first-to-explore-mercury (visited on 04/22/2020).

[14]   Gary A. Flandro. "Fast reconnaissance missions to the outer solar system utilizing energy derived from the gravitational field of Jupiter." In: *Acta Astronautica* 12.4 (1966), pp. 329–337.

[15]   Paul F. Thompson et al. "Parker solar probe navigation: One year from launch." In: *Advances in the Astronautical Sciences*. Vol. 162. 2018, pp. 575–589. ISBN: 9780877036456.

[16]   Howard D. Curtis. *Orbital Mechanics for Engineering Students*. Ed. by Elsevier. Third Edit. 2013. ISBN: 978-0-080-97747-8. DOI: 10.1016/C2011-0-69685-1.

[17]   Kazuyuki Yagasaki. "Sun-perturbed earth-to-moon transfers with low energy and moderate flight time." In: *Celestial Mechanics and Dynamical Astronomy* 90.3-4 (2004), pp. 197–212. ISSN: 09232958. DOI: 10.1007/s10569-004-0406-8.

[18]   Junichiro Kawaguchi et al. "On making use of Lunar and Solar Gravity Assists in LUNAR-A, PLANET-B Missions." In: *Acta Astronautica* 35.9-11 (1995), pp. 633–642. ISSN: 00945765. DOI: 10.1016/0094-5765(95)00013-P.

[19]   Wang Sang Koon et al. *Dynamical Systems, the Three-Body Problem and Space Mission Design*. Marsden Books, 2006. ISBN: 978-0-615-24095-4.

[20]   E Belbruno. "The Dynamical Mechanism of Ballistic Lunar Capture Transfers in the Four Body Problem from the Perspective of Invariant Manifolds and Hill's Regions." 1994.

[21]   Yi Qi and Shijie Xu. "Study of lunar gravity assist orbits in the restricted four-body problem." In: *Celestial Mechanics and Dynamical Astronomy* 125.3 (2016), pp. 333–361. ISSN: 15729478. DOI: 10.1007/s10569-016-9686-z.

[22]   Christian Marchal. *The Three-Body Problem*. 1st ed. Elsevier, 1990. ISBN: 978-0-444-87440-5.

[23]   Mauri Valtonen and Hannu Karttunen. *The Three-Body Problem*. Cambridge University Press, 2005. ISBN: 978-0-521-85224-1.

[24]   Jerrold E. Marsden and Tudor S. Ratiu. *Introduction to Mechanics and Symmetry (Texts in Applied Mathematics vol 17)*. 1999.

[25]   Victor G. Szebehely. *Theory of Orbit: The Restricted Problem of Three Bodies*. Academic Press, 1967. ISBN: 978-0-12-395732-0. DOI: 10.1016/b978-0-12-395732-0.x5001-6.

[26]   Jürgen Moser. "On the generalization of a theorem of A. Liapounoff." In: *Communications on Pure and Applied Mathematics* 11.2 (1958), pp. 257–271. ISSN: 10970312. DOI: 10.1002/cpa.3160110208.

[27]   Yusuke Hagihara. *Celestial mechanics: Topology of the Three-Body Problem*. Volume 5. 1976.

[28]   Roberto Castelli. "Regions of prevalence in the coupled restricted three-body problems approximation." In: *Communications in Nonlinear Science and Numerical Simulation* 17.2 (2012), pp. 804–816. ISSN: 10075704. DOI: 10.1016/j.cnsns.2011.06.034.

[29]   Stefano Campagnola and Ryan P. Russell. "Endgame Problem Part 1: V-Leveraging Technique and the Leveraging Graph." In: *Journal of Guidance, Control, and Dynamics* 33.2 (2010), pp. 463–475. ISSN: 07315090. DOI: 10 . 2514/1.44258.

[30]   James Richard Wertz et al. *Space Mission Engineering: The New SMAD.* 2011, p. 1033. ISBN: 1881883167.

[31]   E. Barrabés et al. "Dynamical aspects of multi-round horseshoe-shaped homo-clinic orbits in the RTBP." In: *Celestial Mechanics and Dynamical Astronomy* 105.1 (2009), pp. 197–210. ISSN: 09232958. DOI: 10.1007/s10569-009-9190-9.

[32]   E Barrabés et al. "Numerical continuation of families of homoclinic connections of periodic orbits in the RTBP." In: *Nonlinearity* 22.12 (2009), pp. 2901–2918. ISSN: 09517715. DOI: 10.1088/0951-7715/22/12/006.

[33]   G. Gómez et al. "The invariant manifold structure of the spatial Hill's problem." In: *Dynamical Systems* 20.1 (2005), pp. 115–147. ISSN: 14689367. DOI: 10.1080/14689360412331313039.

[34]   Wang Sang Koon et al. "Heteroclinic connections between periodic orbits and resonance transitions in celestial mechanics." In: *Chaos* 10.2 (2000), pp. 427–461. ISSN: 10541500. DOI: 10.1063/1.166509.

[35]   Jeffrey S. Parker et al. "Chaining periodic three-body orbits in the EarthMoon system." In: *Acta Astronautica* 67.5-6 (2010), pp. 623–638. ISSN: 00945765. DOI: 10.1016/j.actaastro.2010.04.003.

[36]   Amanda F. Haapala and Kathleen C. Howell. "Representations of higher-dimensional Poincaré maps with applications to spacecraft trajectory design." In: *Acta Astronautica* 96.1 (2014), pp. 23–41. ISSN: 00945765. DOI: 10.1016/j.actaastro.2013.11.019.

[37]   Carlos Sánchez Lara. "Preliminary Design of Near Rectilinear Orbits around the Moon as Operational Orbit for the Future Deep Space Gateway tle." MA thesis. Cranfield University, 2018.

[38]   Jose M. Sánchez Pérez et al. *Comet Interceptor: Consolidated Report on Mission Analysis.* Tech. rep. European Space Operations Centre, 2020.

[39]   David W. Dunham and Sylvia A. Davis. "Optimization of a Multiple Lunar-Swingby Trajectory Sequence." In: *AIAA Paper.* Reston, Viriginia: American Institute of Aeronautics and Astronautics, 1984. DOI: 10.2514/6.1984-1978.

[40]   Cesar A. Ocampo. "Transfers to Earth centered orbits via lunar gravity assist." In: *Acta Astronautica.* Vol. 52. 2-6. Pergamon, 2003, pp. 173–179. DOI: 10 . 1016/S0094-5765(02)00154-6.

[41]   Paul A. Penzo. *A Survey and Recent Development of Lunar Gravity Assist.* 1998. URL: https://ntrs.nasa.gov/search.jsp?R=20010000274.

[42]   Roby S. Wilson and Kathleen C. Howell. "Trajectory Design in the Sun-Earth-Moon System Using Lunar Gravity Assists." In: *Journal of Spacecraft and Rockets* 35.2 (1998), pp. 191–198. ISSN: 00224650. DOI: 10.2514/2.3309.

[43]   Robert Farquhar. "The flight of ISEE-3/ICE: origins, mission history, and a legacy." In: *AIAA/AAS Astrodynamics Specialist Conference and Exhibit*. Reston, Virigina: American Institute of Aeronautics and Astronautics, 1998, pp. 1–59. DOI: 10.2514/6.1998-4464.

[44]   Hongru Chen et al. "Earth Escape from a Sun-Earth Halo Orbit using Unstable Manifold and Lunar Swingbys." In: *Transactions of the Japan Society for Aeronautical and Space Sciences* 59.5 (2016), pp. 269–277. ISSN: 05493811. DOI: 10.2322/tjsass.59.269.

[45]   Daniel García Yárnoz et al. "Extended Tisserand-Poincare Graph and Multiple Lunar Swingby Design with Sun Perturbation." In: *Sixth International Conference on Astrodynamics Tools and Techniques* (2016).

[46]   Bruno V. Sarli et al. "DESTINY+ Trajectory Design to (3200) Phaethon." In: *Journal of the Astronautical Sciences* 65.1 (2018), pp. 82–110. ISSN: 21950571. DOI: 10.1007/s40295-017-0117-5.

[47]   Jose J. Guzman et al. "STEREO Mission Design Implementation." In: *20th International Symposium on Space Flight Dynamics*. 2007.

[48]   Timothy P. Mcelrath et al. "Using gravity assists in the Earth-Moon system as a gateway to the Solar System." In: *Global Space Exploration Conference*. 2012.

[49]   David W. Dunham et al. "STEREO trajectory and maneuver design." In: *Johns Hopkins APL Technical Digest (Applied Physics Laboratory)* 28.2 (2009), pp. 104–125. ISSN: 02705214.

[50]   Stefano Campagnola et al. "Design of Lunar Gravity Assist for the Bepi-Colombo Mission to Mercury." In: *Advances in the Astronautical Sciences*. Vol. 119. SUPPL. 2005, pp. 427–441.

[51]   D. V. Byrnes and H. L. Hooper. "Multi-Conic: A Fast and Accurate Method of Computing Space Flight Trajectories." In: *AIAA Paper*. American Institute of Aeronautics and Astronautics, 1970. DOI: 10.2514/6.1970-1062.

[52]   S. W. Wilson. "A Pseudostate Theory for the Approximation of Three-Body Trajectories." In: *AIAA Paper*. American Institute of Aeronautics and Astronautics, 1970. DOI: 10.2514/6.1970-1061.

[53]   Antonio Fernando Bertachini de Almeida Prado. "A comparison of the "patched-conics approach" and the restricted problem for swing-bys." In: *Advances in Space Research* 40.1 (2007), pp. 113–117. ISSN: 02731177. DOI: 10.1016/j.asr.2007.01.012.

[54]   Ryan Perry. "Mission Analysis of Intercepting a Dynamical New Comet from a Halo Orbit Launch Around the Sun-Earth L2 Libration Point." MA thesis. Cranfield University, 2019.

[55]   Gerard Gómez et al. *Study Refinement of Semi-Analytical Halo Orbit Theory*. Tech. rep. 1991, p. 89.

[56]   Michihiro Matsumoto and Junichiro Kawaguchi. "Escape Trajectory from the Sun-Earth L2 Point." In: *Proceedings of 15th Workshop on JAXA Astrodynamics and Flight Mechanics*. 2006.

[57]   Masaki Nakamiya and Hiroshi Yamakawa. "Earth Escape Trajectories Starting from L2 Point." In: *Collection of Technical Papers - AIAA/AAS Astrodynamics Specialist Conference*. Vol. 3. American Institute of Aeronautics and Astronautics, 2006, pp. 1953–1972. ISBN: 1563478226. DOI: 10.2514/6.2006-6751.

[58]   John C. Niehoff. "Gravity-assisted trajectories to solar-system targets." In: *Journal of Spacecraft and Rockets* 3.9 (1966), pp. 1351–1356. ISSN: 00224650. DOI: 10.2514/3.28659.

[59]   R. H. Smith and V. Szebehely. "The onset of chaotic motion in the restricted problem of three bodies." In: *Celestial Mechanics & Dynamical Astronomy* 56.3 (1993), pp. 409–425. ISSN: 09232958. DOI: 10.1007/BF00691811. URL: https://link.springer.com/article/10.1007/BF00691811.

[60]   Kenshiro Oguri et al. "EQUULEUS Trajectory Design." In: *Journal of the Astronautical Sciences* (2020), pp. 1–27. ISSN: 21950571. DOI: 10.1007/s40295-019-00206-y.

[61]   Yi Qi and Shijie Xu. "Mechanical analysis of lunar gravity assist in the Earth–Moon system." In: *Astrophysics and Space Science* 360.2 (2015), pp. 1–15. ISSN: 1572946X. DOI: 10.1007/s10509-015-2571-5.

[62]   Lawrence Davis. *Handbook of genetic algorithms*. New York: Van Nostrand Reinhold, 1991.

[63]   David E. Goldberg. "Genetic Algorithms in Search." In: *Optimization and Machine Learning* (1989).

[64]   John H. Holland. *Adaptation in Natural and Artificial Systems*. Ann Arbor: The University of Michigan Press, 1975.

[65]   Zbigniew Michalewicz. *Genetic Algorithms + Data Structures = Evolution Programs*. Springer New York, 1994.

[66]   Sheldon M. Ross. *Introduction to Probability and Statistics for Engineers and Scientists*. 5th. Academic Press, 2014. ISBN: 978-0-12-394811-3.

[67]   Steven C. Gordon. "Orbit Determination Error Analysis and Station-Keeping For Libration Point Trajectories." PhD Dissertation. Purdue University, 1991.

[68]   Kathleen C. Howell and Steven C. Gordon. "Orbit Determination Error Analysis and a Station-Keeping Strategy for Sun-Earth L1 Libration Point Orbits." In: *Journal of the Astronautical Sciences* 42.2 (1994), pp. 207–228. ISSN: 00219142.

[69]   Kathleen C. Howell and Henry J. Pernicka. "Station-keeping method for libration point trajectories." In: *Journal of Guidance, Control, and Dynamics* 16.1 (1993), pp. 151–159. ISSN: 07315090. DOI: 10.2514/3.11440.

[70]   Henry J. Pernicka. "The numerical determination of nominal libration point trajectories and development of a station-keeping strategy." PhD Dissertation. Purdue University, 1990.

[71]   C Simó et al. "On the Optimal Station Keeping Control of Halo Orbits." In: *Acta Astronautica* 15.6-7 (1987), pp. 391–397. ISSN: 00945765. DOI: 10.1016/0094-5765(87)90175-5.

[72]   Kathleen C. Howell and Timothy M. Keeter. "Stationkeeping Strategies for Libration Point Orbits: Target Point and Floquent Point Approaches." In: *Advances in Astronautical Sciences* 89.2 (1995), pp. 1377–1396.

[73]   Timothy M. Keeter. "Station-Keeping Strategies for Libration Point Orbits: Target Point and Floquet Mode Approaches." MA thesis. Purdue University, 1994.

[74]   Vivek Muralidharan. "Orbit Maintenance Strategies for Sun-Earth/Moon Libration Point Missions: Parameter Selection for Target Point and Cauchy-Green Tensor Approaches." MA thesis. Purdue University, 2017.

[75]   Gerard Gómez et al. *Dynamics and Mission Design Near Libration Points, Vol. I Fundamentals: The Case of Collinear Libration Points.* World Scie. World Scientific Publishing, 2001. ISBN: 981-02-4285-9.